



HAL
open science

Wenchuan-Maoxian Fault (Longmen Shan, China) Cenozoic kinematics, geodynamics implications

Chenglong Ge

► **To cite this version:**

Chenglong Ge. Wenchuan-Maoxian Fault (Longmen Shan, China) Cenozoic kinematics, geodynamics implications. Earth Sciences. Université Claude Bernard - Lyon I; Université de Pékin, 2023. English. NNT : 2023LYO10185 . tel-04887652

HAL Id: tel-04887652

<https://theses.hal.science/tel-04887652v1>

Submitted on 15 Jan 2025

HAL is a multi-disciplinary open access archive for the deposit and dissemination of scientific research documents, whether they are published or not. The documents may come from teaching and research institutions in France or abroad, or from public or private research centers.

L'archive ouverte pluridisciplinaire **HAL**, est destinée au dépôt et à la diffusion de documents scientifiques de niveau recherche, publiés ou non, émanant des établissements d'enseignement et de recherche français ou étrangers, des laboratoires publics ou privés.

Université Claude Bernard Lyon 1



北京大學
PEKING UNIVERSITY

THESE de DOCTORAT DE L'UNIVERSITE CLAUDE BERNARD LYON 1

**Ecole Doctorale : PHAST 52
Physique et Astrophysique**

Discipline : Earth and Planetary Sciences

Soutenue publiquement le 20/10/2023, par :
Chenglong GE

Wenchuan-Maoxian Fault (Longmen Shan, China) Cenozoic kinematics, geodynamics implications

Devant le jury composé de :

TIAN Yuntao Professor of Sun Yat-sen University, Guangdong	Président, Rapporteur
FAURE Michel Professor of Université d'Orléans, Orléans	Rapporteur
GARDIEN Véronique Professor of Université Lyon1, Lyon	Examinatrice
LELOUP Hervé Philippe Director researcher of CNRS-Université Lyon1, Lyon	Directeur de thèse
LI Haibing Director researcher of CAGS, Beijing	Co-Directeur de thèse
YAN Danping Professor of China University of Geosciences, Beijing	Rapporteur

Abstract

The Longmen Shan tectonic belt is located in the eastern margin of the Tibetan Plateau, marks the boundary between the plateau and the Sichuan Basin, and represents the steepest continental topography in the world. It has a vertical elevation drop of nearly 5,000 m and presents significant differences in crustal structure. The Longmen Shan tectonic belt consists of three main faults, from west to east: the Wenchuan-Maoxian fault (hinterland fault), the Yingxiu-Beichuan fault (central fault), and the Guanxian-Anxian fault (foreland fault). Because the last two faults ruptured simultaneously during the 2008 Wenchuan Ms8.0 earthquake, and not the Wenchuan-Maoxian fault, their deformation behavior and role in the process of large earthquakes, including how they regulate the uplift of the Longmen Shan, are important aspects of understanding the occurrence of large earthquakes and the process of mountain range formation. Current research shows that of the three major faults, only the Wenchuan-Maoxian fault exposes deep ductile deformation and shallow brittle deformation rocks (mylonite, cataclasite, fault gouge, and fault breccia). In addition, Mesozoic deformation suggests that this fault records long-term processes and uplift, hence providing a clearer understanding of the Longmen Shan formation process, while the different sense of motion of the Wenchuan-Maoxian fault zone directly affect the establishment of different models of the Longmen Shan uplift: the upper crustal horizontal shortening model requires that the Wenchuan-Maoxian fault is reverse, whereas the lower crustal flow model requires that it is normal, in order to coordinate block extrusion. Therefore, the Cenozoic tectonic deformation of the Wenchuan-Maoxian fault is crucial to accurately understand the formation of the Longmen Shan and the environment in which strong earthquakes occur. This paper presents a systematic study of the geometry, kinematics, and chronology of deep ductile and shallow brittle deformation within the Wenchuan-Maoxian fault zone, and discusses the relationship between faulting and uplift of the Longmen Shan in the framework of regional thermal chronology data, as well as possible orogenic mechanisms in the eastern margin of the Tibetan Plateau.

Through detailed field investigation, we identified a ductile shear zone of ~3 km wide, steeply NW-dipping, in the Wenchuan-Maoxian fault, within which lies a brittle fracture zone consisting of fault gouge, fault breccia, and fracture zones with a width of ~50 m and steeply NW-dipping (60-70°).

Based on microstructural studies, two different phases of ductile deformation were identified within the ductile shear zone: normal with dextral deformation towards the NW, and NW-SE thrust deformation. Highly accurate petrologic and ^{40}Ar - ^{39}Ar chronology constrain the deformation to ~28 and ~15 Ma, respectively. Chlorite and quartz lattice thermometers indicate deformation temperatures of ~350°C and ~300°C, respectively.

High resolution remote sensing images show a clear, linear Wenchuan-Maoxian fault in the central part of the Longmen Shan. Macro- and microstructure of the fault gouge within the brittle fault zone shows that the brittle fault is clearly dextral with a thrust component. The dissected river and geological units indicate a right-lateral offset of ~25 km. In addition, the brittle deformation timing defined by authigenic illite dating of the fault gouge is ~7 Ma, thus yielding a dextral slip rate of ~3.6 mm/yr. for this fault.

Direct fault gouge dating obtained in this study is in good agreement with the indirect ages constrained by previous thermochronology data on fault activity, which identified three phases of tectonic deformation in the Wenchuan-Maoxian fault zone during the Cenozoic: normal with right-lateral movement during the Oligocene (~30-25 Ma), thrusting during the Oligocene to Miocene (25-15 Ma), and dextral with thrust movement during the Late Miocene (~7 Ma).

Our results show that the Wenchuan-Maoxian fault has not experienced purely downward Cenozoic normal deformation, and that horizontal shortening deformation has mainly existed since the Oligocene. Combined with regional geophysical data, we suggest that crustal channel flow may not have been an effective mechanism for generating and maintaining the steep topography of the Longmen Shan, and that the formation of the Longmen Shan results from horizontal shortening and thickening of the crust.

KEY WORDS: Longmen Shan; Wenchuan-Maoxian fault; Ductile faulting; Brittle faulting; Petro-geochronology; Mountain building

This manuscript is organized around two peer-reviewed articles (one published, one in preparation). All the published papers have been reported in their accepted (or submitted) versions and have been inserted as a whole.

Content

Abstract	2
1 Introduction	6
2 Cenozoic kinematics of the Wenchuan-Maoxian fault implies crustal stacking rather than channel flow extrusion at the Tibetan plateau eastern margin (Longmen Shan).	8
2.1 Introduction	8
2.2 Geological background.	10
2.2.1 The Longmen Shan belt.	10
2.2.2 The Wenchuan - Maoxian fault zone.	12
2.3. Field constraints on the structural evolution of the Wenchuan-Maoxian (WM) fault zone.	13
2.3.1 Ductile kinematics.....	13
2.3.2 Brittle kinematics.	14
2.3.3 Quantitative offset estimates.	16
2.4 Temporal constraints	17
2.4.1 K-Ar dating of fault gouge	17
2.4.2 White mica ⁴⁰ Ar/ ³⁹ Ar dating.....	18
2.5 Discussion	20
2.5.1 Timing of brittle and ductile deformation in the WM fault zone.....	20
2.5.2 Differential uplift across the WM fault zone	21
2.5.3 Cenozoic faulting and building of Longmen Shan.....	23
2.5.4 Cenozoic building of the Tibetan eastern margin: channel flow or crustal stacking?	24
2.6 Conclusions	24
3 The Wenchuan shear zone and the deformation history of the Longmen Shan.....	26
3.1 Introduction	26
3.2 Geological setting.....	28
3.3 Ductile deformation of Wenchuan-Maoxian fault	29
3.3.1 The Wenchuan shear zone.....	30
3.3.2 Southwest and North of Pengguan Massif	32
3.4 Sampling and analytical strategy.....	34
3.5 Results and interpretation.....	35
3.5.1 Quartz crystallographic preferred orientation	35
3.5.2 Petro-Geochronology in white mica	38
3.5.3 Chlorite thermometer	40
3.6 Discussion	42
3.6.1 Kinematics and deformation condition	42
3.6.2 Width of shear zone.....	43
3.6.3 Timing	44
3.7 Conclusions	48
4 Summary and conclusion	49
Reference.....	51
Appendix	70

1 Introduction

Known as the world's "third pole," the Tibetan Plateau is undoubtedly one of the most impressive geologic formations on the planet, providing geologists with important insights into the dynamics of the Earth's crust. The Longmen Shan, on the eastern edge of the Tibetan Plateau, are the area with the largest elevation difference around the circumference of the Plateau. Geomorphologically, the vertical elevation difference from the Sichuan Basin to the Tibetan Plateau can be up to 5000 m within a distance of less than 50 km horizontally, and there is also a difference of ~20 km in the thickness of the crust. Moreover, the Longmen Shan themselves are highly seismically active, with several large earthquakes of magnitude 7 or greater occurring along the fault belt, suggesting that deformation associated with plateau growth is still ongoing in the Longmen Shan region today. Therefore, the Longmen Shan region, located at the eastern edge of the Tibetan Plateau, is an excellent place to study in order to gain a deeper understanding of the uplift of the Tibetan Plateau and crustal thickening processes.

However, there are still a series of outstanding world-class geological problems in the Longmen Shan. For example, it lacks a corresponding Cenozoic foreland sedimentary basin (SBGMR, 1991; Burchfiel et al., 1995, 2008), and GPS geodetic surveys indicate that the Longmen Shan area has a very low horizontal shortening rate (< 3 mm/yr.) (Zhang et al., 2004; Wang and Shen, 2020). So how do such low horizontal transport rates of material support or lead to such high differences in topography and crustal thickness? In order to explain these phenomena, two very different endmember models have been proposed based on the available geological and geophysical data. The first one is the crustal shortening model, which suggests that a series of crustal-scale faults underwent thrusting leading to crustal thickening and surface uplift in the Longmen Shan (Hubbard and Shaw, 2009; Hubbard et al., 2010). The other is the lower crustal channel flow model, which suggests that there was a flowable "soft" lower crust beneath the eastern margin of the Tibetan Plateau, which was blocked by the rigid Sichuan Basin and transported upward, resulting in the present steep topography and thickened crust of the Longmen Shan (Royden et al. 1997, 2008; Clark and Royden, 2000; Clark et al. 2005a; Burchfiel et al. 2008). However, these two very different end-member models have different requirements for fault activity in the region. The upper crustal shortening model requires that these faults have uniform activity of thrusting (Fig. 1.3b). In contrast, the lower crustal channel flow model requires that the fault in the hinterland must have normal deformation to regulate the upward extrusion of the block in conjunction with the reverse fault in the foreland (Fig. 1.3c). From this point of view, the Wenchuan-Maoxian fault located at the hinterland of Longmen Shan seems to be the key to solve this problem. The Wenchuan-Maoxian fault is also the only one in the Longmen Shan tectonic belt with ductile deformation, which develops different levels of deformation from deep to shallow, and is of great significance for us to understand the uplift process of the Longmen Shan systematically and completely from deep to shallow. The low-temperature thermochronology data show that the blocks on both sides of the Wenchuan-Maoxian fault have obvious differential uplift processes, implying that the fault zone may have had complex deformation processes in the Cenozoic. However, there is no corresponding Cenozoic fault activity event reported in the hinterland of Longmen Shan. There is still no clear and unified understanding of the tectonic deformation process of the Wenchuan-Maoxian fault since the Cenozoic.

In addition, the Wenchuan-Maoxian Fault is an important block boundary on the eastern margin of the Tibetan Plateau (Fig. 1.3a), separating the Songpan-Ganzi Massif (Tibetan Plateau) from the Sichuan Basin (Yangzi block), and is an important tectonic and sedimentary boundary. Its various phases of tectonic deformation also control the geological evolution of the whole region, and also play a fundamental role in the growth of the present Longmen

Shan and the distribution of seismic stress. In recent years, with the rapid development of deformation dating methods in fault zones, the problem of accurate dating of brittle faulting, which had troubled geologists before, can now be effectively solved. Thus, we can have a complete understanding of the deformation evolution of a fault zone from deep to shallow, at different levels and in different epochs. Therefore, in this work we combine structural geology with illite K/Ar dating on fault gouges and *in situ* and step-heating $^{40}\text{Ar}/^{39}\text{Ar}$ dating of mica in greenschist-facies rocks deformed along the fault system to constrain the kinematics of the Wenchuan-Maoxian fault zone, trying to clarify the corresponding deformation sequence of the fault zone. Thus, we further explore the relationship between the fault activities and the uplift of Longmen Shan, as well as the implications for the formation of the plateau and the thickening process of the crust.

2 Cenozoic kinematics of the Wenchuan-Maoxian fault implies crustal stacking rather than channel flow extrusion at the Tibetan plateau eastern margin (Longmen Shan).

2.1 Introduction

The Tibetan plateau with an average elevation >5000 m a.s.l., and a 65-80 km-thick crust, is the largest high plateau on earth. Geological and geophysical studies suggest it has a complex structure largely shaped by the India / Eurasia collision since ~55 Ma (e.g.: Tapponnier et al., 2001; Yin and Harrison, 2000). Various models corresponding to contrasted views of the continental lithosphere rheology have been proposed to explain the Cenozoic formation and evolution of the Tibetan plateau.

Lateral extrusion of partially molten crustal material outward from below the Tibetan plateau has been proposed for the building of the Himalaya and Eastern Tibet structure and topography. Such mechanism would be strongly coupled with high erosion focussed on the ranges slope and would explain extrusion of a piece of crust between parallel and coeval thrust at the base and normal fault at the top. Central to this model is the geophysical (seismic, magnetotelluric) observation of widespread Low Velocity Zones (LVZ) within the crust interpreted as diagnostic of present-day partial melting and thus extremely weak rheology (e.g., Nelson et al., 1996; Klemperer, 2006), that would decouple deformation in the upper crust from that in the lower crust / upper mantle.

In the Himalaya, channel flow has been suggested to explain lower Miocene extrusion of partially molten gneisses of the Greater Himalayan Sequence between the Main Central Thrust at the base of the range and the South Tibet Detachment at the top (e.g.; Beaumont et al., 2001; Jamieson et al., 2004; Searle and Szulc, 2005). This popular model may be questioned because the partial melting, the Main Central Thrust and the South Tibet Detachment are not exactly synchronous (e.g., Leloup et al., 2015). Some still favour an accretionary prism model where the structure and topography of the Himalaya result from crustal stacking in an accretionary prism (e.g., Bollinger et al., 2006; Kohn et al., 2008).

In any case, motion on the South Tibet Detachment, and thus potential channel flow toward the south, ended between 13 and 11 Ma ago (e.g., Leloup et al., 2010). Since ~15 Ma (middle Miocene) crustal flow would have veered toward the east inducing E-W extension in Central Tibet and outward migration of the eastern Tibet topography (e.g., Klemperer, 2006; Adams and Hodges, 2022). That second phase of channel flow would have created the world's steepest topographic continental slope in the Longmen Shan (LMS) towering nearly 5000 m above the Sichuan basin (Fig. 1c). Lower crustal material expelled from below Tibet would inflate when buttressing against the rigid South China craton (e.g., Royden et al., 1997; Clark and Royden, 2000), generating coeval reverse fault at the bottom and normal fault at the top (Fig. 2b) (e.g., Clark et al., 2005a, b; Royden et al., 2008; Burchfiel et al., 2008). This makes of the LMS an archetype example of an orogenic system built by crustal channel flow extrusion since the Miocene. But others rather advocate thickening through crustal stacking on reverse faults where deformation in the upper crust is strongly coupled with that in the lower crust / upper mantle (e.g., Hubbard and Shaw, 2009; Hubbard et al., 2010; Li et al., 2010; Tian et al., 2013; Wu et al., 2014; Lu et al., 2016) (Fig. 2a). One of the key points to distinguish between these models is the kinematics of the Wenchuan-Maoxian (WM) fault zone located in the internal part of the

belt: in the lower crustal flow extrusion model the fault should show a normal component of motion coeval with thrusting at the front of the range (Fig. 2b).

Kinematics of the WM fault zone is however still poorly documented especially for the Miocene, at a time when lower crustal flow is thought to be dominant (e.g., Clark et al., 2005a). In this work we combine structural geology with illite K/Ar dating on fault gouges and *in situ* and step-heating $^{40}\text{Ar}/^{39}\text{Ar}$ dating of mica in greenschist-facies rocks deformed along the fault system to constrain the kinematics of the WM fault zone since ~30 Ma, and thus to discuss the Longmen Shan building mechanism(s).

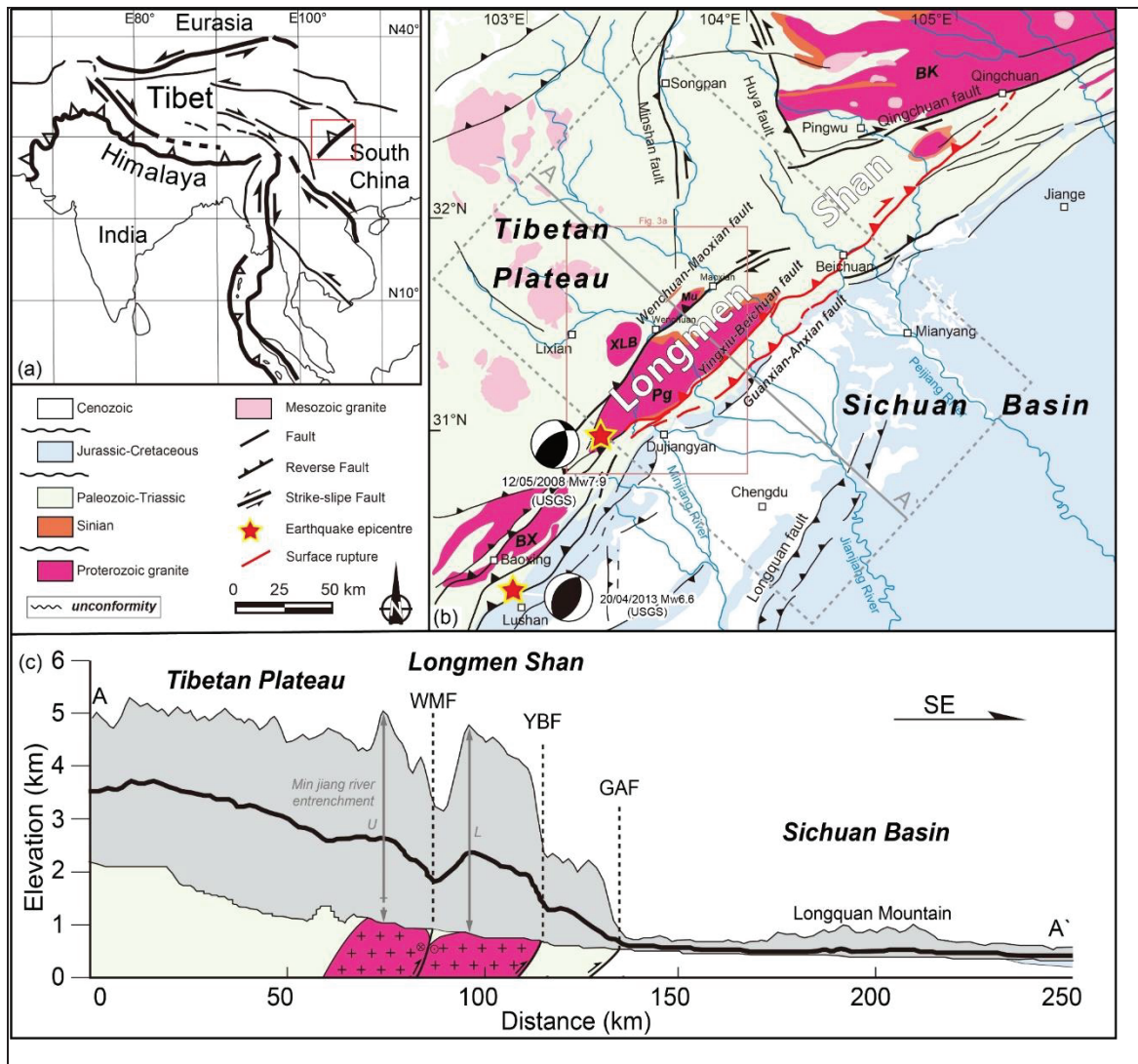


Fig. 1 The Longmen Shan belt (a) Location of the Longmen Shan in the frame of the India-Asia collision. (b) Geological map of Longmen Shan and adjacent area (modified from Li et al., 2014), with three major faults: Wenchuan-Maoxian (WMF), Yingxiu-Beichuan (YBF), and Guanxian-Anxian (GAF). Focal mechanisms of Wenchuan and Lushan Earthquakes are shown. Basement ranges: MT, Mutuo; XLB, Xuelongbao; PG, Pengguan; BX, Baoxing; BK, Bikou. (c) A-A' cross section. Grey frame is the topography (swath profile) with average (bold), upper and lower values. Simplified geological cross section at the bottom. Double arrows indicate the minimum entrenchment of the Min Jiang river: U, upper reach, L, Lower Reach.

2.2 Geological background.

2.2.1 The Longmen Shan belt.

The Longmen Shan separates the Songpan-Ganze block (Tibetan plateau) in the west from the Sichuan Basin in the east and is straddled from west to east by three major sub-parallel fault zones: Wenchuan-Maoxian (WM), Yingxiu-Beichuan, and Guanxian-Anxian (Fig. 1b) (e.g., SBGMR 1991). Surface geology and geophysical studies suggest that the faults are NW-dipping, listric and that they merge into a detachment at depth of ~20-30 km (Feng et al., 2016; Hubbard and Shaw, 2009). In the Central Longmen Shan, three basement complexes (Pengguan (PG), Mutuo (MT) and Xuelongbao (XLB)) are composed of Neoproterozoic meta-granites unconformably overlain by a Neoproterozoic meta-sedimentary cover (Sinian). They are

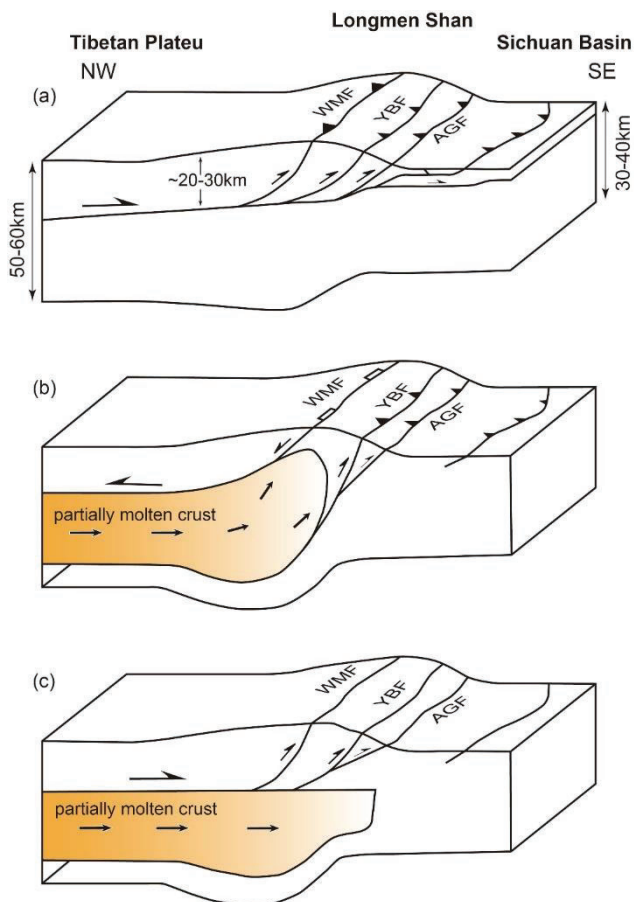


Fig.2 Conceptual models for the Cenozoic Longmen Shan evolution. Adapted from Tian et al., (2013).

a) Crustal thickening through reverse faulting (e.g., Hubbard and Shaw 2009)
b) Exhumation in front of a buoyant lower crust expelled from below the Tibetan plateau (channel flow extrusion) requiring a normal fault along the Wenchuan – Maoxian fault at the backside of the channel (e.g., Royden et al., 2008; Burchfiel et al., 2008).

c) A modified channel flow model. Flow of ductile lower crust drags the upper crust eastward to thicken the crust in the LMS through high-angle listric reverse faulting (e.g., Zhang, 2013).

WME: Wenchuan – Maoxian fault, YBF: Yingxiu-Beichuan fault, GAF: Guanxian-Anxian fault. Note that surface topography is exaggerated.

bounded by the WM and Yingxiu-Beichuan faults and structured in NW dipping slices (Fig. 1b, c) (Xu et al., 2008; Yan et al., 2011; Airaghi et al., 2017; Xue et al., 2021).

A major phase of top to the SE thrusting is evidenced by penetrative cleavage and stretching lineation in the metasediments in the Wenchuan area, and by nappe emplacement over the strongly folded Late Triassic sequences in the western Sichuan foreland basin (Burchfiel et al., 1995; Worley and Wilson, 1996; Mattauer, 1992; Yan et al., 2011). During that phase the metasedimentary rocks northwest of the Pengguan complex reached amphibolite-facies metamorphic conditions at $\sim 11 \pm 2$ kbar and ~ 620 °C (Dirks et al., 1994; Airaghi et al., 2019). These conditions were reached at ca. 224–180 Ma (Upper Triassic – Lower Jurassic) (Yan et al., 2011; Airaghi et al., 2018b; 2019; Xue et al., 2021). The Pengguan complex experienced further exhumation at ca. 140 – 120 Ma (Lower Cretaceous) (Arne et al., 1997; Airaghi et al., 2018a).

In the Longmen Shan, localized crustal shortening models are supported by observations of east-verging Cenozoic thrust faults in the foreland (e.g., Hubbard and Shaw, 2009; Hubbard et al., 2010) (Fig. 2a). Channel flow models are based instead on the lack of significant shortening across the belt both at short time scale according to GPS measurements (e.g., Zhang et al., 2004), and at longer time scale because of the absence of significant flexural basin of Cenozoic age (e.g., Burchfiel et al., 1995). Geophysical evidence for low velocity layers in the lower crust of Tibet suggest that the lower crust is soft enough for channel flow to occur (e.g., Yao et al., 2006,

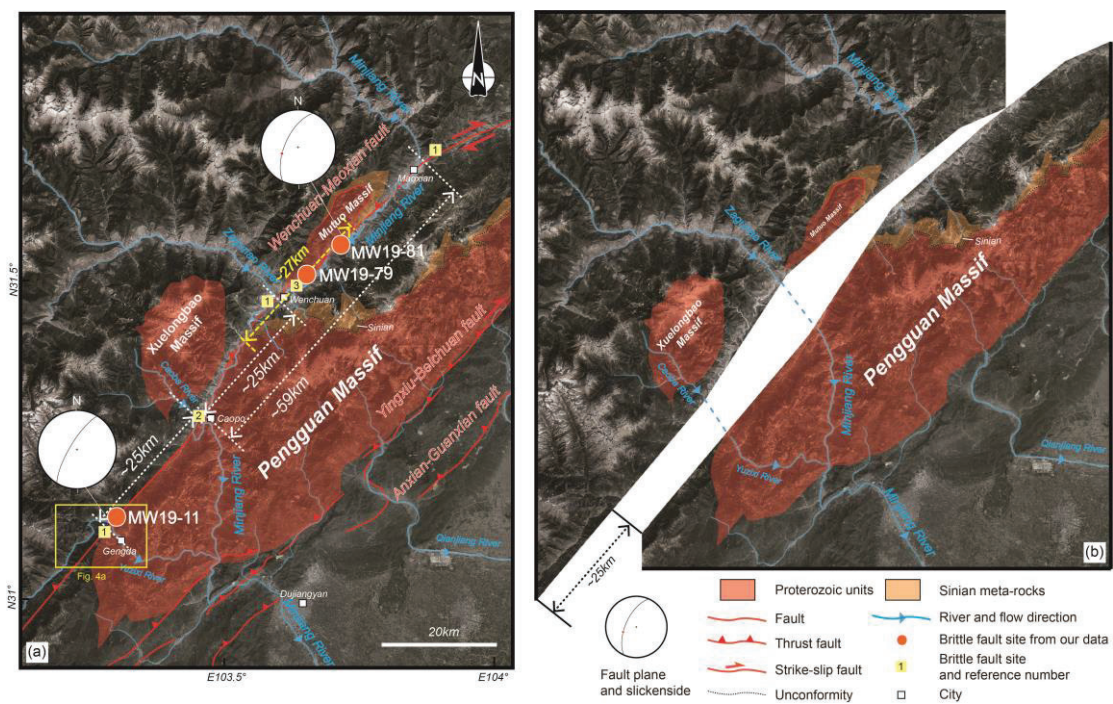


Fig. 3 The Wenchuan – Maoxian (WM) fault, geological offset and river network evolution. (a) Google earth image with major river channels, brittle faults and metamorphic complexes. River data are referenced and modified from GloRiC dataset (Dallaire et al., 2019). Faults from Li et al. (2014) and personal mapping. Orange circles indicate brittle fault sites, stereoplots show brittle fault attitude. Yellow squares and numbers indicate published brittle fault sites, 1: Dirks et al., 1994; 2: Airaghi, 2017; 3: Wang et al., 2014. (b) Reconstitution prior to right-lateral faulting assuming ~ 25 km right-lateral offset along the WM fault.

2008; Li et al., 2009). In this view, the flow of soft lower crust would have propagated eastward during the Miocene (Fig. 2b) (Royden et al., 2008). Activation of the Guanxian-Anxian and Yingxiu-Beichuan faults at the front of the LMS during the 2008 Mw7.9 Wenchuan earthquake implies that thrusting with a right-lateral component on NE-SW NW dipping faults is a major active mechanism in the Longmen Shan building (e.g., Xu et al., 2009) (Fig. 1b)

2.2.2 The Wenchuan - Maoxian fault zone.

In the Central Longmen Shan the Wenchuan-Maoxian (WM) fault zone is a ~120 km long, NE-SW striking, NW-dipping fault network that separates Proterozoic basement rocks in the south-east from metamorphosed Paleozoic sediments in the north-west (SBGMR, 1991). The fault zone underwent a polyphase history (e.g., Burchfiel et al., 1995) since the Paleozoic. Raman spectrometry measurements of carbonaceous material (RSCM) suggest the basement rocks never exceeded 360 °C, while the Paleozoic sediments that experienced temperature conditions of 450-600 °C (Airaghi et al., 2018a).

Within the WM fault zone, there is evidence for brittle deformation with fault planes, fault gouge and brecciated rocks along the WM fault (Dirks et al., 1994, Burchfiel et al., 1995; Wang et al., 2014; Airaghi, 2017) (Fig. 3a). Slickensides on fault planes are dominantly horizontal but also show pitches up to 30° SW, indicating right lateral / reverse motion for some authors (Burchfiel et al., 1995) or left-lateral for others (Dirks et al., 1994). Yet, other authors suggest pure reverse motion (Wang et al., 2014), or a more complex history with left-lateral then right-lateral motion (Airaghi, 2017). Dog-leg's river deflections and possible shutter ridges suggest that the right-lateral motion is recent and possibly still active (Burchfiel et al., 1995; Densmore et al., 2005). Some late Pleistocene fluvial terraces, dated at ~20–24 ka by radiocarbon and thermoluminescence methods, were uplifted above the Minjiang riverbed by ~20–50 m, suggesting a minimum Quaternary vertical thrust rate of ~0.5–1.1 mm/yr. across the WM fault (Li et al., 2006; Zhou et al., 2006), and a right-lateral rate of 0.8 to 1 mm/yr. (Zhou et al., 2006). However, based on the spatial distribution of the basin-wide denudation rates inferred from cosmogenic dating, Godard et al. (2010) propose that there is no significant recent differential uplift across the WM fault.

Mylonites with steep lineation are found both in the Proterozoic basement east of the brittle WM fault and in metamorphosed Paleozoic sediments in the west (Burchfiel et al., 1995, Airaghi et al., 2019; Xue et al., 2021). S/C shear criteria generally indicate top to the SE (reverse) motion, but top to NW (normal) is observed southeast of the WM fault (Xu et al., 2008; Burchfiel et al., 1995; Xue et al., 2021). ~120 km further south in the Southern Longmen Shan, Cretaceous-Paleogene ductile top to the NW (normal) deformation is found in gneiss west of the WM fault (Tian et al., 2016). However, there are no similar structures in the Central Longmen Shan, possibly because the structural evolution of the southern Longmen Shan is markedly different from than that of the central one (Airaghi et al., 2018a). West of the WM fault, the metamorphism shows a prograde path coeval with thickening with peak metamorphism reached at ~180 Ma, and retrograde evolution lasting until ~120 Ma, prior to activation of the WM fault zone sometime after 100 Ma (Airaghi et al., 2018b, 2019). East of the WM fault, white micas in mylonite showing top to the west (normal) shear criteria yield an $^{40}\text{Ar}/^{39}\text{Ar}$ weighted mean age of 26.2 ± 1.0 Ma, while other samples showing similar deformation have disturbed age spectra with apparent ages between 50 and 140 Ma (Xue et al.,

2021). These ages are interpreted to reflect episodic normal faulting from Lower Cretaceous to Miocene (Xue et al., 2021).

Low-temperature thermochronology across the fault constrains the vertical motion on the WM fault zone. Shen et al. (2019) estimate that the WM behaved as a reverse fault zone at ~ 0.6 mm/yr. since 12-15 Ma. Furlong et al. (2021) infer a more complex history with the WM fault behaving as a thrust between ~ 20 and ~ 15 Ma, then stopping before resuming at 10-6 Ma with a vertical rate >0.6 mm/yr.

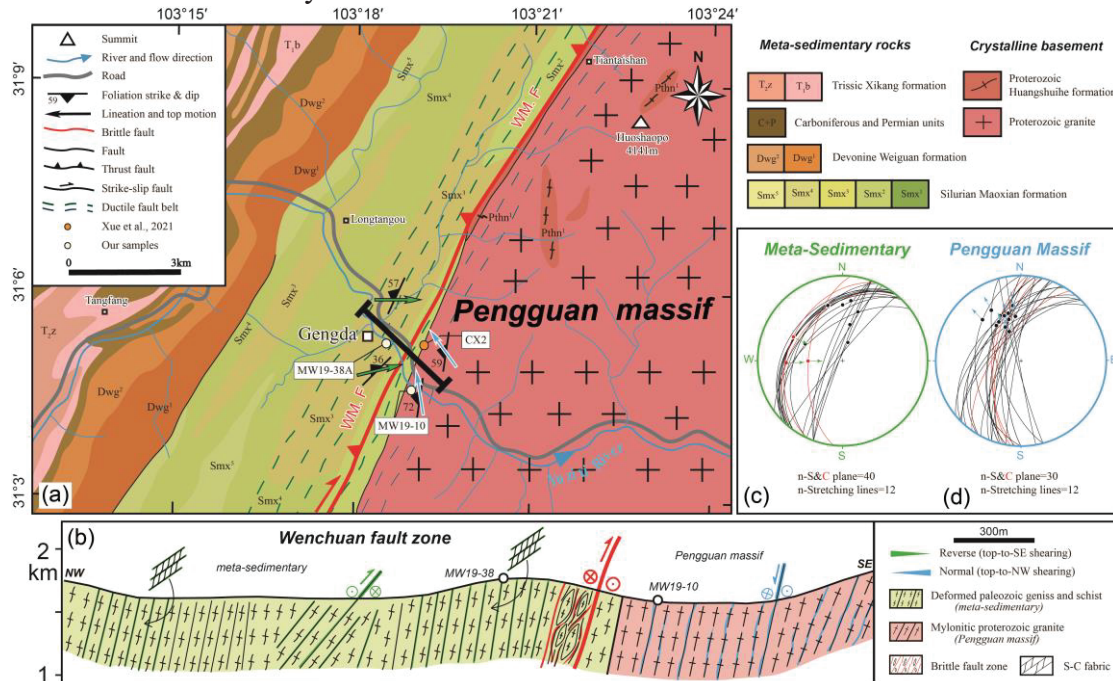


Fig. 4 Ductile deformation in the WM fault zone. a) Geological map of the Gengda area of the WM fault zone. See location on fig. 1b. b) Geological cross section through the WM fault and shear zones. c, d) Stereonet diagram of foliations and shear planes on the western side of the fault (c) and on the eastern side (d).

2.3. Field constraints on the structural evolution of the Wenchuan-Maoxian (WM) fault zone.

2.3.1 Ductile kinematics.

Our study across the WM fault near Gengda documents a ~ 3 km wide ductile deformation belt on both sides of the brittle WM fault (Fig. 4a, b). Within this belt, foliations trend $N164^\circ$ to $N150^\circ$ and dip 40° - 85° to the NW (Fig. 4c, d). Within the Paleozoic metamorphosed sediments west of the fault steep cleavage planes are cut by shallower shear planes bearing WSW-ENE trending lineation (Fig. 4c, Fig. 5a, b). These S/C relationships suggest top to the east (reverse) motion. At the microscopic scale shear criteria are sometime ambiguous, but when clear they systematically suggest top the east motion (Fig. 5c). These rocks have White mica + Chlorite + recrystallized Quartz in the shear planes and along the foliation, and Feldspar \pm Epidote porphyroclasts, with feldspars deforming brittlely (Fig. 5c).

Within the Proterozoic basement of the Pengguan massif the lineation trend to the NNW (Fig. 4d). Shear criteria are not clear in the field but in thin section they suggest top to the NW (right-lateral / normal) motion (Fig. 5f). These rocks show White mica + Chlorite +

recrystallized Quartz in the shear planes and along the foliation, and Feldspar \pm Epidote \pm Amphibole porphyroclasts in the matrix. Some of the feldspar show evidence for ductile deformation (Fig. 5f) suggesting higher deformation temperature of deformation than in the schists west of the fault. However, other factors as the deformation rate can influence the mechanical behaviour of K-feldspar during deformation. Xue et al. (2021) also report top to the NW (normal) deformation along the boundary of the Pengguan east of the WM fault. The ductile deformation zone thus appears to result from two distinct deformations: top to the east (reverse) in the Paleozoic metamorphic rocks and top to the NW (normal / right lateral) at the margin of the Pengguan. No outcrop with both deformations could be found, precluding the observation of any crosscutting relationship.

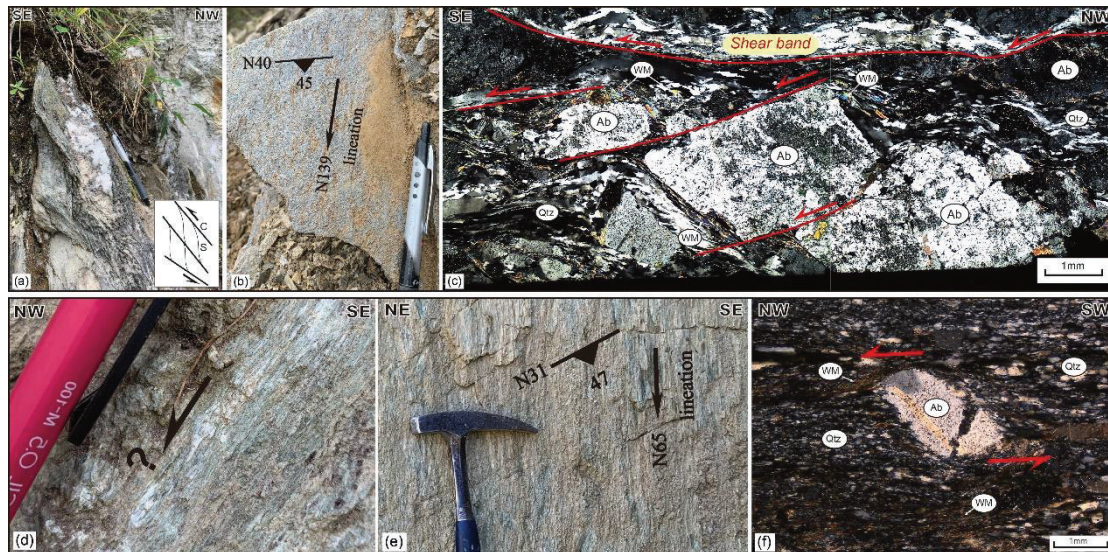


Fig. 5 Ductile deformed rocks of the WM shear zone. a - c) Top to the SE (reverse) deformation (site MW19-38A). a) S/C structure. b) Foliation and stretching lineation. c) Shear criteria in an oriented thin section of sample MW19-38A. d - f) Top to the NW (normal) deformation (site MW19-10B). d) mylonitic foliation dipping to the NW. e) Stretching lineation view from above. f) Shear criteria in an oriented thin section of sample MW19-10B.

2.3.2 Brittle kinematics.

As evoked above, some lines of evidence point to a recent dominant strike-slip motion on the brittle WM fault, with presumably a right-lateral / reverse motion (e.g., Burchfiel et al., 1995). Our own observations document brittle deformation zones at several sites along the WM fault (Fig. 3a). At site MW19-11, near Gengda, gneiss, micaschists and calcschists are affected by ductile reverse / left-lateral deformation compatible to that seen further north, east of the brittle fault. These structures are overprinted by brecciation along faults trending \sim N30° parallel to the WM fault (Fig. 3a). At site MW19-81 granites are brecciated and bounded by a clear fault plane trending N25° 61°W bearing striation with a pitch of 64°S (Fig. 3a). At site MW19-79 the WM fault crops out as a \sim 50 m thick brittle fault zone, with soft, deep dark and strongly foliated gouges, framing a grey fault breccia zone with a less organized structure (Fig. 6a, d). The fault planes strike between N38° and N65°, dip steeply to the NW and show slickensides with pitches of \sim 10° to 40° toward the SW (Fig. 6c). An oriented sample taken from the black fault gouge against the NW fault plane (Fig. 6b) shows angular quartz clasts surrounded by a

black clay-rich matrix whose foliation orientation with respect to that of the fault plane (shear plane) indicate right-lateral shear (Fig. 6e). Similar structures and Riedel shear elements can be also seen at the microscopic scale (Fig. 6f. g. h). Pitch values of striations imply a component of reverse motion.

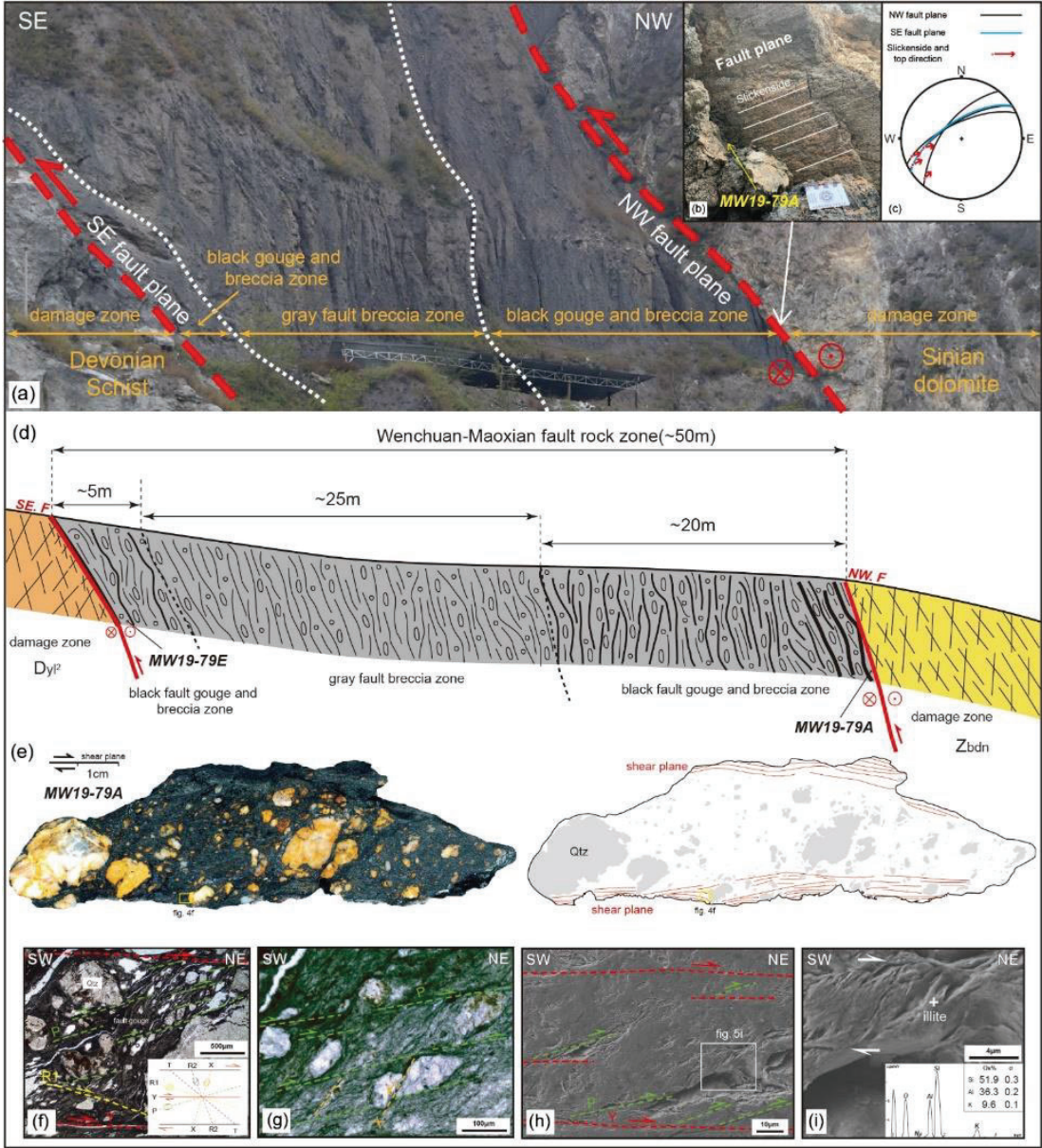


Fig. 6 Fault gouge of the Wenchuan-Maoxian fault at site MW19-79; (a) Picture of the fault zone outcrop (b) detail of the NW fault plane with sub-horizontal slickensides; (c) stereonet plot of fault planes and slickensides; (d) Fault zone cross-section showing samples location; (e, f, g, h, i) views of sample MW19-79A in the XZ plane showing “S/C” microstructures and Riedel shear elements at various scales implying right-lateral shear, red lines represent shear planes; (e, f, g) polished slab (h, i) SEM images. e) right is a line drawing of the picture on the left, with clasts in grey and shear planes in red; i) also shows the illite EDS spectrum.

2.3.3 Quantitative offset estimates.

One important aspect of the WM fault zone kinematics is that it can be constrained by bedrock geology (reflecting long-term changes in metamorphic grade) and morphology (manifesting shorter-term changes in active topography).

Total exhumation appears more important SE of the fault zone, where basement rocks are more widely exposed in the Pengguan complex (4969 m), than in the NW where such rocks only outcrop in the Xuelongbao (5313 m) and Mutuo (3455 m) ranges (Fig. 3a). This could imply that the WM fault zone is a normal fault (e.g., Royden et al., 2008). However, the metasediments NW of the fault experienced higher temperature metamorphism (450-600 °C) during the Triassic than those from the Pengguan range (≤ 360 °C) (Airaghi et al., 2018a). This rather suggests an overall reverse motion since the Triassic. From a limited thermochronology data set Godard et al., (2009) concluded that there was no significant vertical motion across the WM fault since ~11 Ma. However, from a much larger dataset Furlong et al. (2021) recently estimated ~7 km more Cenozoic exhumation of the Xuelongbao than the Pengguan, implying a reverse component of motion. Taking the base of the Sinian sedimentary cover as a piercing point across the fault suggests an apparent right-lateral offset of ~27 km (NE of both the Pengguan and Mutuo complexes; Fig. 3a and S1-1). Maps of river channel steepness do not show a strong contrast across the WM fault, suggesting that the fault has no dip-slip motion at present (Kirby and Ouimet, 2011).

Geologic markers as well as geomorphologic offset patterns such as deflected river network (e.g., Gaudemer et al., 1989) provide insight into mid- to short-term horizontal motion accumulated along the WM fault. Using the river network may not be straightforward because rivers are not passive markers. However, in the case of deeply incised rivers, lateral motion of the river-bed is greatly limited, and those rivers may be considered as clear piercing points. This is the case for the lower reach of the major Minjiang River (Fig. 3a) which is one of the only two rivers flowing across the Pengguan range in deep gorges (Fig. 1c). Upstream, the Minjiang river is strongly deflected toward the NE along the WM fault for ~59 km until Maoxian town, where it suddenly veers ~90° to flow out of the Tibetan Plateau (Fig. 3a). Taken at face value, this piercing point would suggest a ~59 km right-lateral offset since river incision. However, such offset does not realign the Zagunao river, the only other major river draining Tibet in this area (Fig. 3a), with any downstream counterpart. Furthermore, the implied river offset is more than twice as large than the geological one when it should be equal or smaller as it is necessarily younger. Taking the Zagunao river as the upper reach of the Minjiang prior to the onset of the WM fault instead yields a ~25 km offset (Fig. 3b). That offset also aligns the upstream Caoba river with the downstream Yuzixi river that is the other river flowing across the Pengguan range (Fig. 3). This offset is consistent with that seen in the geology (~27 km) (Fig. 3a and S1-1b). The ~25 km offset does not realign the upper reach of the Minjiang with any downstream counterpart, but with the Qianjiang river. However, these two rivers are now disconnected as they are separated by the Pengguan range (Fig. 3b). This could be due to the fact that uplift of the Pengguan may have been too fast for the Qianjiang to entrench, disconnecting it from the upstream river network while the Minjiang and the Yuzixi rivers eroded fast enough to cross the Pengguan. This interpretation is consistent with the detailed geometry of the river network by also matching thirteen valleys across the fault (Figs S1-1 and S1-2). Accordingly, the flow direction would have been inverted for five ~10 km-long river

stretches (8' to 13') by the fast uplift of the Pengguan. While tentative, such reconstruction provides the simplest scenario for the recent river network evolution, in particular by accounting for the fact that the WM fault, for which there is clear evidence of strike-slip motion, did necessarily offset the river network. Integration of the river offset pattern with the finite-strain structural-metamorphic record is discussed further in Sections 5.1 and 5.2 based on temporal constraints described below.

2.4 Temporal constraints

2.4.1 K-Ar dating of fault gouge

Dating of fault gouge can constrain the timing of brittle deformation (Vrolijk et al., 2018). Natural fault gouge usually contains a mixture of two illite polytypes, $2M_1$ and $1M_d$. Only $1M_d$ polytype is considered to form simultaneously with faulting and usually has a size $< 2 \mu\text{m}$, in contrast to the larger $2M_1$ polytype inherited from wall-rock material. The age of the $1M_d$ polytype would thus tend to be closer to that of deformation while that of the $2M_1$ will be inherited (Haines and van der Pluijm, 2008). Considering the fine grain size of illite mineral, the K-Ar method is more appropriate than the $^{40}\text{Ar}/^{39}\text{Ar}$ because of recoil effects during neutron irradiation (Clauer, 2013). We present results from two fault gouge samples taken at site MW19-79 near both fault planes framing the gouge zone (Fig. 6d, see detail in table 1). The samples were disaggregated and separated via gravitational floating and centrifugation to isolate clay fraction with four sizes, 1-2, 0.5-1, 0.25-0.5 and $<0.25 \mu\text{m}$, which were then characterized using X-ray diffraction and analysed with PROFEX software to quantify illite polytypes (Bergmann et al., 1998) (Fig. S2-1, S2-2; table S2-1). Each size fraction was dated using the K-Ar method as described by Zheng et al., (2014), and ages are plotted against the percentage of $2M_1$ polytype (Fig. 7, Tables S2-2, S2-3). Details on the analytical procedure are found in Zheng et al. (2022).

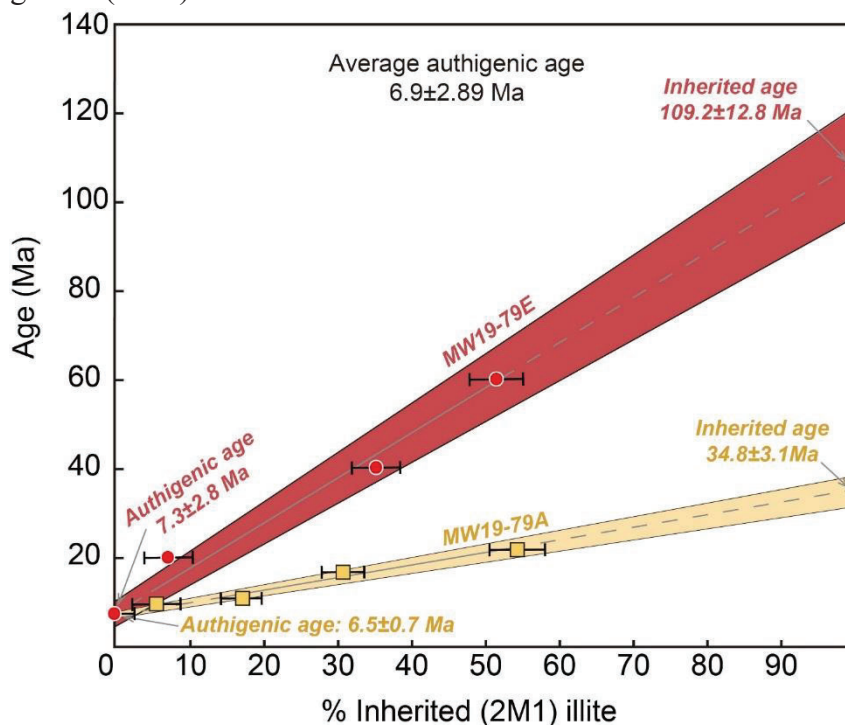


Fig. 7 Illite age plot of samples MW19-79A and MW19-79E.

Sample MW19-79A that shows clear indication for right lateral deformation comes from the vicinity of the NW fault plane (Fig. 6e, f, g). Ages for the four fractions vary between 6.9 and 21.2 Ma, while proportion in $2M_1$ illite varies between 0 and 54.08 % (Table S2-3). York regression of the four ages with respect to the $2M_1$ percentage yield a 6.5 ± 0.7 Ma age at the lower (0%) intercept, and 34.8 ± 3.1 Ma at the upper (100%) intercept (Fig. 7).

MW19-79E sampled in the black gouge in vicinity of the SE fault plane yield ages between 9.6 and 60.2 Ma, while proportion in $2M_1$ illite varies between 5.64 and 51.5 % (Table. S2-3). Regression of the four ages yield 7.3 ± 2.8 Ma at the lower intercept, and 109.2 ± 12.4 Ma at the upper one (Fig. 7).

XRD analysis of both samples show that the only K-bearing minerals are illite (Table S2-1). Illites are strongly oriented by the right-lateral deformation (Fig. 6g, h). For both sample the apparent ages decrease linearly with the $2M_1$ illite (inherited) content, and the two lower intercepts are identical within error while the two upper intercept ages are clearly distinct. We interpret this as reflecting a single $1M_d$ (authigenic) growth event at 6.9 ± 2.9 Ma (upper Miocene) affecting two distinct host rocks that yield ages of 109.2 ± 12.4 Ma in the SE and 34.8 ± 3.1 Ma in the NW. The fault gouge results from brittle deformation of the host/parent rocks at temperature ≤ 200 °C, and crystallization of illite in fault gouge occurs between 110 °C and 180 °C (Duvall et al., 2011; Mottram et al., 2020). We thus interpret the $1M_d$ growth event as resulting from motion along the brittle WM fault, and the ages as yielding a minimum age for the onset of that fault. The fact that the ages record a common resetting age, but a distinct inherited component precludes temperature to have exceeded ~ 260 °C after faulting (Hunziker et al., 1986).

2.4.2 White mica $^{40}\text{Ar}/^{39}\text{Ar}$ dating

$^{40}\text{Ar}/^{39}\text{Ar}$ is applicable to *in situ* dating of fabric-forming minerals, particularly white micas crystallized (or recrystallized) in schistose and mylonitic rocks (Di Vincenzo et al., 2016; Laurent et al., 2021). Combined with conventional step-heating, the technique can provide temporal constraints on deformation stages recorded by composite fabrics formed near the brittle-viscous transition at greenschist-grade conditions (Beaudoin et al., 2020). We present *in situ* laser and step heating $^{40}\text{Ar}/^{39}\text{Ar}$ dating of white mica for sample MW19-38A showing top to the SE deformation (Fig. 5c), and MW19-10B showing top to the NW deformation (Fig. 5f). Details on the technique are given in S3, structural information is reported in table 1.

Micaschist MW19-38A was collected in Paleozoic metamorphic rocks with S/C relationships indicating top to the SE (reverse) deformation ~ 200 m NW of the brittle WM fault (Fig. 4a). Ductile quartz, white mica and chlorite layers constitute the shear bands but feldspar porphyroclasts are brittlely deformed (Fig. 5c). This suggests deformation temperature < 450 °C (Sibson 1992), more probably close to 310-350°C (Stöckhert et al., 1999). Using Bourdelle and Cathelineau (2015) thermometer that is accurate for temperatures ≤ 350 °C, chlorite composition yield temperature estimates between 170 and ≥ 350 °C, with most data (46%) at ~ 350 °C (Fig. S11; table S11-1). Quantitative composition maps of the white mica (see S8 for the analytical procedure) shows two generations of white mica based on their celadonite (Xcel) content. One has Xcel < 0.2 , while the other has higher Xcel up to 0.4 (Fig. 8a) (Fig. S4-1). *In situ* $^{40}\text{Ar}/^{39}\text{Ar}$ dating yield apparent ages between ~ 10 and 600 Ma with most ages ≤ 30 Ma (Figs. 8a, c, S4-1, S4-2; Table S4-1). White micas with low Xcel (Xcel < 0.2) have younger apparent ages (< 20 Ma) than the ones with higher Xcel (> 300 Ma). Among the youngest ages, forty-nine spots define an average of 15.4 ± 0.2 Ma (MSWD = 1.35) (Fig. 8c). The companion

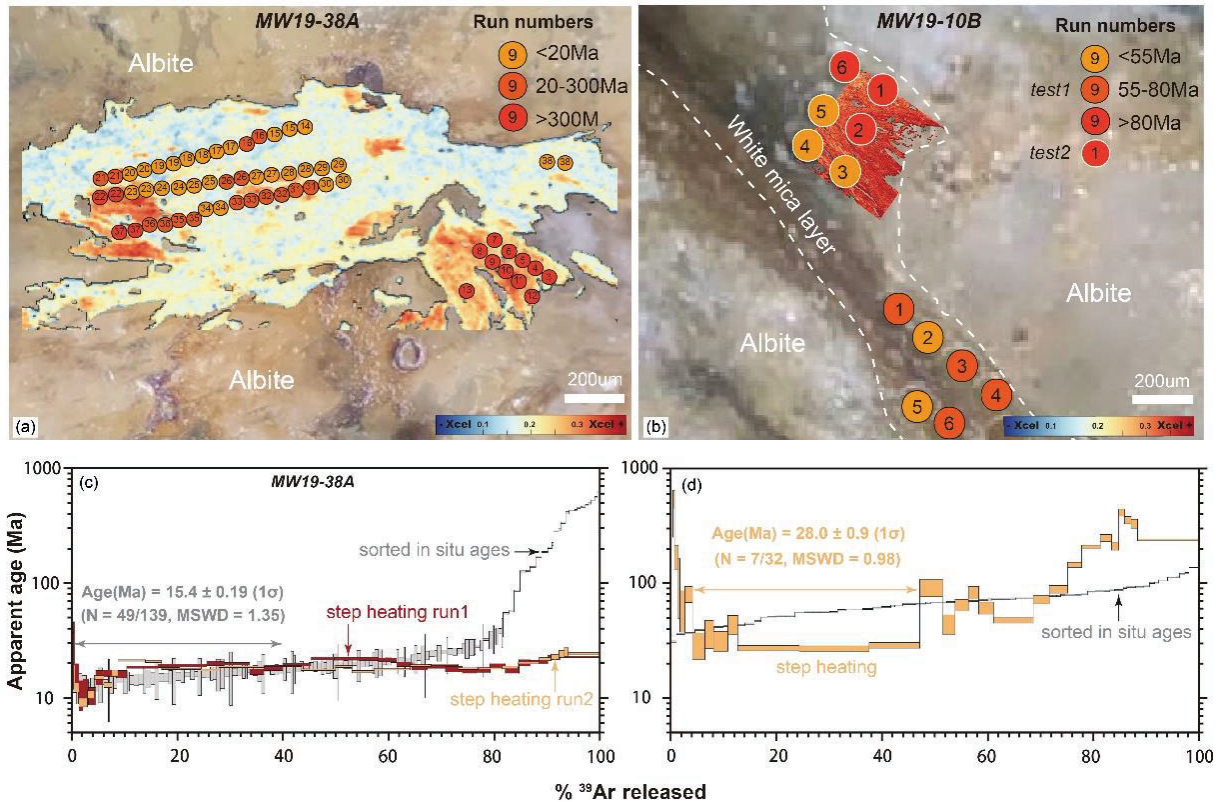


Fig. 8 $^{40}\text{Ar}/^{39}\text{Ar}$ dating results of ductile deformation of samples MW19-38A (a and c), and MW19-10B (b and d). (a) and (b) in situ laser ablation map with spot numbers. Spot colours refer to apparent ages. The background is thin section (reflective light) or chemical composition (X Celadonite) when available. c) age spectra (two runs) and sorted in situ ages of sample MW-38A. d) age spectra and sorted in situ ages of sample MW-10B.

step heating runs yield relatively flat age spectra with ages between 10 and 23 Ma, with a large fraction of the ages consistent with the young in situ component at ~15 Ma (Fig. 8c, Table S5). Our interpretation is that the micas with Xcel > 0.3 are porphyroclasts inherited from an early event (≥ 600 Ma) while the younger age of the Xcel < 0.2 micas record a younger fluid-rock interaction event responsible for the growth of secondary white micas and chlorite between 250 and 350 °C during top to the east deformation. That temperature is lower than the closure temperature of white micas for the K/Ar system of 400-445 °C (Harrison et al., 2009) and recently revised theoretical and empirical estimates (Nteme et al., 2022, 2023) implying that the 15.4 ± 0.2 Ma (middle Miocene) age correspond to white mica crystallization, not cooling.

Micaschist MW19-10B from ~200 m SE of the brittle WM fault (Fig. 4a) shows top-to-NW right-lateral / normal shear planes underlined by recrystallized quartz and white mica (Fig. 5f). Chemical composition of the white mica shows moderate variation in Xcel content between 0.2 and 0.4 % (Fig. 8b; S6-1a). Chlorite compositions yield temperature estimates between 315 and ≥ 350 °C, with one outlier at 160 °C, and most data (37%) at ~350°C (Fig. S11; table S11-1). In that part of the Pengguan range RSCM data east of the WM fault suggest that temperature never exceeded 360 °C (Airaghi et al., 2018a). In situ $^{40}\text{Ar}/^{39}\text{Ar}$ dating yield apparent ages between 30 and 140 Ma (Fig. 8b, d, S6-1, Table S7). The step-heating spectrum displays a flat (concordant) segment at 28.0 ± 0.9 Ma in the early gas release (4% to 48% of the total ^{39}Ar), consistent with the youngest component of the in-situ data (Fig. 8d, Table S7). Step-ages then climb up to ~450 Ma, indicating an inherited high-temperature component. Our interpretation

is that the top to the NW (normal / right lateral) ductile deformation occurred at 300-360 °C inducing feldspar deformation and chlorite and white mica (re)-crystallization at 28.0 ± 0.9 Ma (Middle Oligocene), while a previous metamorphic event occurred at ≥ 140 Ma. This deformation age is fully consistent within error with the $^{40}\text{Ar}/^{39}\text{Ar}$ step-heating age of 26.2 ± 1.0 Ma inferred to date normal deformation from white micas sampled less than 1 km away (Xue et al., 2021). The deformation temperature is below the 400-445 °C closure temperature of white micas for the K/Ar system, implying crystallization rather cooling age (see above).

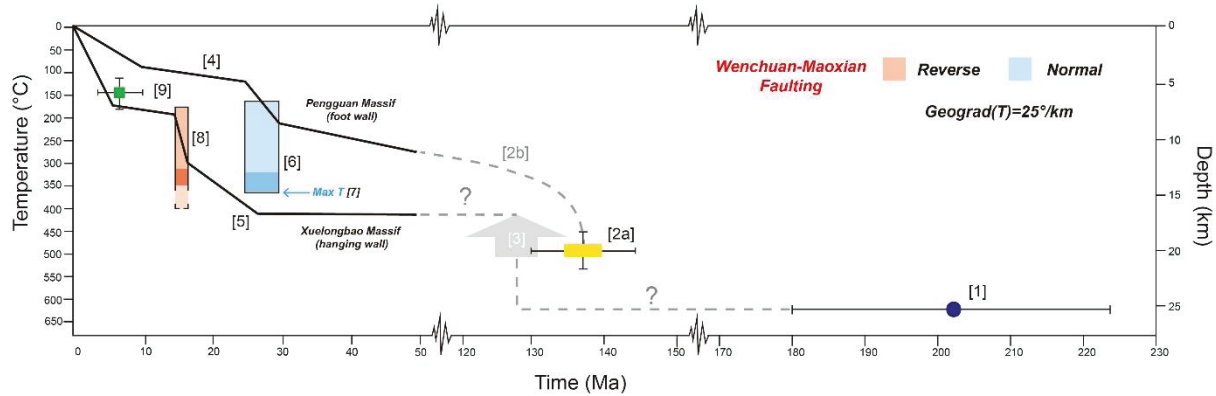


Fig. 9 Exhumation – cooling history of the Pengguan and Xuelongbao massifs. [1] P-T estimate of Lower Jurassic metamorphism in Xuelongbao (Airaghi et al., 2018b). [2a] Lower Cretaceous P-T estimate (Airaghi et al., 2017), and [2b] Lower Cretaceous cooling path (Airaghi et al., 2017) of Pengguan. [3] Amount of Early Cretaceous exhumation of Xuelongbao (Li et al., 2023). [4] Exhumation history of the Pengguan range (Wang et al., 2012). [5] Exhumation history of the Xuelongbao range (Tian et al., 2013; Furlong et al., 2021). [6]. Temperature estimate of the top to the northwest (right-lateral / normal) deformation (MW19-10B) (this study), with [7] maximum estimate from RSCM (Airaghi et al., 2018a). [8] Temperature estimate of top to the SE (reverse) deformation (MW19-38A) (This study). [9] Gouge formation at site MW19-79 (this study). Correspondence between depth and temperature assuming a geothermal gradient of 25°C/km.

2.5 Discussion

2.5.1 Timing of brittle and ductile deformation in the WM fault zone

Fault gouge K/Ar dating at site MW19-79 indicates that brittle faulting was ongoing along the WM fault at 6.9 ± 2.9 Ma (~7 Ma, upper Miocene). Such faulting is dominantly right lateral with a slight reverse component (pitch between 10° and 40° S). Our $^{40}\text{Ar}/^{39}\text{Ar}$ data indicate that top to the east (reverse) deformation occurred in the Paleozoic schists at 15.4 ± 0.2 Ma (~15 Ma, middle Miocene), while top to the northwest (normal / right lateral) took place at the margin of the Pengguan complex at 28.0 ± 0.9 Ma (~28 Ma, Middle Oligocene).

The right-lateral fault kinematics with a slight reverse component are compatible with the ~25 km right-lateral offset of the river network (Fig. 3) and the higher altitude of the Xuelongbao complex with respect to the Pengguan (Fig. 1c).

The ductile top the east (reverse) shear along the WM fault zone is usually ascribed to the amphibolite-grade deformation that affected the whole Paleozoic metasediments north of the Pengguan range during the Upper Triassic and created the nappes in the external part of the Longmen Shan (Airaghi et al., 2018a; Xue et al., 2021). Our age of deformation at 15.4 ± 0.2

Ma points to a clearly much younger event (middle Miocene) of reverse shear restricted to the WM fault zone between the Xuelongbao and Pengguan ranges (see below).

The age of top to NW (normal) shear along the NW boundary of the Pengguan range was poorly constrained so far and some have proposed that it could correspond to a major detachment fault (Wang et al., 2014). Based on three white mica $^{40}\text{Ar}/^{39}\text{Ar}$ age spectra, Xue et al. (2021) proposed that deformation occurred episodically at 141–120 Ma, 81–47 Ma, and 27–25 Ma. These Cretaceous and Paleocene ages are deduced from complex age spectra possibly affected by mixed ages (partial resetting), in the same way as the older components seen in our data (cf. Section 4.2). In contrast, our *in situ* approach clearly resolves, and confirms, their Middle Oligocene age with a robust estimate at 28.0 ± 0.9 Ma. This Miocene age is further compatible with the exhumation histories of the Pengguan and Xuelongbao ranges (see below).

2.5.2 Differential uplift across the WM fault zone

Independent but complementary to direct dating of faults and mylonite, quantitative kinematics can be deduced from thermochronological modelling of cooling due to exhumation in the hanging (thrust) or footwall (normal fault) of fault systems.

During the lower Cretaceous, the Pengguan massif experienced a metamorphic event at conditions of 7 ± 1 kbar, 280 ± 30 °C (Airaghi et al., 2017). Low-temperature thermochronological data (ZHe, AFT, and AHe) staggered over more than 3000 m of differential height within the Pengguan range further constrain the range cooling history suggesting that slow, steady exhumation during early Cenozoic was followed by two pulses of rapid exhumation, one beginning 30–25 Myr ago and a second 10–15 Myr ago and still active today (Godard et al., 2009; Kirby et al., 2002; Wang et al., 2012) (Fig. 9). The temperature conditions estimated for sample MW19-10B at ~28 Ma appear to be ~100 °C higher than the cooling path of the Pengguan (Wang et al., 2012) (Fig. 9). This is probably because that path is inferred from samples located in the central and eastern Pengguan far away from the WM fault while MW19-10B is from the fault zone close to the Pengguan.

West of the WM fault, the Upper Triassic – Lower Jurassic metamorphism (11 ± 2 kbar and ~620 °C) (Dirks et al., 1994; Airaghi et al., 2018b; 2019; Xue et al., 2021) was followed by ~2-4 km exhumation in the Early Cretaceous (~120-135 Ma) (Li et al., 2023) (Fig. 9). Cooling / exhumation resumed in the Cenozoic and Tian et al., (2013) interpreted faster Late Cenozoic exhumation rates deduced from ZHe ages in the Xuelongbao than in the Pengguan as due to out of sequence thrusting on the WMF. This was confirmed by Shen et al. (2019) who, using Pecube-based inverse modelling of ZFT, ZHe, and AHe data from two transect spanning ~3300 m in elevation in the Xuelongbao, infer an exhumation rate of 0.9 – 1.2 mm/yr from ~13 Ma to present. Inverse 1D modelling using the TQTec code of ZFT, AFT, and AHe data spanning nearly 3900 m of altitude, lead Furlong et al. (2021) to propose a more complex history with an earlier start of exhumation at ~27 Ma, a fast exhumation at 2 mm/yr between 17 - 15 Ma and a final stage at ~1 mm/yr since ~6 Ma (Fig. 9). The temperature conditions estimated for sample MW19-38A are compatible with that cooling history (Fig. 9).

Both the Xuelongbao and Pengguan massif appear to share a nearly identical onset of Cenozoic exhumation at ~30 Ma (Fig. 9), pointing to a major regional event. Exhumation of the Xuelongbao massif (~16 km) is however significantly greater than that of the Pengguan Massif (~10 km). Analysis of the differential exhumation between both massifs allows the timing and rate of vertical motion on the WM fault zone to be discussed. The differential vertical rates across the west dipping WM fault zone calculated from the more likely models of

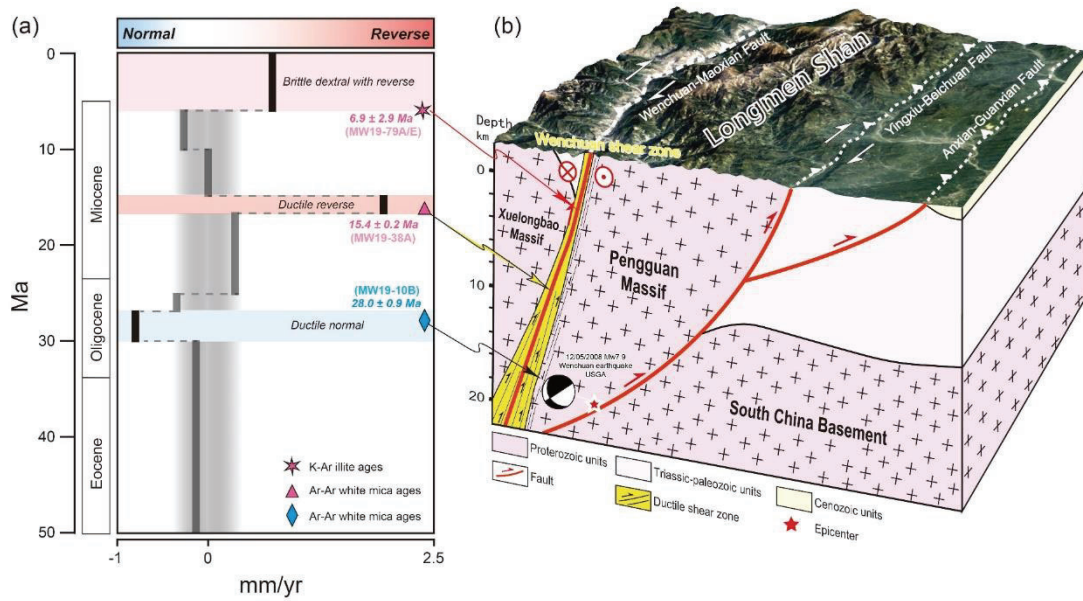


Fig. 10 Kinematics of the Wenchuan-Maowen fault. (a) vertical differential exhumation across the fault according to thermochronological data of the Pengguan and Xuelongbao ranges (Furlong et al., 2021; Wang et al., 2012). Negative values correspond to normal motion on the NW dipping fault, and positive to reverse motion. (b) structural bloc diagram of Longmen Shan in shallow crust.

Wang et al. (2012) for Pengguan and Furlong et al. (2021) for Xuelongbao (Fig. 9) indicate four main kinematic stages (Fig. 10a). 1) A normal motion at the onset of global exhumation (~ 30 Ma) until ~ 25 Ma, with a vertical rate between 0.79 and 0.40 mm/yr (~ 3.2 km of relative subsidence of the Xuelongbao). 2) A reverse motion until ~ 15 Ma, with a maximum rate of 1.93 mm/yr (relative uplift of ~ 6.3 km). 3) Negligible vertical motion until ~ 6 Ma at ≤ 0.26 mm/yr. 4) Reverse motion since ~ 6 Ma at 0.72 mm/yr (relative uplift of ~ 4.2 km). The timing of these relative vertical motions is strikingly similar to the deformation style and absolute timing found in this study in at least three respects.

First, the age of brittle faulting at ~ 7 Ma closely matches the final exhumation starting at ~ 6 Ma. Since 6 Ma, the total exhumation of Xuelongbao would be of ~ 7 km, ~ 5 km greater than Pengguan (Furlong et al., 2021). Preservation of the 25 km right-lateral offset of the river network despite erosion suggests that it dates back to the onset of the last exhumation event in the hanging wall (i.e. ~ 6 Ma). This would correspond to a horizontal strike-slip rate of ~ 4.2 mm/yr. Brittle motion on WM fault is mostly strike-slip but involves a significant uplift of the NW compartment. The pitch angle of the slickensides measured in the field ($\sim 11^\circ$ S, Fig. 6c) is consistent with the direction of motion calculated assuming a vertical rate of ~ 0.72 mm/yr, a horizontal rate of 4.2 mm/yr, and a fault dip angle of 65° - 70° ($\sim 12^\circ$ S). The thrusting component is responsible for the exhumation of the western compartment (hence the entrenchment of the river network) following a ~ 9 yr long period of negligible exhumation. The actual strike-slip motion may have started slightly before the exhumation became substantial, possibly explaining why the apparent horizontal geological offset is slightly larger than the morphological one (27 vs 25 km) (Figs. 3b, S1-1b).

Second, the Miocene phase of reverse faulting starting at ~ 25 Ma peaked at 1.93 mm/yr around 16.6-14.8 Ma, coinciding with the 15.4 ± 0.19 Ma age of reverse motion recorded by

our sample MW19-38A. Top to the east thrusting thus lasted until the middle Miocene (25-15 Ma) along the ductile WM fault zone to produce ~6.3 km more exhumation in Xuelongbao than in Pengguan. Given the average dip of the motion on the shear planes (45°, Fig. 4c), this corresponds to a shortening of ~6.3 km in the E-W direction.

Third, normal motion on the WM fault zone from ~30 Ma until ~25 Ma at a vertical rate of 0.79 – 0.4 mm/yr., is coeval with deformation ages of 28 ± 0.9 Ma (sample MW19-10B, this study) and 26.2 ± 1.0 Ma (sample CX2, Xue et al., 2021) associated with ductile normal/ right lateral deformation. Given the lineation attitude (Fig. 4d), the ~3.2 km of subsidence corresponds to ~2.7 km of stretching in the N350° direction (~50° dip). Such normal / right lateral motion on the WM fault zone resulted from differential motion with respect to Pengguan while both massifs were rising, most probably above a sole thrust corresponding to the Yingxiu-Beichuan and Wenchuan-Maoxian faults.

2.5.3 Cenozoic faulting and building of Longmen Shan

The kinematic history of the WM fault zone discussed above shed new light on the Longmen Shan tectonics during the Cenozoic and the accompanying deformation / uplift mechanisms.

The onset of exhumation of central Longmen Shan in the Oligocene (~30 Ma) is interpreted as due to thrusting on a sole thrust dipping to the NW, presumably the Yingxiu-Beichuan fault (Hubbard and shaw, 2009; Wang et al., 2012; Shen et al., 2019). A similar timing of exhumation is reported at other locations along the eastern Tibetan margin (Cao et al., 2019; Zhu et al., submitted). This led Zhu et al. (submitted) to propose that a ~800 km long thrust fault, the Yulong-Muli-Jinpingshan-Longmenshan (YMJL) bounded eastern Tibet before being offset by the Xianshuihe strike-slip fault. Normal motion with a large right-lateral component occurred along the WM fault zone at that time. As we show, this was linked to differential uplift, whose effective cause needs to be elucidated yet. What is clear however, is that since the onset of Cenozoic building of the Tibetan plateau, the WM fault never experienced pure normal motion, and no normal motion at all since the Oligocene.

The total Cenozoic exhumation of the Xuelongbao is ~16 km (Furlong et al., 2021). Significant top to the east thrusting occurred during the middle Miocene (27-15 Ma) along the ductile WM fault zone inducing ~13 km of exhumation (Furlong et al., 2021) in the internal part of the Longmen Shan. At that time, exhumation (and thus probably thrusting above the sole thrust) was slower in the externally located Pengguan massif. This implies out-of-sequence thrusting with respect to the previous activation of the sole thrust in the Oligocene. Thrusting on the frontal Guanxian-Anxian and Yingxiu-Beichuan is still active as shown by the Wenchuan earthquake (Fig. 1b) implying that the main locus of thrusting has migrated back to the frontal part. This implies a more complex organization of thrusting on the eastern Tibet margin than a classical external propagation model would suggest, as already proposed for the Yalong margin further south (Pitard et al., 2021; Zhu et al., submitted). This kind of thrusting pattern could be linked to the steepness of faults such as the WM fault zone, and possibly also to a significant strike-slip component of motion. The steepness of the thrust could also explain the absence of significant flexural basin.

The recent kinematics of the WM fault are characterized by right-lateral shear with a reverse component. Such motion is consistent with the 2008 Mw7.9 Wenchuan main shock focal mechanism (USGS) which has been documented on a NE-SW striking NW dipping fault, and Yingxiu-Beichuan surface ruptures (Fu et al., 2011) (Fig. 1b). This indicates that present-day kinematics of these major faults in Longmen Shan are comparable to those having prevailed

during the upper Miocene. However, the absence of surface break along the WM fault during the Wenchuan mega-earthquake suggests that it could be now inactive with right-lateral motion being transferred on the parallel and more external Yingxiu-Beichuan fault.

2.5.4 Cenozoic building of the Tibetan eastern margin: channel flow or crustal stacking?

Lateral extrusion of partially molten crustal material outward from below Tibet has been widely proposed to explain the steep boundaries of the Tibetan plateau. (e.g., Clark and Royden, 2000; Beaumont et al., 2001; Clark et al., 2005b; Cook and Royden, 2008; Adams and Hodges, 2022). In the Longmen Shan, the Pengguan metamorphic complex is composed of NeoProterozoic granites without any trace of Cenozoic melting. Crustal extrusion would result from growth of the deep crust in a weak layer pushing the Pengguan range and inducing thrusting along the Yingxiu-Beichuan fault and normal faulting along the WM fault (Fig. 2b) (e.g., Royden et al., 1997; Clark et al., 2005a; Burchfield et al., 2008, Royden et al., 2008). However, we clearly document that the WM fault has not been normal since the Oligocene implying that extrusion at the front of a crustal channel flow did not occur in the Longmen Shan in the Cenozoic.

According to the rheology of the lower crust, numerical models of crustal channel flow do not necessarily imply extrusion of the crust at the surface but can result in tunnelling or formation of domes or nappes at depth (Beaumont et al., 2006; Jamieson et al., 2013). Some have proposed that the Longmen Shan thrust wedge would be pushed from below by a lower channel flow originated from below Tibet (Fig. 2c) (Zhang, 2013). Such hypothesis is difficult to test from geological observations at the surface. Zones of high electrical conductivity (Bai et al., 2010) and low shear wave speed (Li et al., 2009; Yao et al., 2008) in east Tibet appear to support Channel flow. Seismic tomography confirms that the Longmen Shan is an important boundary between the thick Songpan block with its LVZ's and the thinner and more rigid Sichuan crust (e.g., Li et al., 2009; Robert et al., 2010; Liu et al., 2014). However, other geophysical experiments revealed that the LVZ are not as continuous as previously envisaged and that present-day widespread channel flow appears dubious (e.g., Hetényi et al., 2011; Yao et al., 2010; Zhao et al., 2012; Li et al., 2014). Further analysis of geophysical images shows that the LVZs are within the Songpan Block and stop ~25 km west of the Longmen Shan (e.g., Zhao et al., 2012). Dragging of the upper crust should thus not occur below the Longmen Shan as inferred by Zhang (2013) model (Fig. 2c) but west of the WM fault where there is no reverse fault nor significant relief.

We conclude that crustal channel flow is not, and has not been at least since the Oligocene, the active mechanism that would have produced and maintained the steep LMS topography. The LMS rather results from crustal stacking in an accretionary prism, with a large strike-slip component and out of sequence thrusting on steep thrusts.

2.6 Conclusions

Combining field analysis with direct deformation dating (K-Ar on fault gouge and $^{40}\text{Ar}/^{39}\text{Ar}$ on white micas) and thermochronology, we constrain the kinematics and exhumation history of the Wenchuan-Maowen (WM) fault zone that is key to decipher between the various models proposed for Cenozoic building of the eastern Tibetan plateau margin (Longmen Shan). The WM fault zone records onset of exhumation of the Longmen Shan in the Cenozoic with various steps across the viscous/brittle regime during progressive exhumation. Coupled structural analysis and in situ dating shows that, at the onset of exhumation in the Middle Oligocene (~30 - 25 Ma), the fault was right-lateral /normal while thrusting was taking place on a deeper, more

external part of the Yulong-Muli-Jinpingshan-Longmenshan thrust belt. In the middle Miocene (25-15 Ma), out-of-sequence thrusting along the WM fault zone was active while thrusting on the basal thrust was decelerating, inducing ~6 km of differential exhumation between the Xuelongbao and Pengguan ranges. After a ~9 Myr pause, exhumation of the Xuelongbao resumed during the upper Miocene (~6 Ma) with the activation of the brittle right lateral / reverse WM fault that accrued ~25 km of right lateral offset, now visible in the river network. Such deformation is still active in the Longmen Shan but it is unclear whether this is so across the WM fault today. The MW fault zone never showed pure normal motion, dismissing a lower crustal channel flow extrusion model for building what has often been considered as one archetype example of such mechanism: the east Tibet topographic step. This topography rather results from crustal shortening, including activation of steep out of sequence reverse faults with significant right-lateral component.

Supplementary material

S1 River network evolution around the Wenchuan-Maoxian (WM) fault

S2 Results Illite dating MW19-79A and MW19-79E

S3 Analytical procedure for $^{40}\text{Ar}/^{39}\text{Ar}$ dating

S4 Sample MW19-38A in situ $^{40}\text{Ar}/^{39}\text{Ar}$ data

S5 Sample MW19-38A step heating $^{40}\text{Ar}/^{39}\text{Ar}$ data

S6 Sample MW19-10B in situ $^{40}\text{Ar}/^{39}\text{Ar}$ data

S7 Sample MW19-10B step heating $^{40}\text{Ar}/^{39}\text{Ar}$ data

S8 Microprobe analytical procedure and X map tool

S9 Microprobe results of MW19-38A and EMPA location

S10 Microprobe results of MW19-10B and EMPA location

S11 Temperature estimate MW19-38A and MW19-10B

3 The Wenchuan shear zone and the deformation history of the Longmen Shan

3.1 Introduction

During the Cenozoic, the Tibetan Plateau arose as a result of the ongoing Indo-Eurasian collision (Yin and Harrison, 2000; Guillot et al., 2003), which produced not only great relief at the surface, but also a thick lithospheric crust with a complex structure at depth (Tapponnier et al., 2001; Replumaz et al., 2010). At the eastern margin of the plateau, the NE-SW striking Longmen Shan (LMS) belt towers nearly 5000 m above the Sichuan basin at a horizontal distance of less than 50 km, which was regarded as the world's steepest topographic slope. Such steep topography is thought to form mainly during the Cenozoic time, undergoing two pulses of rapid uplift from 30-25 Ma and 15-10 Ma (Wang et al., 2012). The LMS consists of three main NW-dipping faults, from the west to east, Wenchuan-Maoxian fault, Yingxiu-Beichuan fault and Anxian-Guanxian fault. Previous studies considered that

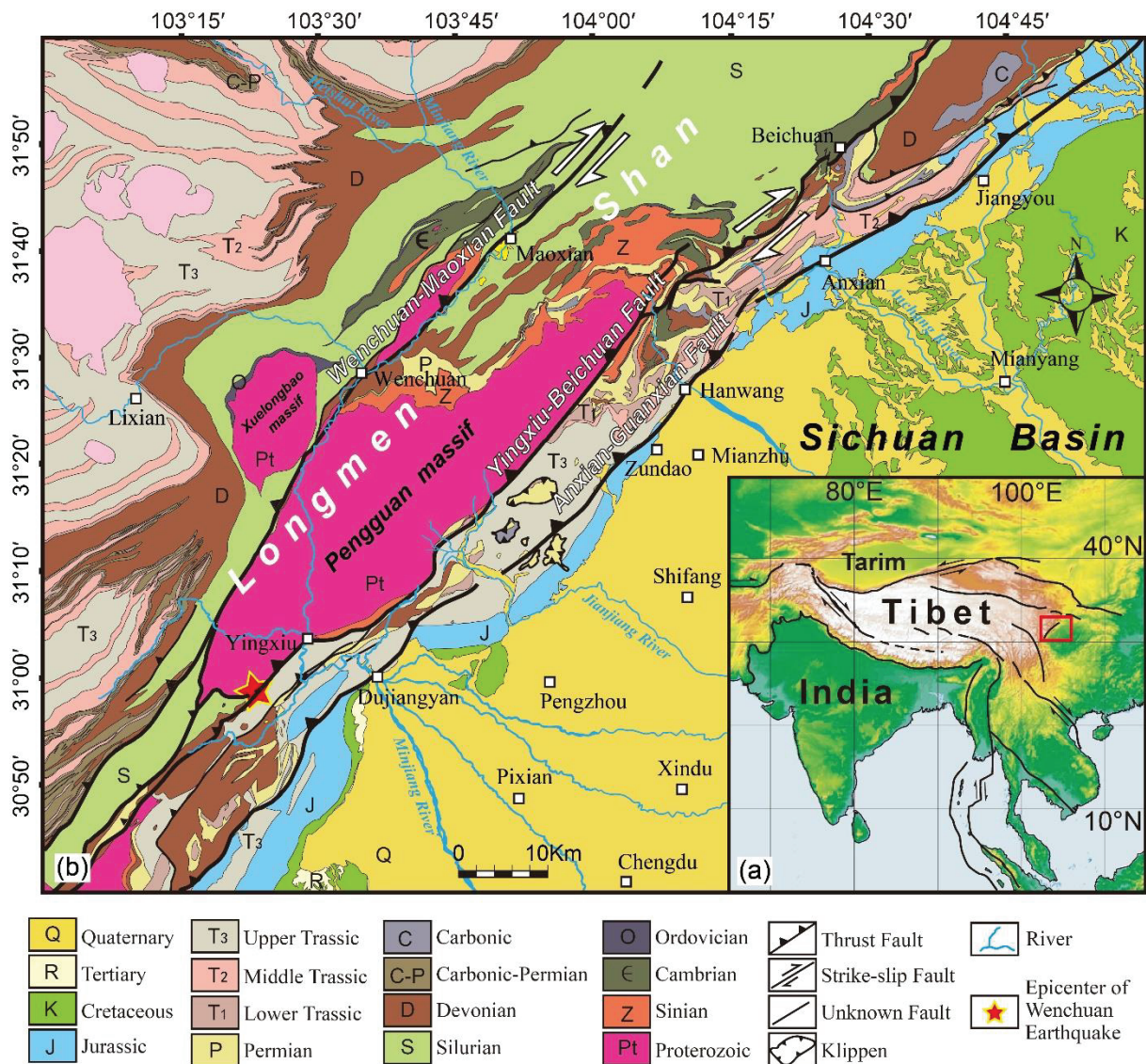


Fig1 (a) Geomorphological map of Tibet plateau, red square is the location of Longmen Shan;(b) Geological map of Longmen Shan area

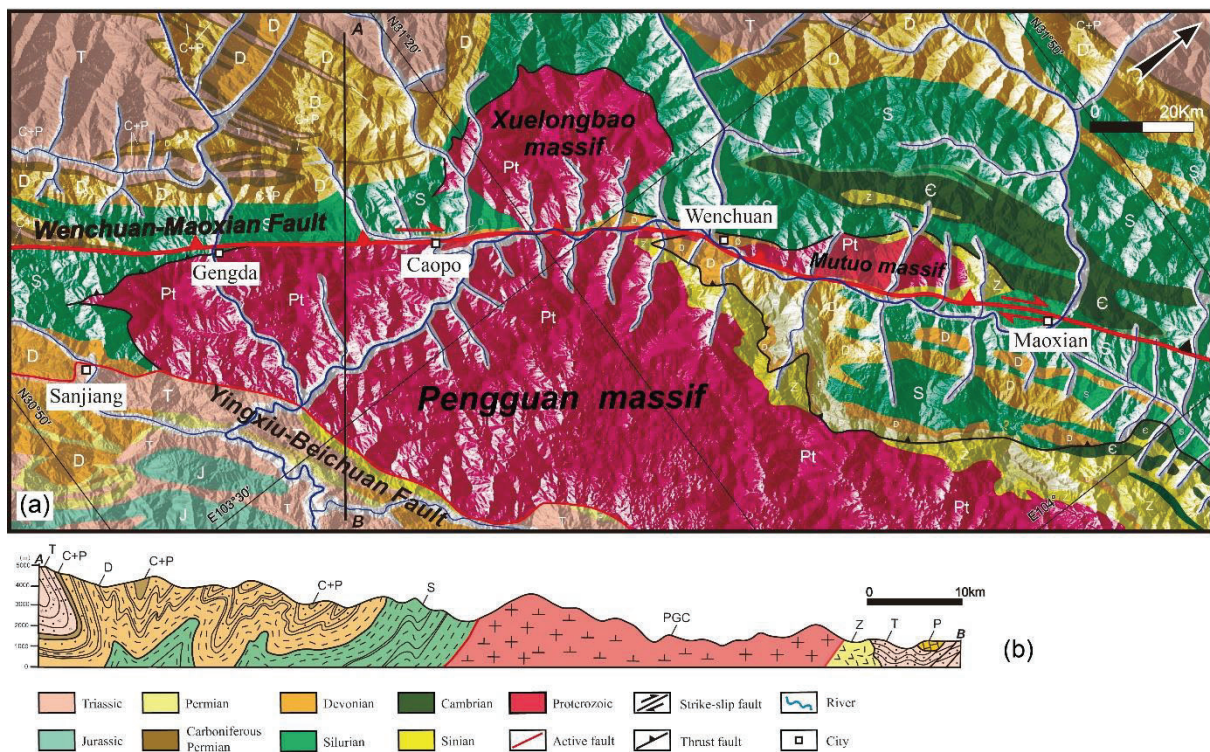


Fig2 (a) Geological map of Wenchuan-Maoxian fault; (b) Cross-section of fault

the Yingxiu-Beichuan and Anxian-Guanxian faults are characterized by obvious brittle faulting (Li et al., 2014, 2016; Wang et al., 2014; Zheng et al., 2014, 2016; He et al., 2018; Ran et al., 2019), which is thought to be the main cause of the uplift of LMS (Wang et al., 2012; Zheng et al., 2016; Wang et al., 2019). Especially, During the Wenchuan Mw7.9 earthquake in 2008, the Yingxiu-Beichuan and Anxian-Guanxian faults were strongly activated, creating a surface rupture of around 275 km (Li et al., 2008a, 2008b; Fu et al., 2011). The Wenchuan-Maoxian fault, in contrast, showed no co-seismic motion (Wang et al., 2017), and has therefore not received much attention from the academic community. Nevertheless, it is the only fault in the LMS where deep ductile deformation has been reported (Dirks et al., 1994; Burchfiel et al., 1995; Worley and Wilson, 1996; Xu et al., 2008; Xue et al., 2021). Thermochronological data show that since the initial uplift of the LMS at ~30 Ma, the upper wall of the Wenchuan-Maoxian fault (Xuelongbao Massif) has been uplifted by ~16 km, with a differential uplift of 5-7 km relative to the footwall (Pengguan Massif) (Arne et al., 1997; Godard et al., 2009; Wang et al., 2012; Tan et al., 2017; Shen et al., 2019; Furlong et al., 2021). This implies that the Wenchuan-Maoxian fault may have recorded the deformation at deeper depth during the Cenozoic time and made an important contribution to the uplift of the LMS. However, the current understanding of the structural deformation of the Wenchuan-Maoxian fault, especially the deep ductile deformation kinematics and timing are still weak. In this work we combine structural deformation analysis with *in situ* and *step heating* $^{40}\text{Ar}/^{39}\text{Ar}$ dating of mica in ductile deformed rocks along the Wenchuan-Maoxian fault to constrain the ductile faulting, and thus to discuss the contribution to the LMS building.

3.2 Geological setting

The NE-SW striking LMS belt separates the Songpan-Ganzi block in the west from the Sichuan basin in the east. Within the belt are three main subparallel faults, from west to east, the Wenchuan-Maoxian, Yingxiu-Beichuan and Anxian-Guanxian fault. Geological and geophysical data indicate that these three faults dip to NW and converge in a decollement at the depth of 20-30 km (SBGMR, 1991; Hubbard and Shaw, 2009; Feng et al., 2016). As shown in Figure 1b, the Anxian-Guanxian fault is located in the foreland of the LMS and is broadly developed along the boundary between Triassic and Jurassic strata. Drilling hole rocks along this fault show that deformed fault gouge and breccia are predominantly developed within the fault zone, indicating a clear brittle reverse deformation (He et al., 2018). The Yingxiu-Beichuan fault located in the middle of the LMS belt, developing a large number of fault gouge and breccia, and there are also cataclasite and pseudotachylyte developing, which differ from the Anxian-Guanxian fault (Li et al., 2014; Wang et al., 2014, 2019; Zheng et al., 2016). Airaghi et al. (2017) have also identified a phase of brittle-ductile deformed granites within the fault zone. This suggesting that the deformation in Yingxiu-Beichuan fault may occurred at a deeper depth than Anxian-Guanxian fault. Li et al. (2008) though the Yingxiu-Beichuan fault is dominated by reverse with some dextral component by investigating the co-seismic surface rupture, which is also consistent with the observations in the drilling hole rock in Yingxiu-Beichuan fault (Wang et al., 2014, 2019). Whereas the Wenchuan-Maoxian fault, located in the hinterland of LMS, not only exposes brittle deformation, but also develops a large number of ductile deformed rocks. The NE-SW striking Wenchuan-Maoxian fault, also dip to NW, is approximately 120 km long and separates the Proterozoic crystalline basement on the Southeast from the Paleozoic meta-sedimentary on the Northwest. Meanwhile, the Wenchuan-Maoxian fault is a clear metamorphic phase boundary: petrological evidence suggests that the strata on the south of fault experienced low-grade green schist phase metamorphism at temperature not exceeding 360 °C (Airaghi et al., 2018), whereas the Paleozoic meta-sedimentary on the northwest side experienced amphibolite phase metamorphism at temperature significantly exceeding 500 °C (Dirks et al. 1994; Airaghi et al., 2018). These phenomena suggest that the Wenchuan-Maoxian fault may have experienced multiple tectonic events since the Paleozoic (Burchfiel et al., 1995). Within the Wenchuan-Maoxian fault zone, its brittle deformation consists mainly of fault planes, fault gouge and fault breccia (Dirks et al., 1994; Burchfiel et al., 1995; Wang et al., 2014; Airaghi, 2017). Latest research on the brittle faulting shows that Wenchuan-Maoxian fault underwent a major dextral movement with little thrust since ~7 Ma. Ductile deformed rocks with steep lineation are found both in the Proterozoic basement east of the brittle fault and in metamorphosed Paleozoic sediments in the west (Burchfiel et al., 1995, Airaghi et al, 2019; Xue et al., 2021). S/C criteria generally indicate top to the SE (reverse) motion, but top to NW (normal) is also observed southeast of the WM fault (Xu et al., 2008; Burchfiel et al., 1995; Xue et al., 2021). West of the Wenchuan-Maoxian fault, the metamorphism shows a prograde path coeval with thickening at ~200 Ma (Airaghi et al., 2019). Peak metamorphism took place at ~180 Ma and retrograde evolution lasted until ~140 Ma, prior to activation of the Wenchuan fault zone sometime after 100 Ma (Airaghi et al., 2018, 2019). East of the WM fault, white micas in mylonite showing top to the west (normal) shear criteria yield an $^{40}\text{Ar}/^{39}\text{Ar}$ weighted mean age of 26.2 ± 1.0 Ma, while other samples showing similar deformation have disturbed age spectra with apparent ages between 50 and 140 Ma, interpreted to reflect episodic normal faulting from Lower Cretaceous to Miocene (Xue et al., 2021). Shen

et al. (2019) used thermochronological data to estimate that the Wenchuan-Maoxian fault is reverse at ~ 0.6 mm/yr since 12-15 Ma. Furlong et al., (2021) infer a more complicated history with the WMF being a thrust between ~ 20 and ~ 15 Ma, then stopping before resuming at 10-6 Ma with a vertical rate >0.6 mm/yr.

As for the uplift of the LMS, two controversial end-member models have been proposed. The first is Cenozoic upper crustal shortening model, which suggest that the LMS were formed by a series of thrusting. The other one is the lower crustal channel flow model. The model was proposed mainly on the basis of the very low GPS horizontal shortening rate in the LMS on short time scales (Zhang et al., 2004) and the lack of significant Cenozoic foreland basin deposit on long time scales (Burchfiel et al., 1995), as well as some geophysical data for the presence of low-velocity layers in the lower crust of the Tibetan Plateau (Nelson et al., 1996). Therefore, some scholars suggest that these “soft” lower crustal flows may have climbed to the eastern margin of the Tibetan Plateau during the Pleistocene and participated in the uplift of the LMS (Royden et al., 2008). However, it is worth noting that during the 2008 Mw 7.9 Wenchuan earthquake, the Yingxiu-Beichuan fault and the Anxian-Guanxian fault were activated respectively, showing both reverse and dextral deformation (Li et al., 2008; Fu et al., 2011), suggesting that thrusting is still the main deformation mechanism of the LMS uplift (Li et al., 2013; Wang et al., 2013; Wang et al., 2019; Li et al., 2018, 2021).

3.3 Ductile deformation of Wenchuan-Maoxian fault

To the Northwest of the Wenchuan-Maoxian fault there is a large-scale Paleozoic meta-sedimentary developed, dominated by Silurian and Devonian phyllite and crystalline limestone. To the south, the Proterozoic granitic crystalline basement is present. Based on our geological investigation at the Gengda area, where the most significant ductile deformation is

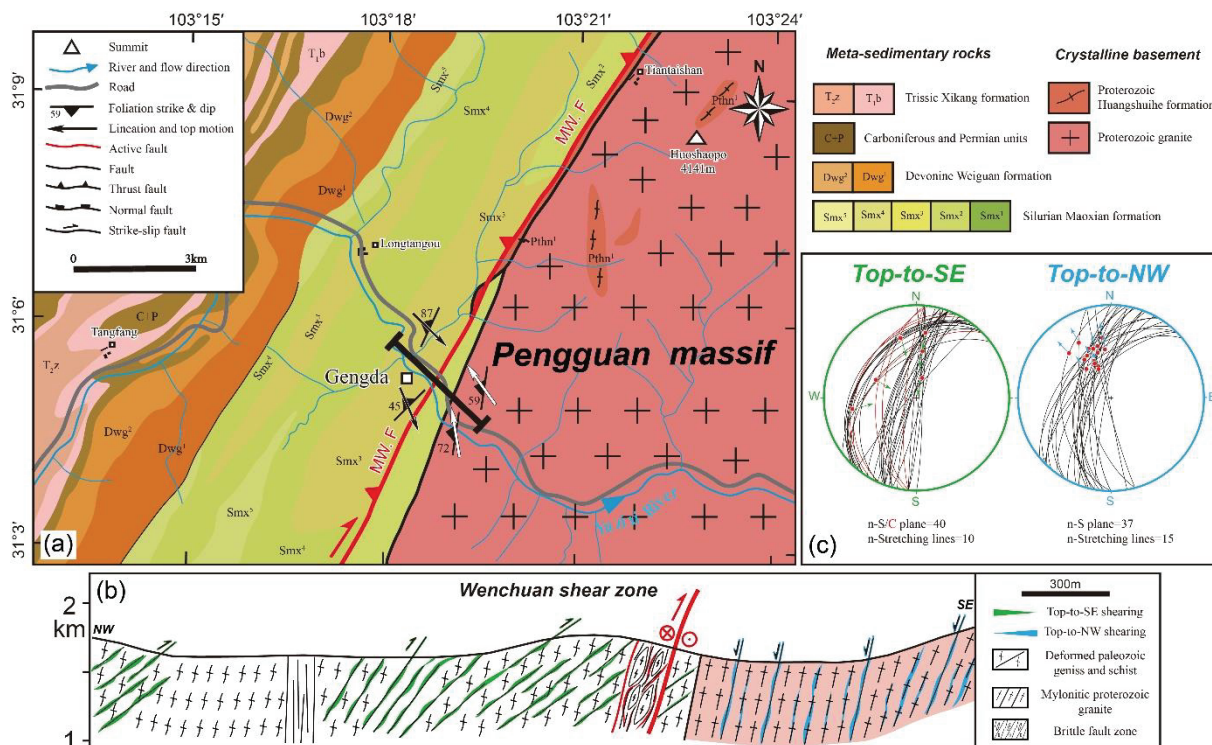


Fig3 (a) Regional geological map of Gengda site; (b) Geological cross-section; (c) Stereonet plot

exposed in Wenchuan-Maoxian fault, we found that the rocks near the fault zone differ significantly from the surrounding rocks in terms of deformation intensity, metamorphic phase and material composition. Based on this, a ductile shear zone of ~3 km wide was identified within the fault and named the Wenchuan shear zone. Meanwhile, in order to explore the distribution of Top-to-NW (normal) shearing, we also carried out a comparative study at locations that do not coincide with the fracture zone, such as the south-western end and northern section of the Pengguan Massif.

3.3.1 The Wenchuan shear zone

The shear zone is dominated by two geological units, the Silurian meta-sedimentary and the Proterozoic granitic (Pengguan Massif), which are divided by brittle Wenchuan-Maoxian fault. As a whole, the rock types within the shear zone are different, but all have suffered strong ductile deformation and developed a series of NW-dipping penetrating foliations, striking North-East (N150°-164°), dip angle 40°~85°. Stretching lineations of mica and other minerals are commonly developed on the foliations, and results of the equatorial projection show that they have a relatively uniform direction of movement, which plunge to NWW in Pengguan Massif, and to NWW in meta-sedimentary. It is noteworthy that two kinds of deformations with different kinematic sense develop within the shear zone, with the top-to-E (reverse) deformation developing only within the Paleozoic meta-sedimentary and the top-to-NW (normal) shearing developing within the Pengguan Massif. The two types of deformation do not show a clear cross-cutting relationship in the outcrop.

Meta-sedimentary

The meta-sedimentary involved in the shear zone is the Silurian Maoxian formation with a width of ~2 km, consisting mainly of strongly deformed gneisses and mica schist with an overall greenschist metamorphism phase. The rock in shear zone have a uniform NE-SE striking penetrating foliations (N30°-60°) and lineations due to strong ductile deformation. Numerous WSW-ENE mineral stretching lineations develop on the foliations, usually composed of muscovite, chlorite and recrystallized quartz. The foliations within the belt dip steeply (40°-88°) to the North-west on the whole and is slower in local areas, e.g. the mica schist near point MW19-37 has a dip of 40°-60°. In general, the equatorial projection of the 40 foliation measurements are relatively uniform, showing a dominant group of foliations, which are also cut by slower NW-dipping shear planes (35°-54°). This S/C relationship of steeply dipping foliations and slower dipping shear planes indicates eastward reverse

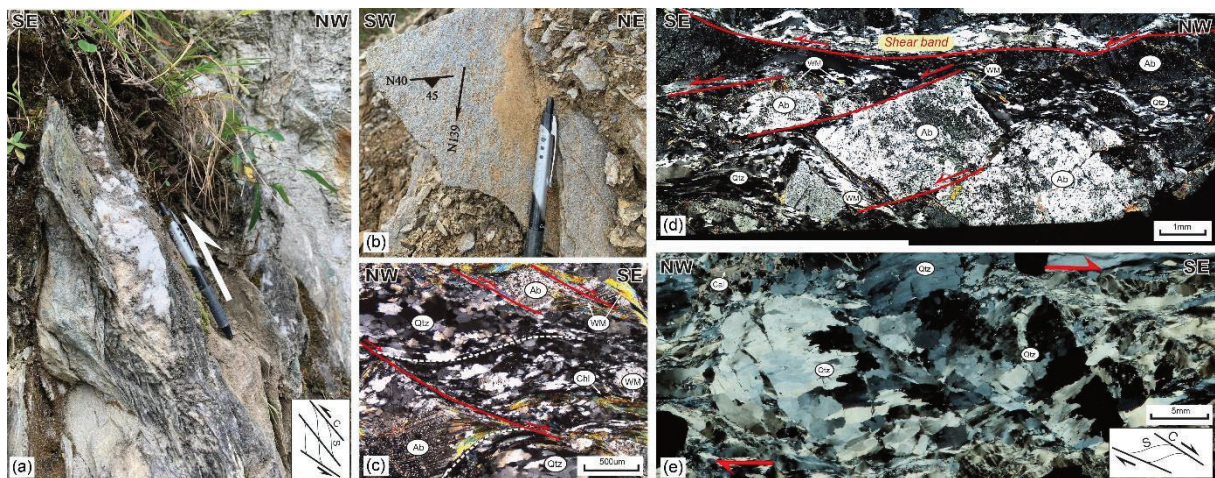


Fig4 Field observation and microstructures of reverse deformation

deformation. Detailed field observations also show that the strata within the shear zone exhibits top-to-E reverse deformation on the north-western (upper wall) side, such as the S/C fabric and quartz asymmetric trailing developing in the strongly deformed gneisses and schist. On the microscopic scale, oriented recrystallized quartz, muscovite and brittle staggered feldspar fragments (Fig. 5f) can also be observed, all of which suggest that this phase of deformation was a top-to-east reverse deformation. However, away from the shear zone, the deformation intensity in the Paleozoic meta-sedimentary strata begins to diminish and no clear kinematic signatures are observed in the outcrop, and the foliations are gradually dispersed and are superimposed by multiple phases of foliations.

Pengguan Massif

The mylonitic granites are mainly developed on the north-western boundary of the Pengguan Massif and strike NNE with an overall width of ~1 km, and the mylonitic foliations weaken and disappear as they move away from the fault. The NE-SW striking foliations dip to NW (45°-88°), where steeply dipping foliations mainly developed close to the fault core zone and disappearing at MW19-41 away from the core zone. NNW plunging mineral stretching lineations developed on the foliations, composed mainly of muscovite, chlorite and recrystallized quartz, indicating metamorphism of the greenschist phase. As a whole the equatorial projection results of the 42 foliation and stretching lineation measurements are very uniform and show a uniform movement of the upper wall in the NW direction. It is worth noting that the kinematics of this phase of deformation is not clear at the outcrop scale, and no typical and obvious shear signatures are observed. On the microscopic scale, we can clearly

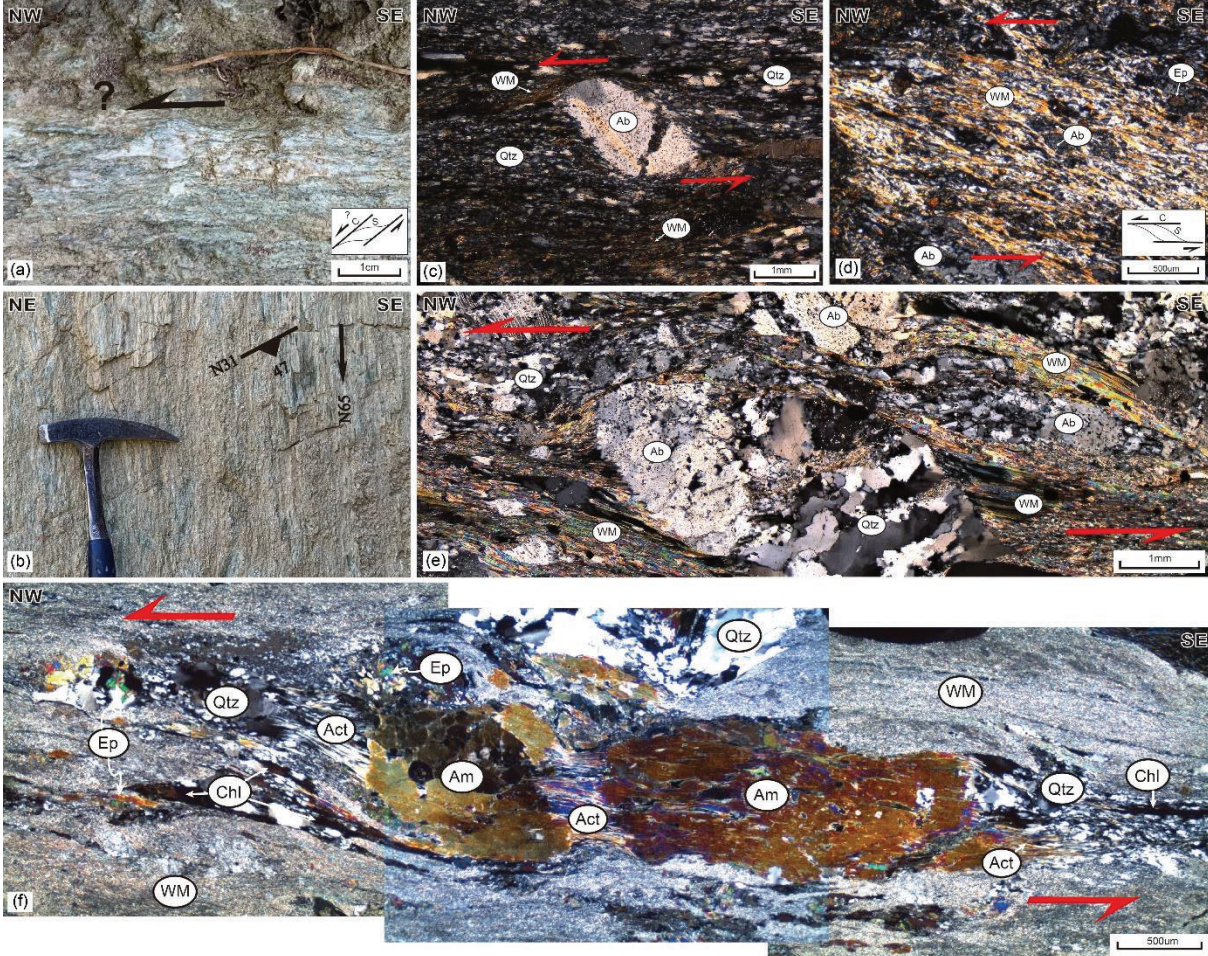


Fig5 Field observation and microstructures of normal deformation

see shear bands consisting of oriented recrystallized quartz and mica, as well as asymmetric clast of feldspar and amphibole, which also show a little bit ductile deformation. These shear criteria collectively indicate a top-to-NW shearing, while the NNW-plunging stretching lineation also show a significant right-lateral strike slip component.

3.3.2 Southwest and North of Pengguan Massif

Location and stratigraphy

The study area at the southwestern end of the Pengguan Massif is located on the northern side of Sanjiang town, where the Wenchuan-Maoxian fault passes to the west from the north and has no direct spatial contact with the Pengguan Massif. The geological units exposed in the study area are mainly Paleozoic meta-sedimentary and Proterozoic granitic basement, with some outcrops of Triassic Xikang formation. The meta-sedimentary are approximately divided into two parts, bounded by the Wenchuan-Maoxian fault. The Triassic, Carbonic, Permian and Devonian strata are mainly developed on the north-western side of the fault. On the south-east side, the Silurian Maoxian formation is mainly developed, where the Pengguan granitic massif are developed through fault contacts. The Silurian stratigraphy is dominated by mica-quartz schist, clearly distinguished from the granitic crystallized basement. North-west dipping foliations are developed within the Silurian stratigraphy, with steeply dipping foliations, and gently dipping shear zones close to the Pengguan Massif. The slowly dipping shear planes are also developed close to the Pengguan Massif. Similarly, north-west dipping foliations have also been observed within the granitic crystallized basement. However, fault gouge and fault breccias associated with brittle faulting have not been observed in the field.

The study area of the North Pengguan Massif is located to the south of Wenchuan County and east of Banqiao Village. The Wenchuan-Maoxian fault similarly passes to the north-east of the study area. The study site on the northern boundary of the Pengguan Massif has no direct contact with the Wenchuan-Maoxian fault. The geological units exposed in the study area are also Paleozoic meta-sedimentary and Proterozoic crystallized basement, some Sinian strata and Proterozoic Huangshuihe formation are also exposed in this area. The Paleozoic meta-sedimentary are similar to those at the southwestern end of Pengguan Massif, being the Carbonic and Permian strata, the Devonian Yuelizhai formation and the Silurian Maoxian formation. Within these, the Silurian strata are mainly developed on the north-west side of the Wenchuan-Maoxian fault, and only partially on the south-east side. The

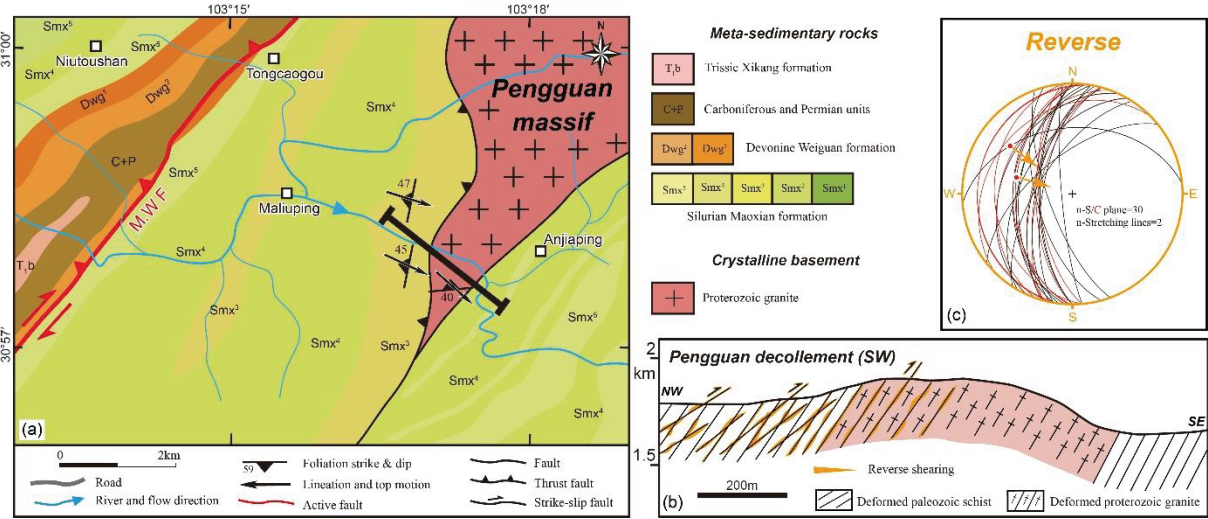


Fig6 (a) Regional geological map at the southwest tip of Pengguan massif; (b) Geological cross-section; (c) Stereonet plot

Proterozoic Huangshuihe formation and the adjacent Sinian strata are developed in long parallel fault in the north-western part of the fault zone, showing strong tectonic correlation. In contrast, the Sinian strata in the south-eastern part of the fault are in unconformable contact with the granitic Pengguan Massif and faulted to contact the Silurian Maoxian formation. The Sinian stratigraphy is dominated by schist and carbonate rocks, with a large number of steeply NW-dipping foliations and slowly dipping shear planes. No brittle deformation was also observed at this site.

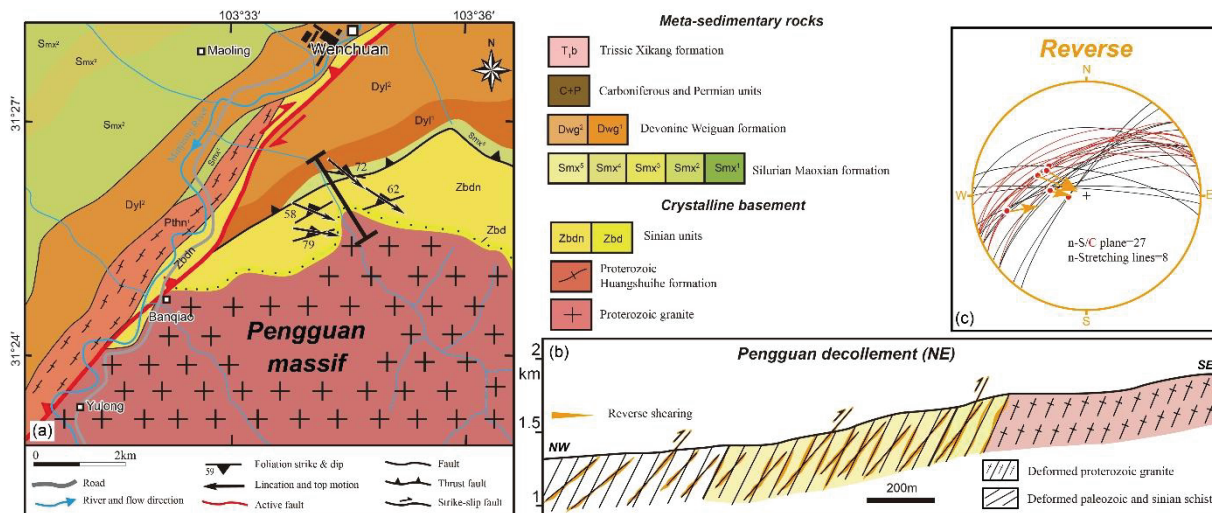


Fig7 (a) Regional geological map at the north tip of Pengguan massif; (b) Geological cross-section; (c) Stereonet plot

Field and micro structural observations

The stratigraphy involved in the ductile deformation at the southwestern end of the Pengguan Massif are mainly the Silurian Maoxian formation, which composed of strongly deformed mica schist. This set of rocks has a relatively uniform north-west dipping foliations due to the strong ductile deformation that suffered. The strike are approximately 350° to 45° , with a steeper dip (50° to 88°). Overall, the results of the equatorial projection of the 30 foliation measurements are relatively uniform, showing a dominant direction. It is also cut by slowly NW-dipping shear planes (20° to 65°) (Fig. 4.9c), and a large number of WSW-ENE oriented stretching lineations develop on the shear planes, which mainly consist of white mica, chlorite and quartz. On the field outcrop, the steeply dipping foliation and slowly dipping shear plane form a distinct and typical S/C fabric, indicating top-to-E reverse shearing. On the microscopic scale, micro shear planes which mainly consist of muscovite, recrystallized quartz and chlorite are also observed (Fig. 4.9e), forming a microscopic S/C fabric with asymmetric quartz subgrain aggregation, also suggest a reverse deformation.

At the northern end of the Pengguan Massif, the rocks involved in the ductile deformation are Sinian stratigraphy, which mainly consist of strongly deformed mica schist and limestone (Fig. 4.9a, b). It is clearly observed in the geomorphology that the Sinian strata thrust over the Pengguan Massif. Within the Sinian strata, a large number of penetrating NW-dipping foliation (striking $N65^{\circ}$ to 85°), with steeply plunging stretching lineation on it (Figure 4.8c). Overall, the results of the equatorial projection of the 27 foliations and 8 stretching lineations measurements are relatively homogeneous, showing a dominant direction, with only one lineation extracts. In areas of strong deformation, the steeply dipping foliations bend and form a typical S/C fabric with the slowly dipping shear planes (Fig. 4.9b), indicating top-to-E deformation. At the microscopic scale the distinct micro shear bands can

also be observed (Fig. 4.9f, g), which mainly consist of fine-grained white mica aggregates, recrystallized quartz grains and a small amount of chlorite. Asymmetrical clast of quartz and albite can be observed between the shear bands (Fig. 4.9f), and some calcite grains can be identified between these clast (Fig. 4.9g). All of these microstructures indicate that this phase of deformation is top-to-E reverse.



Fig8 Field observation and microstructures of Southwest and North of Pengguan Massif

3.4 Sampling and analytical strategy

Electron backscattered diffraction (EBSD) and Automatic fabric analyzer (AFA) methods have been used to observe the Crystallographic Preferred Orientation (CPO) of quartz under the deformation. The AFA technique allows for a more rapid scan and counting of the crystal preference of minerals over the whole range of the thin section (or a larger area), allowing a more visual observation and analysis of the grain boundaries and crystal preferences over a larger area than EBSD. However, it has the disadvantage that only the C-axis of the crystals can be counted and therefore needs to be combined with the EBSD technique. The test samples were not only collected from the Wenchuan shear zone, but also on the Southwest and North boundary of Pengguan Massif. All the samples are pure quartz veins which parallel with the foliation. Detailed locations information for samples are listed in Table*, the test procedure is provided in supplementary.

High resolution geochemical composition analysis and *in situ* $^{40}\text{Ar}/^{39}\text{Ar}$ geochronology (Petro-Geochronology) provide a better exploration of the relationship between age and composition and micro structure, and has been used to precisely constrain the timing of deformation. In this study, we also used the *step heating* $^{40}\text{Ar}/^{39}\text{Ar}$ dating method for comparison. The dated samples were also collected from the Wenchuan shear zone and Pengguan Massif edges, where the outcrops are fresh and deformation criteria are obvious. All the samples are the schist, mylonite and deformed gneiss. Detailed locations information for samples are listed in Table*.

White mica in our samples are elongated and aligned along the shear bands and trails, and has been used as the target mineral for dating. One dated sample was split into two parts, one part was ground and polished into the rock chip with the thickness of 1 mm along the XZ

(shear) plane for subsequent in situ analysis. The other was crushed to selected pure white mica grains for *step heating* $^{40}\text{Ar}/^{39}\text{Ar}$ dating.

The geochemical composition test was carried out by Electron microprobe analyses (EMPA), and quantified and visualized by the XMapTools software.

Analytical methods and results for EMPA and $^{40}\text{Ar}/^{39}\text{Ar}$ analyses are detailed in supplementary, respectively.

3.5 Results and interpretation

3.5.1 Quartz crystallographic preferred orientation

Three samples of MW19-37, MW19-32 and MW19-36 were collected from the Paleozoic meta-sedimentary in Wenchuan shear zone and MW19-17 was from the Proterozoic massif. Sample MW19-1 and MW19-51 were collected from the Southwest and North boundary of Pengguan Massif, respectively.

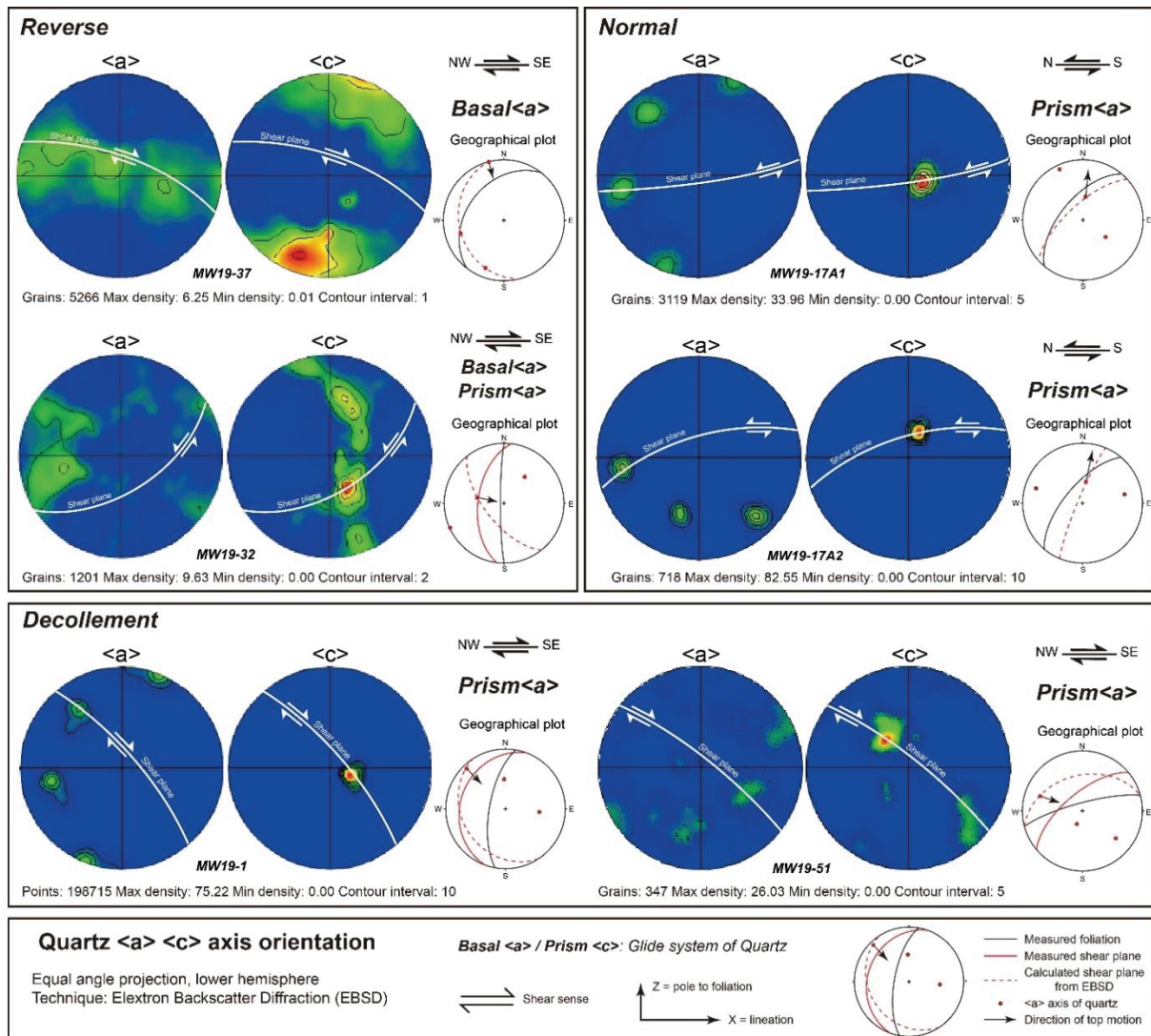


Fig9 EBSD results

Electron backscattered diffraction

The preferred orientation of quartz from samples MW19-37 shows that the C-axis of quartz is extremely dense near the X-axis, suggesting that basal<a> slip is the dominant slip system. The quartz preferred orientation of samples MW19-32 is slightly more complex, with the quartz C-axis being concentrated near the X-axis and partially near the Y-axis, but the overall shape shows type I, suggesting that basal<a> slip should be the dominant slip system in this sample and that the rock deformation is relatively weak (Passchier and Trouw, 2005). Both samples also show an asymmetry shape in the CPO of the C-axis, which indicate top-to-E reverse deformation by combined with the orientation of the thin section, and the deformation condition are dominated by low temperature (Neumann, 2000). The C-axis extreme density of sample MW19-36 is also located near the X-axis, but it is symmetrically distributed throughout. This suggests that the sample may not have undergone strong simple shearing and that the deformation is dominated by pure shear and that the deformation conditions are low temperature (Neumann, 2000). MW19-17A1 and MW19-17A2 are two tested areas in sample MW19-17, both results show similar and distinctly CPO of quartz, with the C-axis extreme densities all located near the X-axis, suggesting that prism <a> slip is the dominant slip system for quartz in this sample. Based on the distribution of their a-axes and the orientation of the thin section, they all show top-to-N normal deformation, and the deformation conditions of the rock are moderate temperature (Grujic et al., 1996; Stipp et al., 2002). The CPO of quartz in sample MW19-1 and MW19-51 are similar to that of MW19-17A1/A2, with the C-axis extreme density also located near the X-axis, again suggesting that prism<a>slip is the dominant slip system for quartz in this sample. Based on the shape of the quartz a-axis and the spatial orientation of the two thin sections, they both also show top-to-SE reverse deformation, and the condition is probably at mid-temperature (Grujic et al., 1996; Stipp et al., 2002).

Automatic fabric analyzer

The spatial orientation of the quartz <c> axis within the full thin section region of the six samples was measured and mapped using automated fabric analysis (AFA) techniques. As shown in Fig4.11 and 4.12, the quartz particles within the flakes are marked with different color depending on the spatial orientation of their <c>axis. Sample MW19-36, a set of paralleled micro shear bands visible under the microscope, indicating a dextral shearing and top-to-E deformation base on the orientation of thin section. The quartz within the micro shear zone is arranged in subgrain aggregates and oriented with similar marker colors (red-orange), suggesting that these fine quartz grains within the zone have a similar <c>-axis spatial distribution. Meanwhile, the spatial orientation of the quartz optical axis shows that the quartz in the micro shear zone are predominantly purple and red in color, with a gradual transition to the blue and green "residual" quartz, suggesting that the dynamic recrystallization mechanism of the quartz is bulge recrystallization (stipp et al., 2002), indicating deformation under low temperature conditions. Whereas the CPO of the quartz <c> axis for the full thin section statistics exhibit the same deformation characteristics: typical basal <a>slip accompanied by asymmetric girdle shape, which indicate dextral shear under low temperature conditions; In samples MW19-32, the quartz is observed under the optical microscope as a subgrain aggregate mostly banded along the x-axis, with a relatively homogeneous color signature (red-purple red) and a gradual transition from blue-green quartz, suggesting that the recrystallisation mechanism of the quartz grains may still be bulge recrystallisation (Stipp et al., 2002), indicating deformation at low temperatures. The CPO of its quartz <c> axis also shows basal <a>slip under low temperature conditions, with weakly

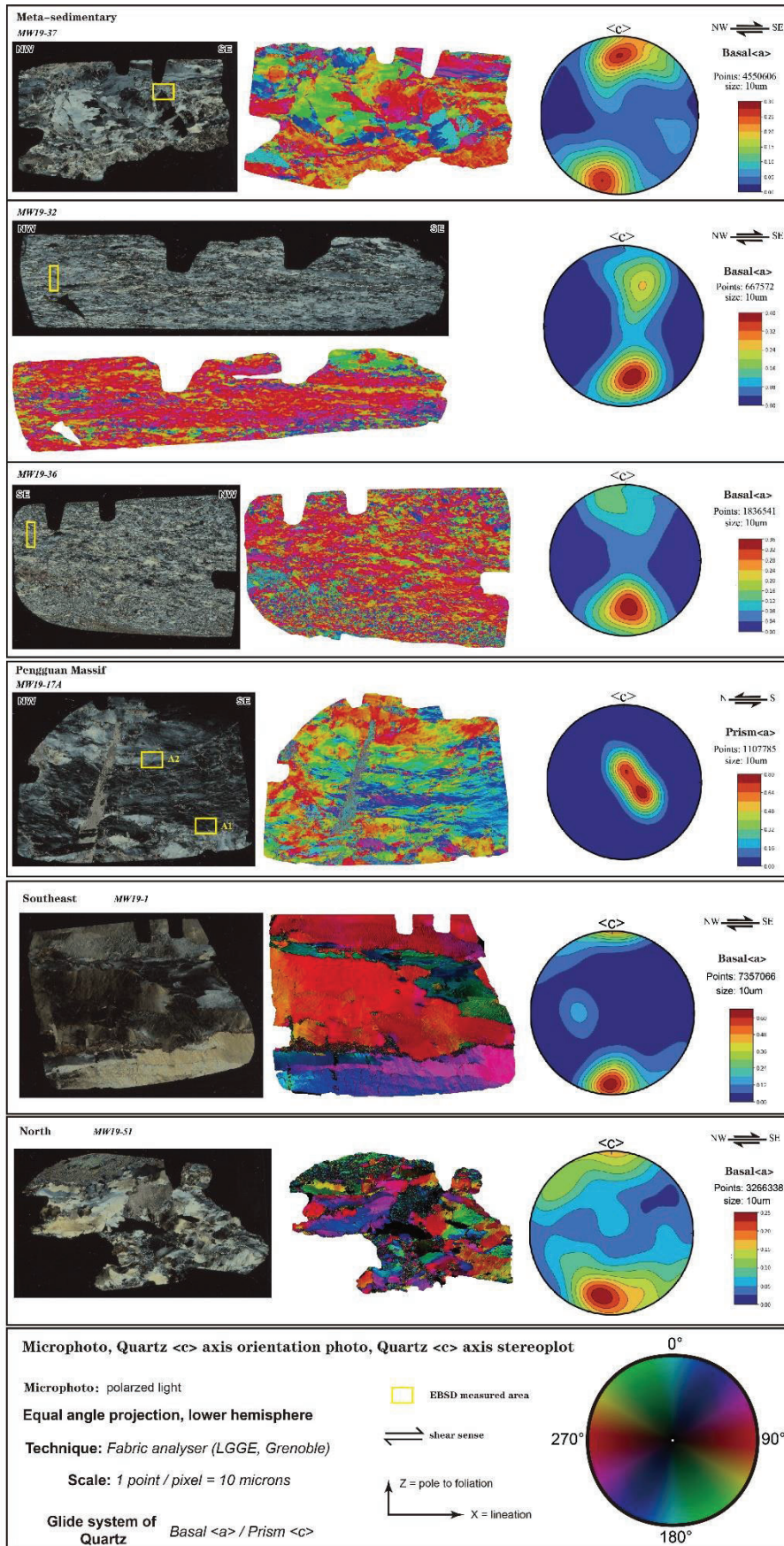


Fig10 AFA results

asymmetric girdle shape indicating a dextral shearing (top-to-SE deformation); Sample MW19-36, the quartz was oriented weakly, but it has similar optical microscopic features to MW19-32, indicating that the quartz grains deformed at low temperatures. The CPO of the quartz $\langle c \rangle$ axis also show similar characteristics: basal $\langle a \rangle$ slip, indicating deformation under low temperature conditions. But the symmetrical girdle shape indicates that simple shear deformation is not evident in this sample; Sample MW19-17A shows a typical core and mantle structure by comparison of optical micro image and quartz $\langle c \rangle$ axis distribution image: large residual quartz grains (red-orange) and a series of quartz subgrain aggregates (blue-green) oriented between the grains, which indicate the recrystallisation mechanism of the quartz is subgrain rotation recrystallization at medium temperature. This is also consistent with the quartz $\langle c \rangle$ axis CPO: Prism $\langle a \rangle$ slip predominates, suggesting shear deformation at medium temperature conditions. By comparing the quartz $\langle a \rangle$ -axis extreme density distribution in the EBSD results for the same sample (Fig4.10), the quartz CPO for this sample also indicates left-lateral shearing; Sample MW19-1 developed large quartz grains, with some smaller quartz grains and sub-grain aggregates developing between them. These large grains with similar spatial distribution of $\langle c \rangle$ axes inside, showing a uniform color (red). The color of the intergranular grains is transitional to the larger grains (red-purple-blue-green), possibly reflecting the homological relationship of them, which suggest a dynamic recrystallisation mechanism of quartz as bulge recrystallisation (Stipp et al., 2002). This phenomenon is also verified by the CPO of the quartz $\langle c \rangle$ axis in full thin section: the typical basal $\langle a \rangle$ slip accompanied by a certain asymmetrical girdle shape, indicating right-lateral shearing at low temperatures; The quartz in samples MW19-51 are arranged in subgrain aggregates. In the upper left of the thin section, the curved quartz grain assemblage indicate a right-lateral shearing. The quartz grains also show a clear color gradient (red-violet-blue-green), suggesting a similar and gradual spatial distribution of the $\langle c \rangle$ axis, indicating a dynamic recrystallization mechanism of bulge recrystallization (Stipp et al., 2002). Full thin section statistics of quartz $\langle c \rangle$ axis CPO show deformation as basal $\langle a \rangle$ slip with asymmetric girdle shape, which indicate right-lateral shearing in the low temperature domain. Based on the spatial orientation of the MW19-1 and MW19-51 thin sections, the quartz $\langle c \rangle$ axis CPO for both samples similarly indicate a top-to-SE reverse deformation.

3.5.2 Petro-Geochronology in white mica

The Wenchuan shear zone

As showed in Ge et al. (2023), micaschist sample MW19-38A, collected in Paleozoic metamorphic rocks with clear reverse deformation, has two generations of white mica by using quantitative composition mapping: the yellow-blue part with low Xcel (percentage of Celadonite, <0.2) and the red part with high Xcel (>0.2). *In situ* $^{40}\text{Ar}/^{39}\text{Ar}$ dating yield most of ages ≤ 20 Ma in the white mica with low Xcel, while few of ages >300 Ma in the white mica with high Xcel. Among these younger ages, 25 spots define an average age of 15.7 ± 0.36 Ma (MSWD=1.46). Both *step heating* $^{40}\text{Ar}/^{39}\text{Ar}$ dating runs yield relatively flat spectra with a large fraction of the ages consistent with the younger in situ ages at ~ 15 Ma, where the results showed a ^{40}Ar loss-like spectrum between 10 and 23 Ma from 2% to 18% of the total ^{39}Ar released, then followed by a nearly flat segment at ~ 15 Ma until 90% of the total ^{39}Ar released.

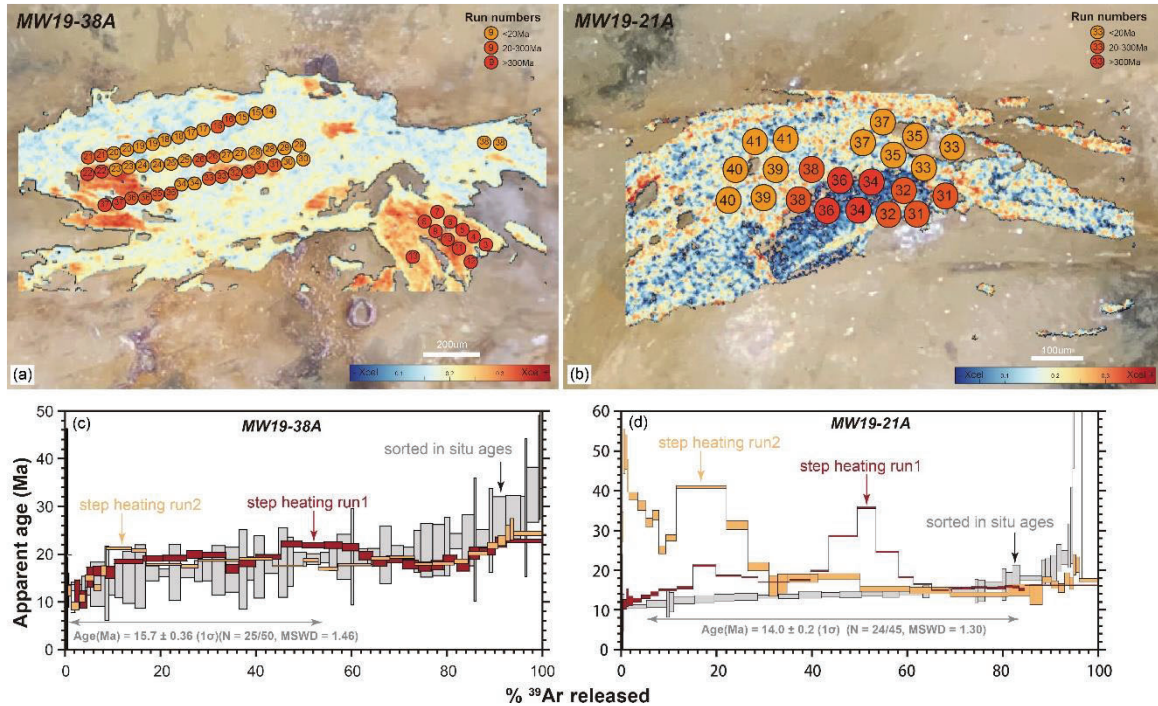


Fig11 (a) Chemical composition of white mica in MW19-38A and laser in situ $^{40}\text{Ar}/^{39}\text{Ar}$ age distribution; (b) in situ and step heating $^{40}\text{Ar}/^{39}\text{Ar}$ ages of MW19-38A; (c) Chemical composition of white mica in MW19-21A and laser in situ $^{40}\text{Ar}/^{39}\text{Ar}$ age distribution; (d) in situ and step heating $^{40}\text{Ar}/^{39}\text{Ar}$ ages of MW19-21A;

Micaschist sample MW19-21A is also collected in Paleozoic metamorphic rocks, which is 200 m west far away from MW19-38A. Quantitative composition map of white mica also shows two generations depend to Xcel: the blue part with low Xcel (<0.2) and the red part with high Xcel (>0.2). whereas *In situ* $^{40}\text{Ar}/^{39}\text{Ar}$ dating yield most of ages ≤ 20 Ma in the white mica with high Xcel, few of ages >300 Ma in the white mica with low Xcel. At the part of younger ages, 24 spots define an average age of 14.0 ± 0.2 Ma (MSWD=1.30). The companion *step heating* $^{40}\text{Ar}/^{39}\text{Ar}$ dating has two runs, which yield an upward convex spectrum and followed a relatively flat spectra with most of ages consistent with in situ ages at the younger part of ~ 14 Ma.

Micaschist sample MW19-10B is collected from the Proterozoic Pengguan Massif with top-to-W shearing. As Ge et al. (2023) showed, chemical composition in white mica vary moderately in Xcel content (0.2-0.4). *In situ* $^{40}\text{Ar}/^{39}\text{Ar}$ apparent ages distributed between 30 and 140 Ma. The companion *step heating* results yields a flat segment at 28.0 ± 0.9 Ma from 4% to 48% of the total ^{39}Ar released, which is consistent with the youngest component of the in situ ages. The spectrum of step heating then followed by an overall complex shape, where age climb up to ~ 450 Ma, indicating an inherited high-temperature component.

Micaschist sample MW19-15C is collected 400m east away of sample MW19-15C, also located in Pengguan Massif. Quantitative composition mapping in white mica shows moderate variation in Xcel between 0.2 and 0.6, and the Xcel value progressively increase from left to right. The 104 spots *in situ* $^{40}\text{Ar}/^{39}\text{Ar}$ apparent ages range from ~ 61 to ~ 130 Ma, and become progressively older with increasing Xcel content (from left to right).

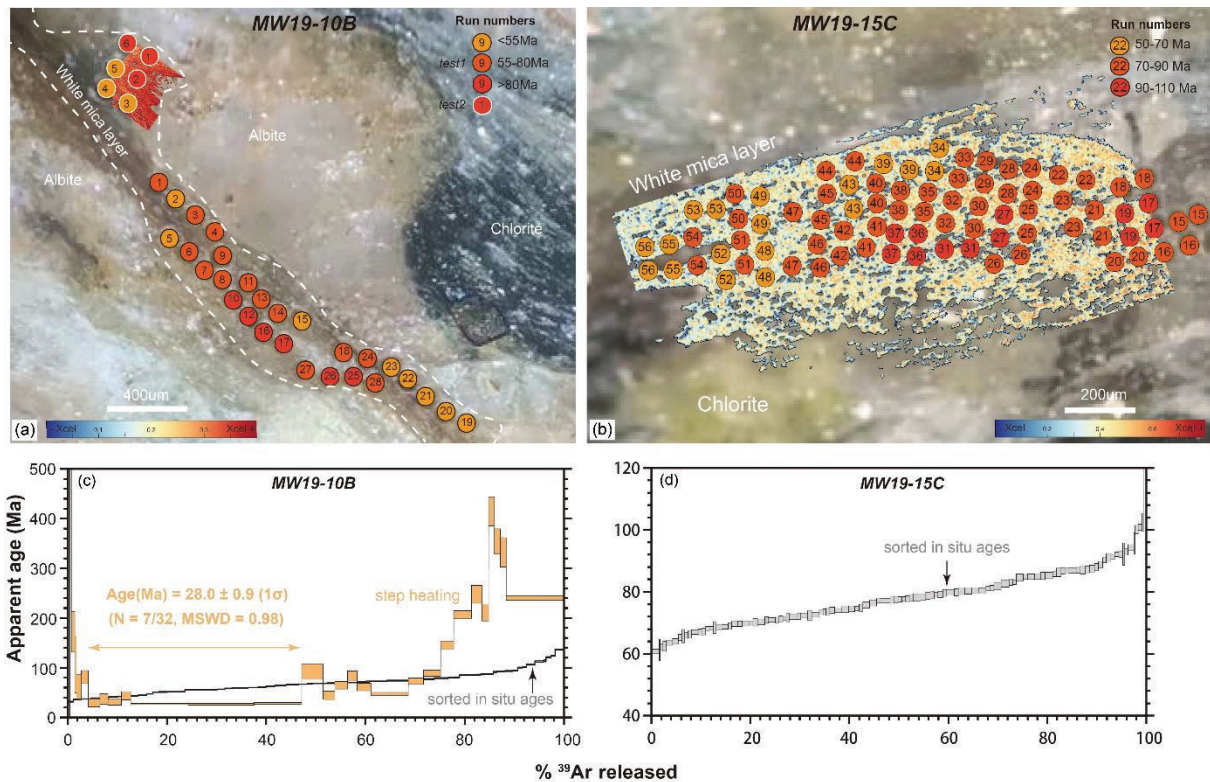


Fig12 (a) Chemical composition of white mica in MW19-10B and laser in situ $^{40}\text{Ar}/^{39}\text{Ar}$ age distribution; (b) in situ and step heating $^{40}\text{Ar}/^{39}\text{Ar}$ ages of MW19-10B; (c) Chemical composition of white mica in MW19-15C and laser in situ $^{40}\text{Ar}/^{39}\text{Ar}$ age distribution; (b) in situ and step heating $^{40}\text{Ar}/^{39}\text{Ar}$ ages of MW19-15C;

Southwest and North of Pengguan Massif

Micaschist sample MW19-15C is collected from the quartz vein in Silurian metamorphic rocks, which is located at the Southwest tip of Pengguan Massif. Quantitative composition map of white mica shows homogeneous Xcel value distribution (< 0.15). The *in situ* $^{40}\text{Ar}/^{39}\text{Ar}$ dating also show consistent apparent ages of 51.3 ± 1.4 Ma (MSWD=1.46). Two companion step heating runs also yield a relatively flat spectrum at ~ 50 Ma, which consistent with the *in situ* apparent ages. After that, the step-spectrum followed by an upward convex shape, which may result from the excess Ar.

Micaschist sample MW19-54A is collected from the Sinian metamorphic rocks, which locates at the North edge of Pengguan Massif and shows clear kinematic indicates of reverse deformation. Quantitative composition mapping in white mica shows homogeneous Xcel value at 0.4, indicating there is only one generation of white mica. *In situ* $^{40}\text{Ar}/^{39}\text{Ar}$ dating also yields relatively consistent apparent age at 149.4 ± 0.3 Ma. The *step heating* $^{40}\text{Ar}/^{39}\text{Ar}$ dating run2 yielded a ^{40}Ar loss-like spectrum starting at ~ 50 Ma and stabilizing between 135 and 150 Ma from 20% to 95% of the total ^{39}Ar released, followed by an increasing age to ~ 155 Ma. The run1 has an overall complex spectrum, where yield two very young ages in the middle that may result from the Ar loss.

3.5.3 Chlorite thermometer

In order to further investigate and constrain the possible temperatures of ductile deformation in the fracture zone, we analyzed samples from the study area using chlorite

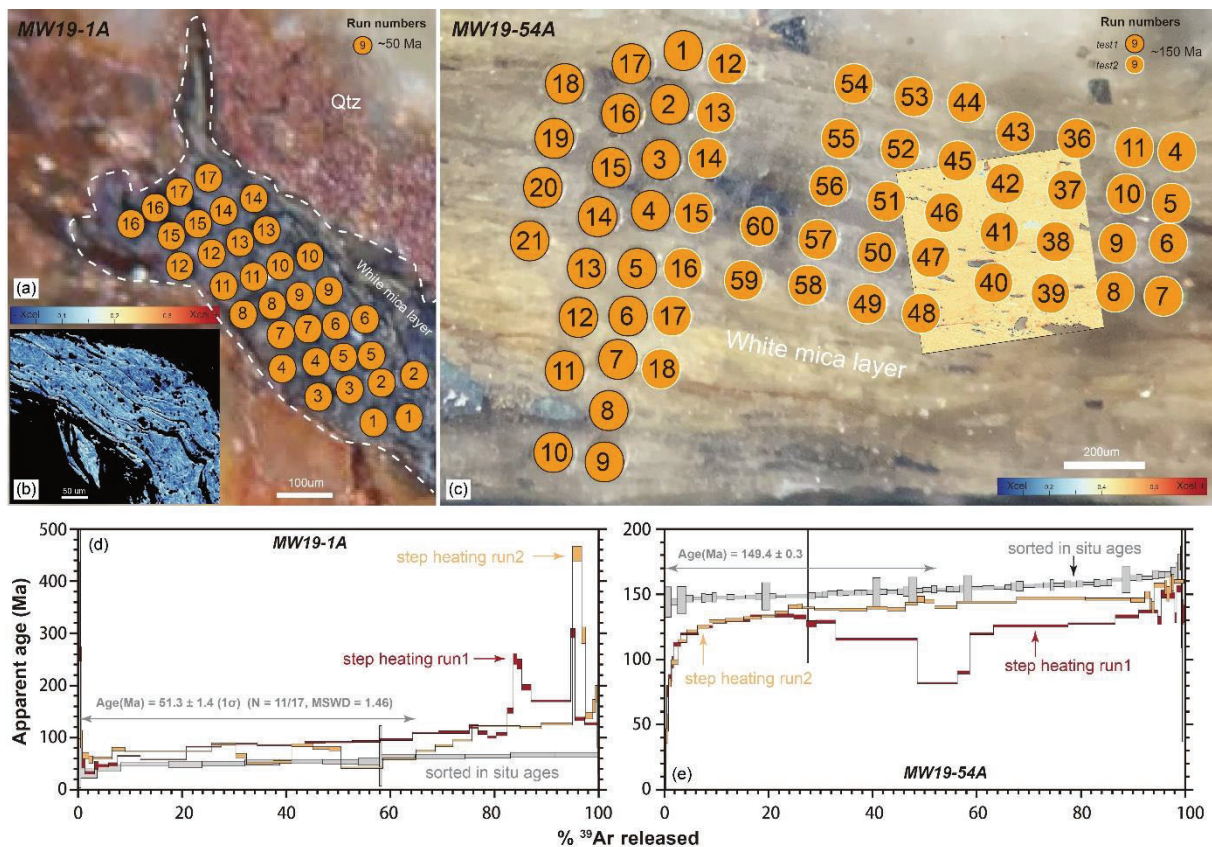


Fig13 (a) Chemical composition of white mica in MW19-1A and laser in situ $^{40}\text{Ar}/^{39}\text{Ar}$ Ar age distribution; (b) in situ and step heating $^{40}\text{Ar}/^{39}\text{Ar}$ ages of MW19-1A; (c) Chemical composition of white mica in MW19-54A and laser in situ $^{40}\text{Ar}/^{39}\text{Ar}$ age distribution; (b) in situ and step heating $^{40}\text{Ar}/^{39}\text{Ar}$ ages of MW19-54A;

thermometers (Bourdelle and Cathelineau, 2015). According to the mineral phases and microstructures of the study samples, chlorite, as a associated mineral, tends to be distributed in spatial position along with white mica and is also clearly orientated, we think that the chlorite in the study samples should have been formed at the same time with white mica recrystallization. Furthermore, chlorite is a highly desirable indicator for probing the thermo-evolutionary history of rocks, and its own wide range of compositional variations are very sensitive to its many formation conditions, such as temperature, pressure, fluid composition, and redox state, etc. (Bourdelle et al., 2013). The chlorite thermometer applied in this study is a visualization thermometer proposed by Bourdelle and Cathelineau in 2015 for temperature estimation of low-temperature deformations, which has a wide and good application for temperature estimation of low-medium temperature deformations.

The data used to estimate the temperatures were obtained from EMPA point analyses, the locations of the points and the corresponding data are shown in supplementary. As shown in Figure 5.15, the estimated chlorite composition of sample MW19-10 ranges between 315° and $>350^\circ\text{C}$, with one data point falling at 160°C and the majority of the data (37%) falling at $\sim 350^\circ\text{C}$. Sample MW19-15 gives a relatively consistent estimate of temperature at $\sim 265^\circ\text{C}$. Sample MW19-38 gives temperatures in the range of $170^\circ\sim$ and $>350^\circ\text{C}$, with most of the data (46%) centred at $\sim 350^\circ\text{C}$. Sample MW19-21 gives estimated temperatures in the range $230^\circ\sim 350^\circ\text{C}$, with most of the data (64%) concentrated at $\sim 300^\circ\text{C}$. Chlorite minerals were not observed in the study area of samples MW19-1 and MW19-54, so we suggest a possible temperature range of 300° to 400°C by the characteristics of the mineral assemblage, the mineral deformation behavior, and the CPO of the quartz.

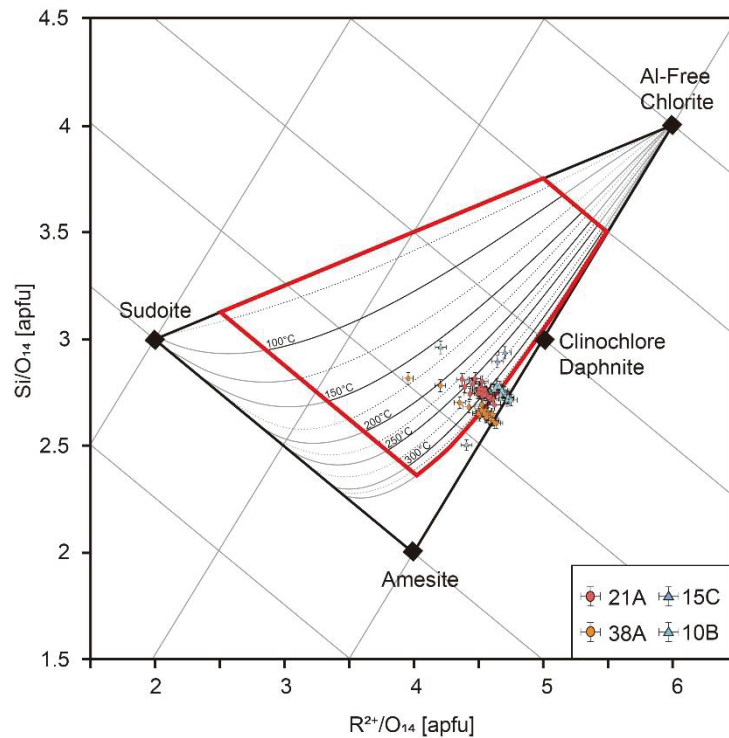


Fig14 Chlorite thermometer

3.6 Discussion

3.6.1 Kinematics and deformation condition

The Wenchuan-Maoxian fault is an important part of the Longmen Shan belt on the eastern margin of the Tibetan Plateau, and it is also the important boundary that separating the Songpan-Ganzi block and the Longmen Shan, which is characterized by obvious deep-level deformation. Since the Wenchuan-Maoxian fault remained silent during the Wenchuan earthquake, its present-day activity may be weak (Li et al., 2008a; Fu et al., 2011). Therefore, understanding its ductile deformation characteristics is highly significant for understanding the early formation process of Longmen Shan. Previous studies have attributed the extensive ductile deformation in the hinterland region of LMS to the Wenchuan-Maoxian shear zone, which was affected by the westward subduction of the Yangzi plate in the Early Mesozoic, and showed significant thrusting with left-lateral strike-slip shear (Dirk et al., 1994). Wang et al. (2014) also suggested that a phase of ductile right-lateral shear may existed at the Late Cenozoic. On the east side of the Wenchuan-Maoxian fault, immediately adjacent to the brittle fault zone, ductile top-to-NW normal shearing is also developed, which is mostly considered to be developed only on the north-west side of the Proterozoic massif (Xu et al., 2008; Tian et al., 2016; Xue et al., 2017, 2021). This time, through detailed field geological investigations and indoor tectonic analyses, we not only identified this phase of ductile normal deformation, but also identified a new phase of ductile reverse deformation.

In the process of faulting, the rocks within the zone will be modified by strong metamorphism and deformation, thus retaining a large number of different mineral assemblages, microstructures and mineral grouping and other characteristics, which provides an important basis for our understanding of the nature, the environment and the process of the deformation. Our study show that two types of shear deformation exist within the Wenchuan shear zone: top-to-E reverse deformation and top-to-NW normal deformation. Of these,

reverse deformation is developed within the meta-sedimentary unit and is characterised by brittle deformation of feldspars and lattice plastic deformation of minerals such as quartz and mica, indicating greenschist phase metamorphic conditions. The deformation of its field outcrops is obvious, with the typical S/C fabric indicating that the shear zone has undergone strong reverse deformation. The lattice structure (EBSD, AFA) of the quartz veins shows that the quartz sub-grains are oriented, and the dynamic recrystallization mechanism of the quartz is bulge recrystallization, and the deformation is dominated by the basal $\langle a \rangle$ slip system, which corresponds to the deformation temperatures of 300-400°C, indicating that the shear deformation in this period occurred in the low-temperature domain. It is noteworthy that the C-axis configuration of quartz crystals of sample MW19-32, collected at the edge of the shear zone, is characterised by Type I, showing weak deformation. On the other hand, the C-axis configuration of sample MW19-37, collected closer to the core of the shear zone, shows a typical asymmetric pattern, indicating strong and obvious shear deformation. This indicates that the deformation intensity of this phase of deformation gradually decreases as it moves away from the shear zone.

Top-to-NW normal deformation developed within the Pengguan massif also shows the deformation environment of the greenschist phase, and the characteristic deformation mineral assemblage is quartz + mica + chlorite, but the albite also has some brittle-ductile deformation characteristics, suggesting that the deformation temperature may be higher. This deformation is not obvious on the outcrop scale, and at the macroscopic scale, the Proterozoic massif develop beneath the Paleozoic unit. The lattice structure (EBSD, AFA) of quartz shows that the dynamic recrystallisation mechanism of quartz is mainly subgrain rotation recrystallization, and the deformation is dominated by prism $\langle a \rangle$ slip systems, which is indicative of shear deformation at the medium temperature that corresponding to temperatures in the range of 350-650 °C.

3.6.2 Width of shear zone

There is a consensus that rocks with ductile deformation are widely exposed in the hinterland of Longmen Shan (Burchfiel et al., 1995; Airaghi et al, 2019; Xue et al., 2021), which constitutes a clear contrast with the brittle deformation in the foreland region (Li et al., 2014; Wang et al. al., 2014; Airaghi et al, 2017; He et al., 2018). But what is the relationship between these ductile deformed rocks and the Wenchuan-Maoxian fault? Previous studies have not given a clear expression. Most people have classified the widely distributed Paleozoic strata and some Triassic strata in the hinterland area as a large ductile shear zone with a width of about 35 km (Disk et al., 1994; Worley et al., 1996; Arne et al., 1997). During this field investigation, we found that these rocks may not all belong to the Wenchuan shear zone. Therefore, we compare and discuss their spatial distribution, rock composition, deformation intensity and condition.

Firstly, as mentioned above, within the redefined Wenchuan-Maoxian shear zone there are two kinematically distinct parts, roughly bounded by the brittle Wenchuan-Maoxian rupture, which belong to different geological units (Fig. 4a). In the Paleozoic meta-sedimentary units, the rocks within the shear zones clearly have uniform foliation and shear plane striking (Fig. 3d), with steeply dipping NE-SW foliations cut by gently dipping shear planes (Fig. 4d, Fig. 5b, c). Moreover, consistent and distinct top-to-E reverse shearing is observed at both outcrop and microscopic scales (Fig. 5). The quartz CPO in the belt not only has obvious kinematic orientation, but also show the correlation with fault activity. However, in other Paleozoic units that west of the shear zone, deformation is not as strong, with obvious foliation stacking and replacement observed at both macroscopic and microscopic scales (Figs. 6b - e), and there is no shear plane development. In some areas, even early near-

horizontal primary foliations can be seen, e.g. MW19-22 (Fig. 6a). In other areas, although the development of NE-striking foliations can also be seen, its strike distribution is more dispersed, and a large number of east-dipping foliations are developed (e.g., MW19-28, Figs. 6b, c), and the dips are not uniform (Fig. 6f), which is therefore more likely to be related to regional metamorphism rather than faulting. More importantly, the shear directions in this set of stratigraphy are very inconspicuous, and no effective kinematic signatures can be identified, making it difficult to classify it as a shear zone with obvious kinematic directions. Meanwhile, in terms of material composition, the rocks in the shear zone are composed of strongly deformed gneisses and schists, which are clearly differentiated from the weakly deformed limestone and phyllite in other Paleozoic strata (Fig. 6a, b). In the other unit of the shear zone, which is the Proterozoic Pengguan massif, the rocks at the north-west boundary of massif undergoes obvious mylonitization and exhibits top-to-NW normal deformation. Although the macroscopic deformation is not clear (Fig. 7b, c), there are only recognizable kinematic indicators at the microscopic scale (Fig. 7f, g, h). However, the deformation-related permeability foliations and lineations diminish and disappear away from the shear zone (Fig. 4b, Fig. 7e), which suggests a very strong tectonic correlation.

Second, most of the Paleozoic meta-sedimentary exposed on a large scale at the hinterland of the Longmen Shan are thought to have undergone Mesozoic metamorphic events (Liu et al., 2005; Yan et al., 2008, 2011, 2018; Airaghi et al., 2018, 2019; Xue et al., 2017, 2021), and the whole has ductile reverse deformation in a south-east direction (Disk et al., 1994; Worley et al., 1996; Yan et al., 2011; Airaghi et al., 2018; Xue et al., 2017). Precise petrological studies indicate its peak metamorphic conditions of $\sim 11 \pm 2$ kbar, ~ 620 °C (Dirks et al., 1994; Airaghi et al., 2019). In contrast, the mineral deformation behavior and characteristic mineral assemblages of this reverse deformation within the shear zone indicate a metamorphic condition of greenschist phase. The quartz EBSD and AFA results also show that the deformation temperature does not exceed 400°C, which is significantly lower than that of this metamorphic event on the region. The Pengguan massif rocks are mainly composed of Neoproterozoic granitic rocks (SBGMR, 1991). The mylonite at north-western part are clearly different from the crystalline magma in its core, which should be the product of later tectonic deformation.

Therefore, considering the rock composition, foliation striking, deformation intensity and condition, we think that the newly identified low-temperature reverse deformation may be a shallow deformation related to the Wenchuan-Maoxian faulting. Similarly, the normal deformation developed in the north-west boundary of the Pengguan massif are also a product of the later faulting, which is regarded as resulting from the uplift of the Pengguan massif (Xu et al., 2009; Tian et al., 2016; Shen et al., 2019; Xue et al., 2021), which is also consistent with our field observations that the foliation in the massif gradually slows down and disappears as they move away from the fault zone (Fig. 4 b, Fig. 7e). Therefore, based on the spatial distribution and origin of these two phases of deformations, we suggest that they are both ductile deformations associated with the Wenchuan-Maoxian fault, constituting a shear zone with the width of ~ 3 km.

3.6.3 Timing

Wenchuan shear zone

Samples MW19-38, the quantitative compositional map of white mica based on Xcel content show two types of mica, M1 with a high Xcel content (>0.2) and M2 with a low Xcel content (<0.2). In Fig. 5.11b, there is a clear compositional divergence between M1 and M2. M1 displays relatively automorphic crystalline morphology and is less orientated than M2. M2, on the other hand, develops as a whole in a diffuse manner within the shear zone,

showing clear tectonic correlation. *In situ* ^{40}Ar - ^{39}Ar ages (Fig. 5.22a) also shows a clear correlation with mica composition. Semi-automorphic and high Xcel M1 has a significantly older age (>300 Ma). M2, which is diffusely close to the shear zone and has low Xcel values, is significantly younger (<20 Ma). Similarly, when a laser point contains both types of mica, the age fluctuates between 20 and 300 Ma. The *in situ* ^{40}Ar - ^{39}Ar age of this sample has a relatively large young fraction and a relatively flat age spectrum, giving a consistent age of 15.4 ± 0.19 Ma (Fig. 5.22c). In contrast, the step-heating ages produce relatively flat age spectra ranging from 10-23 Ma as the temperature increasing, with a large fraction of them consistent with a young *in situ* age of ~15 Ma. Thus based on these phenomena we suggest that the high Xcel-value M1 mica may have originated from an early event (>600 Ma), whereas the low Xcel-value M2 mica is associated with a retrograde deformation event, recording a mica growth event at ~15 Ma.

Samples MW19-21, the quantitative compositional map of white mica based on Xcel content clearly show two types of mica, M1 with low Xcel content (<0.17) and M2 with high Xcel content (>0.17). Especially in Fig 5.10b, there is no obvious compositional transition between M1 and M2 and M2 is mostly developed in the interior of the shear plane, which shows strong correlation with structural deformation. *In situ* ^{40}Ar - ^{39}Ar ages (Fig. 5.22b) shows a clear correlation with mica composition. M2, which is located near the shear zone with high Xcel content, gives a younger apparent age (<20 Ma), while M1, which is closer to the albite clast with low Xcel content, gives a significantly older age (> 300 Ma). When both types of mica are included in the measured spots, the apparent ages range from 20-300 Ma. The younger part of the *in situ* ^{40}Ar - ^{39}Ar ages for this sample gives a consistent age of 14.0 ± 0.2 Ma (Fig. 5.22d). The step-heating age for both runs similarly produces a flatter age spectrum around 15 Ma (Fig. 5.22d), which coincides with the *in situ* age. Our interpretation is therefore that the low Xcel-content M1 mica is a residual fragmentation inherited from an earlier event (>600 Ma), whereas the high Xcel-content M2 mica is younger and records a younger (~14 Ma) fluid-rock interaction event that occurred during reverse deformation.

Comparing the two samples MW19-21 and MW19-38 we find that they both have two generations of white mica, residual mica inherited from earlier events and deformation-related newborn mica, and the ^{40}Ar - ^{39}Ar ages of the newborn mica from two samples are consistent with each other at 14-15 Ma. However, the two newborn white mica differ in their compositions, and the M2 mica in MW19-21 has a relatively high Xcel value (0.17~0.4), while the M2 mica in MW19-38 has Xcel values of 0.1~0.2. However, it is worth noting that the residual M1 mica in the two samples is also compositionally different, with Xcel values of 0.1~0.17 for the M1 in MW19-21, and Xcel values of 0.2~0.3 for the M1 in MW19-38. Considering that the sampling locations of the two samples are spatially separated by no more than 300 m, we suggest that the cause of the compositional differentiation of the newborn mica may be related to the protolith. The chlorite thermometers of both MW19-21 and MW19-38 give a deformation temperature range of $300 \text{ }^{\circ}\text{C} \sim 350 \text{ }^{\circ}\text{C}$, which agrees with the temperature range given by quartz CPO and mineral deformation behavior ($300 \text{ }^{\circ}\text{C} \sim 400 \text{ }^{\circ}\text{C}$). Although the closure temperature ($300\text{-}500 \text{ }^{\circ}\text{C}$) of the white mica K-Ar system is influenced by many factors (e.g., particle size, chemical composition, and cooling rate) and is still under debate (Villa, 1998). However, our estimated deformation temperatures are close to, or even below, their minimum values, and we therefore suggest that the 14-15 Ma recrystallisation age of white mica represents the age of this reverse deformation event rather than the cooling age.

Sample MW19-10, the quantitative compositional map of white mica based on Xcel content also shows two generations of mica, M1 with a high Xcel content (>0.3) and M2 with a low Xcel content (<0.3). In Fig. 5.7b, there is a clear difference in the position of the M1 and M2 developing in the microstructure. M1 develops closer to the clast while as one moves

further away from the clast, M2 develops more. During the process of *in situ* ^{40}Ar - ^{39}Ar dating (Fig. 5.23a), the age shows a clear correlation with the mica composition. In the second dating run, the low Xcel-content M2 near the shear zone (points 3, 4, 5) clearly has a young apparent age (<55 Ma), while the high Xcel-content M1 near the clast trailing, the age of the point is >80 Ma (Fig. 5.16a, Fig. 5.23a). At the transition place between the two mica, the corresponding age is also intermediate between them. The *in situ* ^{40}Ar - ^{39}Ar age for this sample does not give a consistent age, however the corresponding step-heating dating gives a plateau age of 28.0 ± 0.9 Ma (Fig. 5.23c) and this plateau age is consistent with the minimum age of the *in situ* ^{40}Ar - ^{39}Ar age (~30 Ma), which is followed by an upward shift of the age for the step-heating to 450 Ma. Our interpretation is therefore due to the presence of two types of mica within the sample and transitioning into each other in composition, which are not well distinguished with the current sensitivity of the instrument. The laser single measurement point actually contains different proportions of the two types of mica, and the final apparent age obtained is a mixed age. The mica growth event (~28 Ma) recorded by the step-heating experiments in this period should be a hydroclitic reaction event that led to the formation of low Xcel-content M2 mica during the deformation process. It also suggests that the high Xcel-content M1 mica may be associated with a metamorphic deformation event at ≥ 140 Ma.

Sample MW19-15, the quantitative compositional map of white mica based on Xcel content similarly shows two types of mica, M1 with high Xcel content (>0.4) and M2 with low Xcel content (<0.4), and the M2 (rim) tends to develop around M1 (core) (Fig. 5.8d). In the laser *in situ* ^{40}Ar - ^{39}Ar dating (Fig. 5.23a), the age also shows a clear correlation with mica composition. As shown in Fig. 5.23b, the apparent age of the measured points gradually increases and decreases with increasing M1 content. Therefore, considering the core-rim relationship between M1 and M2, we suggest that M1 was probably formed by recrystallisation on the basis of M2. Although laser *in situ* measurements do not give consistent ages, the maximum and minimum values of the mixed ages similarly place constraints on the ages of M1 and M2, which formed among events ≥ 128 Ma and ≤ 61 Ma, respectively.

Both samples MW19-10 and MW19-15 have two ages of white mica, and both early M1 have relatively high Xcel values, while late M2 has relatively low Xcel values. There is little compositional difference between M1 and M2 in the two samples (Fig. 5.7f, Fig. 5.8g), and the Xcel value intervals are both in the range of 0.1-0.6, which suggests that the mica in the two samples may have the same material origin. Although the laser *in situ* ^{40}Ar - ^{39}Ar ages of the two samples do not give consistent ages, the step-heating dating results in MW19-10 qualify the age of formation of their M1 mica at ~28 Ma. This is also consistent with the event in MW19-15 where it is postulated that M1 may have formed at ≤ 61 Ma. Meanwhile Xue et al. (2021) had previously measured ~26 Ma of syn-tectonic white mica deformation age at an adjacent location in the study area. Considering that the deformation temperatures given by the chlorite thermometers of the two samples are 265 °C and ~350 °C, respectively, which are both lower than the closure temperature of the white mica K-Ar system, we suggest that the age of ~28 Ma should represent the age of the top-to-NW normal shear deformation. Meanwhile, the shear zone has also experienced metamorphic deformation events at ≥ 140 Ma, which may be related to the widespread metamorphic events that occurred regionally during the Late Mesozoic (Yan et al., 2008a; Airaghi et al., 2018a; Xue et al., 2021).

Southwest and North of Pengguan Massif

Sample MW19-1 was collected from the south-western tip of the Pengguan massif and shows a single-component signature in quantitative compositional maps of white mica based on Xcel content (Fig. 5.13e, f), with little differentiation in composition within the mica bands

(Fig. 5.24b). In the corresponding laser *in situ* ^{40}Ar - ^{39}Ar dating (Fig. 5.24a, d), the ages also show good homogeneity, giving a consistent age of 51.3 ± 1.4 Ma. Although the age spectrum of the two runs in the step-heating experiment show a complex pattern in the later stages, they both coincide with the *in situ* laser age at ~ 50 Ma in the initial stage. We therefore suggest that ~ 51 Ma may record the event of white mica growth in this sample. Airaghi et al. (2018a) suggest that the metamorphic temperature at this location does not exceed 360°C by RSCM (thermometer). This is consistent with our determination of a metamorphic temperature of $300^\circ \sim 400^\circ\text{C}$ by quartz CPO and is below the closure temperature of the white mica K-Ar system. We therefore suggest that ~ 51 Ma should represent a recrystallisation age for the mica in this quartz vein, possibly associated with reverse deformation.

Sample MW19-54 was collected from the northern boundary of the Pengguan massif and also shows a single component in the quantitative compositional maps of white mica based on Xcel content (Fig. 5.14e, f), with little differentiation in the mica composition (Fig. 5.24c). Laser *in situ* ^{40}Ar - ^{39}Ar dating shows a stable and consistent age of 149 ± 0.3 Ma. Step-heating dating also have relatively stable spectrum between 135 and 150 Ma. We therefore suggest that the white mica in this sample may have undergone a recrystallisation event at ~ 150 Ma. Considering also the pronounced orientation of the mica grains and the deformation temperatures ($300^\circ \sim 400^\circ\text{C}$) obtained by quartz CPO thermometer are lower than the closure temperature of the white mica K-Ar system, we believe that ~ 150 Ma should represent the age of reverse deformation in this region.

Although previous researchers have carried out corresponding geochronological studies on the hinterland area of LMS (Fig. 5.25), they mostly focused on regional metamorphic events, crystallization and uplift of magma rocks, and there are few direct dating studies on the deformation events of the Wenchuan-Maoxian fault. It is mostly suggested that the regional metamorphic deformation events during the Mesozoic in the hinterland area may be related to the activities of the Wenchuan-Maoxian fault during that period (Yan et al., 2008a; Airaghi et al., 2018a; Xue et al., 2021). The low-temperature thermochronology study also show that the fault may have a complex activity history in the Cenozoic (Tian et al., 2013; Tan et al., 2017; Shen et al., 2019; Furlong et al., 2021), however, there has been a lack of direct evidence about the activity of the Wenchuan-Maoxian fault.

In this paper, we identify a shear zones with strong ductile deformation within the fault zone through field and structure analysis. Precise geochemical compositional analyses and laser *in situ* and step-heating ^{40}Ar - ^{39}Ar dating constrain the time of reverse deformation within the shear zones to ~ 15 Ma, and normal deformation to ~ 28 Ma. The ~ 28 Ma time is also consistent with the ~ 26 Ma obtained near the study area in Xue et al. (2021). Chlorite and quartz CPO thermometers also constrain the temperatures of these two phases of deformation to $300^\circ \sim 350^\circ\text{C}$.

In addition, the results of our samples collected from the northern and southern western tips of the Pengguan massif show that they underwent reverse shearing at ~ 150 Ma and ~ 51 Ma, respectively, and that there was no normal shearing event. Moreover, ~ 150 Ma is also temporally consistent with Yan et al. (2008), who suggested that ductile top-to-E shearing occurred on the north-west side of the Pengguan massif during ~ 160 Ma.

In summary, the Wenchuan-Maoxian fault zone has experienced 26-28 Ma of ductile normal deformation, ~ 15 Ma of ductile reverse deformation, and converted to brittle right-lateral strike-slip deformation with a reverse component at ~ 7 Ma since the Cenozoic area (Ge et al., 2023), which is a complex evolution process with multiple stages and different deformation properties.

3.7 Conclusions

(1) The Wenchuan-Maoxian fault has a ~3 km wide ductile shear zone exposed in the Gengda section, which is significantly different from the surrounding rocks in terms of material composition, deformation intensity and condition.

(2) There are two different phases of ductile deformation in the Wenchuan shear zone, the top-to-NW normal deformation and top-to-E reverse deformation.

(3) ^{40}Ar - ^{39}Ar dating, quartz CPO and chlorite thermometer constrain the top-to-NW shearing occurred at 26-28 Ma with a temperature of ~350°C, and top-to-E reverse shearing occurred at ~15 Ma with a temperature of ~300°C.

(4) Southwest and North of Pengguan Massif show clear reverse deformation at ~51 Ma and ~150 Ma with a temperature of 300 °~ 400 °C, and develop no normal shearing.

4 Summary and conclusion

This thesis takes the Wenchuan-Maoxian fault as the research object, focuses on the fault gouge, fault breccia and mylonite with brittle deformation and ductile deformation, and studies the spatial location, material composition, mineral assemblages and deformation behaviors of these deformed rocks. Combined with remote sensing interpretation, geochemical composition analysis, isotope dating, and low-temperature thermochronology data, we finally determine three different phases of deformation in Wenchuan-Maoxian fault; clarify the relationship between each phase of deformation and geochemical composition and corresponding mineral age distribution; explore the possible influence of different phases of deformation; combine with regional thermochronology data to comprehensively discuss the activities of the fault and the uplift of Longmen Shan, which also provides new insights into the mechanism of the orogeny on the eastern margin of the Tibetan plateau.

The main conclusions are as follows:

- (1) On the basis of fieldwork and indoor analyses, we identified a ductile shear zones with a width of ~3 km within the Wenchuan-Maoxian fault zone by studying rock composition, mineral assemblages, spatial distribution, kinematics, and deformation intensity. There are two different phases of deformation within the shear zone, namely, the top-to-E reverse deformation within the Paleozoic meta-sedimentary unit and the top-to-NW normal deformation within the Proterozoic Pengguan massif. Mineral deformation behavior and quartz CPO constrain the temperatures of these two phases of deformation to 300 °~ 400 °C and 350 °~ 650 °C, respectively.
- (2) Using high-resolution geochemical compositional analyses, laser in situ and step heating ^{40}Ar - ^{39}Ar dating in white mica, the age of the reverse deformation was determined for the first time to be ~15 Ma, and the age of the normal deformation was determined to be ~28 Ma. Chlorite thermometers give deformation temperatures of ~300 ° to ~350 °C, all at the deformation level of the green schist phase.
- (3) Remote sensing interpretation shows that the Wenchuan-Maoxian fault has obvious linear features in the middle part of Longmen Shan, and the linear features of the fault zone are not obvious in the area west of Maoxian and south of Gengda. Along the fault zone, there are a series of brittle deformation zones with a width of 20-50 m. The fault planes are striking to the north-east and dips steeply to the north-west. A large amount of fault gouge and fault breccia are developed in the zone. Field outcrops and microstructures of the fault gouge indicate that the brittle deformation of the faults is a right-lateral strike-slip shear with a reverse component. The dislocated river network and geological units along the fault zone indicate ~25 km of right-lateral offset. The K-Ar age of authigenic illite in the fault gouge constrain the age of brittle deformation to ~7 Ma for the first time, and a horizontal slip rate of ~3.6 mm/yr is estimated for the fault zone.
- (4) The study at the northern and south-western tips of the Pengguan massif, which do not coincide with the Wenchuan-Maoxian fault, shows that the deformation in this area is a ductile reverse deformation, and there is no normal movement develops; the petrological and chronological results show that the age of deformation are ~50 and ~150 Ma, and the deformation temperature is between 300 ° and 400 ° C.
- (5) Thermochronological studies across the fault zone show that there are four stages of differential uplift since ~30 Ma in the upper wall of fault (Xuelongbao), and the footwall (Pengguan massif). The timing of these differential uplifts has obvious similarities with the deformation ages and styles that found in this study: 1, the latest uplift of the upper wall at ~6 Ma corresponds to brittle dextral and reverse faulting at ~7 Ma; 2, the strong uplift of the upper wall between 16.6-14.8 Ma corresponds to

ductile reverse deformation faulting at ~15 Ma; 3, the relative downslip of the upper wall from ~30 Ma to ~25 Ma corresponds to normal shearing at ~28 Ma in the fault.

- (6) Different orogenic mechanisms in the Longmen Shan have different requirements for the kinematic properties of the Wenchuan-Maoxian fault, and our study shows that the fault zone had a top-to-NW normal with right-lateral shear deformation in the Oligocene (~30 Ma), strong eastward reverse deformation during 27-15 Ma, and right-lateral strike-slip deformation with a reverse component since the Late Miocene (~7 Ma). The fault zone has never experienced purely normal motion, and no normal deformation has occurred since the Oligocene. Meanwhile, the lack of partial melting in the granitic Pengguan massif in the area, the discontinuous low-velocity high-conductivity zone (LVZ) on the eastern margin of the Tibetan Plateau, and the fact that the LVZ stops at 25 km west of the Longmen Shan, we suggest that crustal flow may not be the active mechanism that produced and maintained the steep topography of the Longmen Shan. The present-day topography and geomorphology of the Longmen Shan are the result of accretionary stacking that occurred in the Earth's crust.

Reference

- Adams, B. A., and Hodges, K. V., 2022, Potential Influences of Middle and Lower Crustal Flow on Landscape Evolution: Insights From the Himalayan-Tibetan Orogen, *Treatise on Geomorphology*, Academic Press, p. 729-748.
- Airaghi, L., 2017, petro-chronological study of the Longmen Shan thrust belt (eastern Tibet) : geological inheritance and implication for the present geodynamics.
- Airaghi, L., Bellahsen, N., Dubacq, B., Chew, D., Rosenberg, C., Janots, E., Waldner, M., and Magnin, V., 2020, Pre-orogenic upper crustal softening by lower greenschist facies metamorphic reactions in granites of the central Pyrenees: *Journal of Metamorphic Geology*, v. 38, no. 2, p. 183-204.
- Airaghi, L., de Sigoyer, J., Guillot, S., Robert, A., Warren, C. J., and Deldicque, D., 2018a, The Mesozoic Along-Strike Tectonometamorphic Segmentation of Longmen Shan (Eastern Tibetan Plateau): *Tectonics*, v. 37, no. 12, p. 4655-4678.
- Airaghi, L., de Sigoyer, J., Lanari, P., Guillot, S., Vidal, O., Monié, P., Sautter, B., and Tan, X., 2017a, Total exhumation across the Beichuan fault in the Longmen Shan (eastern Tibetan plateau, China): Constraints from petrology and thermobarometry: *Journal of Asian Earth Sciences*, v. 140, p. 108-121.
- Airaghi, L., Janots, E., Lanari, P., de Sigoyer, J., and Magnin, V., 2019, Allanite Petrochronology in Fresh and Retrogressed Garnet–Biotite Metapelites from the Longmen Shan (Eastern Tibet): *Journal of Petrology*, v. 60, no. 1, p. 151-176.
- Airaghi, L., Lanari, P., de Sigoyer, J., and Guillot, S., 2017b, Microstructural vs compositional preservation and pseudomorphic replacement of muscovite in deformed metapelites from the Longmen Shan (Sichuan, China): *Lithos*, v. 282-283, p. 262-280.
- Airaghi, L., Warren, C. J., de Sigoyer, J., Lanari, P., and Magnin, V., 2018b, Influence of dissolution/precipitation reactions on metamorphic greenschist to amphibolite facies mica $^{40}\text{Ar}/^{39}\text{Ar}$ ages in the Longmen Shan (eastern Tibet): *Journal of Metamorphic Geology*, v. 36, no. 7, p. 933-958.
- Arne, D., Worley, B., Wilson, C., Chen, S. F., Foster, D., Luo, Z. L., Liu, S. G., and Dirks, P., 1997, Differential exhumation in response to episodic thrusting along the eastern margin of the Tibetan Plateau: *Tectonophysics*, v. 280, no. 3-4, p. 239-256.
- Augier, R., Agard, P., Monié, P., Jolivet, L., Robin, C., and Booth-Rea, G., 2005, Exhumation, doming and slab retreat in the Betic Cordillera (SE Spain): in situ $^{40}\text{Ar}/^{39}\text{Ar}$ ages and P–T–t paths for the Nevado-Filabride complex: *Journal of Metamorphic Geology*, v. 23, no. 5, p. 357-381.
- Bai, D., Unsworth, M. J., Meju, M. A., Ma, X., Teng, J., Kong, X., Sun, Y., Sun, J., Wang, L., Jiang, C., Zhao, C., Xiao, P., and Liu, M., 2010, Crustal deformation of the eastern Tibetan plateau revealed by magnetotelluric imaging: *Nature Geoscience*, v. 3, no. 5, p. 358-362.
- Beaudoin, A., Scaillet, S., Mora, N., Jolivet, L., and Augier, R., 2020, In Situ and Step-Heating ($^{40}\text{Ar}/^{39}\text{Ar}$) Dating of White Mica in Low-Temperature Shear Zones (Tenda Massif, Alpine Corsica, France): *Tectonics*, v. 39, no. 12.

- Beaumont, C., Jamieson, R. A., Nguyen, M., and Lee, B., 2001, Himalayan tectonics explained by extrusion of a low-viscosity crustal channel coupled to focused surface denudation: *Nature*, v. 414, no. 6865, p. 738-742.
- Beaumont, C., Nguyen, M., Jamieson, R. A., and Ellis, S., 2006, Crustal flow modes in large hot orogens: SPECIAL PUBLICATION-GEOLOGICAL SOCIETY OF LONDON, v. 268, p. 91.
- Bellanger, M., Augier, R., Bellahsen, N., Jolivet, L., Monié, P., Baudin, T., and Beyssac, O., 2015, Shortening of the European Dauphinois margin (Oisans Massif, Western Alps): New insights from RSCM maximum temperature estimates and $^{40}\text{Ar}/^{39}\text{Ar}$ in situ dating: *Journal of Geodynamics*, v. 83, p. 37-64.
- Beltrando, M., Lister, G. S., Forster, M., Dunlap, W. J., Fraser, G., and Hermann, J., 2009, Dating microstructures by the $^{40}\text{Ar}/^{39}\text{Ar}$ step-heating technique: Deformation–pressure–temperature–time history of the Penninic Units of the Western Alps: *Lithos*, v. 113, no. 3-4, p. 801-819.
- Bollinger, L., Henry, P., and Avouac, J.-P., 2006, Mountain building in the Nepal Himalaya: Thermal and kinematic model: *Earth and Planetary Science Letters*, v. 244, no. 1-2, p. 58-71.
- Bourdelle, F., and Cathelineau, M., 2015, Low-temperature chlorite geothermometry: a graphical representation based on a $T-R_2^{+}-Si$ diagram: *European Journal of Mineralogy*, v. 27, no. 5, p. 617-626.
- Bourdelle, F., Parra, T., Beyssac, O., Chopin, C., and Vidal, O., 2013, Clay minerals as geothermometer: A comparative study based on high spatial resolution analyses of illite and chlorite in Gulf Coast sandstones (Texas, U.S.A.): *American Mineralogist*, v. 98, no. 5-6, p. 914-926.
- Boutonnet, E., Leloup, P. H., Sassier, C., Gardien, V., and Ricard, Y., 2013, Ductile strain rate measurements document long-term strain localization in the continental crust: *Geology*, v. 41, no. 8, p. 819-822.
- Braitenberg, C., Zadro, M., Fang, J., Wang, Y., and Hsu, H., 2000, The gravity and isostatic Moho undulations in Qinghai–Tibet plateau: *Journal of Geodynamics*, v. 30, no. 5, p. 489-505.
- Bruguier, O., Lancelot, J., and Malavieille, J., 1997, U–Pb dating on single detrital zircon grains from the Triassic Songpan–Ganze flysch (Central China): provenance and tectonic correlations: *Earth Planetary Science Letters*, v. 152, no. 1-4, p. 217-231.
- Brunet, C., Monié, P., Jolivet, L., and Cadet, J.-P., 2000, Migration of compression and extension in the Tyrrhenian Sea, insights from $^{40}\text{Ar}/^{39}\text{Ar}$ ages on micas along a transect from Corsica to Tuscany: *Tectonophysics*, v. 321, no. 1, p. 127-155.
- Burchfiel, B. C., Royden, L. H., van der Hilst, R. D., Hager, B. H., Chen, Z., King, R. W., Li, C., Lü, J., Yao, H., and Kirby, E., 2008, A geological and geophysical context for the Wenchuan earthquake of 12 May 2008, Sichuan, People's Republic of China: *GSA Today*, v. 18, no. 7.

- Burchfiel, B. C., Zhiliang, C., Yupinc, L., and Royden, L. H., 1995, Tectonics of the Longmen Shan and Adjacent Regions, Central China: *International Geology Review*, v. 37, no. 8, p. 661-735.
- Caine, J. S., Evans, J. P., and Forster, C., 1996, Fault zone architecture and permeability structure: *Geology*, v. 24, no. 11, p. 1025-1028.
- Calassou, S., 1994, Etude tectonique d'une chaîne de décollement: Tectonique triasique et tertiaire de la chaîne de Songpan Garzé (est Tibet): Géométrie et cinématique des déformations dans les prismes d'accrétion sédimentaire: Modélisation analogique: Montpellier 2.
- Cao, K., Wang, G., Leloup, P. H., Mahéo, G., Xu, Y., van der Beek, P. A., Replumaz, A., and Zhang, K., 2019, Oligocene-Early Miocene Topographic Relief Generation of Southeastern Tibet Triggered by Thrusting: *Tectonics*, v. 38, no. 1, p. 374-391.
- Cardello, G. L., Di Vincenzo, G., Giorgetti, G., Zwingmann, H., and Mancktelow, N., 2019, Initiation and development of the Pennine Basal Thrust (Swiss Alps): a structural and geochronological study of an exhumed megathrust: *Journal of Structural Geology*, v. 126, p. 338-356.
- Castonguay, S., Ruffet, G., and Tremblay, A., 2007, Dating polyphase deformation across low-grade metamorphic belts: An example based on $^{40}\text{Ar}/^{39}\text{Ar}$ muscovite age constraints from the southern Quebec Appalachians, Canada: *Geological Society of America Bulletin*, v. 119, no. 7-8, p. 978-992.
- Cattin, R., Martelet, G., Henry, P., Avouac, J., Diament, M., and Shakya, T., 2001, Gravity anomalies, crustal structure and thermo-mechanical support of the Himalaya of Central Nepal: *Geophysical Journal International*, v. 147, no. 2, p. 381-392.
- Champagnac, J., Molnar, P., Anderson, R., Sue, C., and Delacou, B., 2007, Quaternary erosion-induced isostatic rebound in the western Alps: *Geology*, v. 35, no. 3, p. 195-198.
- Chang, E. Z., 2000, Geology and tectonics of the Songpan-Ganzi fold belt, southwestern China: *International Geology Review*, v. 42, no. 9, p. 813-831.
- Chen, S., Deng, Q., and Zhao, X., 1995a, Deformational Characteristics, Evolutionary History, and Deformation Mechanism of the Middle Longmenshan Thrust-Nappes and Related Tectonics: *Chinese Science Abstracts Series B*, v. 3, no. 14.
- Chen, S., Deng, Q., Zhao, X., Dirks, C. J. L. W. P., Luo, Z., and Liu, S., 1994a, Deformational characteristics, evolutionary history, and deformation mechanism of the middle Longmenshan thrust nappes and related tectonics: *Seismology and geology*, v. 16, no. 4, p. 413-421.
- Chen, S. F., Wilson, C., Luo, Z. L., and Deng, Q. D., 1994b, The evolution of the western Sichuan foreland basin, southwestern China: *Journal of Southeast Asian Earth Sciences*, v. 10, no. 3-4, p. 159-168.
- Chen, S. F., and Wilson, C. J., 1996, Emplacement of the Longmen Shan Thrust—Nappe Belt along the eastern margin of the Tibetan Plateau: *Journal of Structural Geology*, v. 18, no. 4, p. 413-430.

- Chen, S. F., Wilson, C. J., and Worley, B., 1995b, Tectonic transition from the Songpan-Garzê fold belt to the Sichuan Basin, south-western China: *Basin Research*, v. 7, no. 3, p. 235-253.
- Choi, J.-H., Edwards, P., Ko, K., and Kim, Y.-S., 2016, Definition and classification of fault damage zones: A review and a new methodological approach: *Earth-Science Reviews*, v. 152, p. 70-87.
- Clark, M. K., Bush, J. W. M., and Royden, L. H., 2005a, Dynamic topography produced by lower crustal flow against rheological strength heterogeneities bordering the Tibetan Plateau: *Geophysical Journal International*, v. 162, no. 2, p. 575-590.
- Clark, M. K., Farley, K. A., Zheng, D., Wang, Z., and Duvall, A. R., 2010, Early Cenozoic faulting of the northern Tibetan Plateau margin from apatite (U–Th)/He ages: *Earth and Planetary Science Letters*, v. 296, no. 1-2, p. 78-88.
- Clark, M. K., House, M., Royden, L., Whipple, K., Burchfiel, B., Zhang, X., and Tang, W., 2005b, Late Cenozoic uplift of southeastern Tibet: *Geology*, v. 33, no. 6, p. 525-528.
- Clark, M. K., and Royden, L. H., 2000, Topographic ooze: Building the eastern margin of Tibet by lower crustal flow: *Geology*, v. 28, no. 8.
- Clauer, N., 2013, The K-Ar and $^{40}\text{Ar}/^{39}\text{Ar}$ methods revisited for dating fine-grained K-bearing clay minerals: *Chemical Geology*, v. 354, p. 163-185.
- Condon, D., Hodges, K., Alsop, G. I., and White, A., 2006, Laser ablation $^{40}\text{Ar}/^{39}\text{Ar}$ dating of metamorphic fabrics in the Caledonides of north Ireland: *Journal of the Geological Society*, v. 163, no. 2, p. 337-345.
- Cook, K. L., and Royden, L. H., 2008. The role of crustal strength variations in shaping orogenic plateaus, with application to Tibet. *Journal of Geophysical Research: Solid Earth*, 113(B8).
- Dai, J., Zhao, X., Wang, C., Zhu, L., Li, Y., and Finn, D., 2012, The vast proto-Tibetan Plateau: New constraints from Paleogene Hoh Xil Basin: *Gondwana Research*, v. 22, no. 2, p. 434-446.
- De Sigoyer, J., Vanderhaeghe, O., Duchêne, S., and Billerot, A., 2014, Generation and emplacement of Triassic granitoids within the Songpan Ganze accretionary-orogenic wedge in a context of slab retreat accommodated by tear faulting, Eastern Tibetan plateau, China: *Journal of Asian Earth Sciences*, v. 88, p. 192-216.
- Dewey, J. F., Shackleton, R. M., Chengfa, C., and Yiyin, S., 1988, The tectonic evolution of the Tibetan Plateau. *Philosophical Transactions of the Royal Society of London: Series A, Mathematical Physical Sciences*, v. 327, no. 1594, p. 379-413.
- Di Vincenzo, G., Carosi, R., and Palmeri, R., 2004, The Relationship between Tectono-metamorphic Evolution and Argon Isotope Records in White Mica: Constraints from in situ ^{40}Ar – ^{39}Ar Laser Analysis of the Variscan Basement of Sardinia: *JOURNAL OF PETROLOGY*.
- Di Vincenzo, G., Grande, A., Prosser, G., Cavazza, W., and DeCelles, P. G., 2016, ^{40}Ar – ^{39}Ar laser dating of ductile shear zones from central Corsica (France): evidence of Alpine

- (middle to late Eocene) syn-burial shearing in Variscan granitoids: *Lithos*, v. 262, p. 369-383.
- Dirks, P., Wilson, C., Chen, S., Luo, Z., and Liu, S., 1994, Tectonic evolution of the NE margin of the Tibetan Plateau; evidence from the central Longmen Mountains, Sichuan Province, China: *Journal of Southeast Asian Earth Sciences*, v. 9, no. 1-2, p. 181-192.
- Dubacq, B., Vidal, O., and De Andrade, V., 2009, Dehydration of dioctahedral aluminous phyllosilicates: thermodynamic modelling and implications for thermobarometric estimates: *Contributions to Mineralogy and Petrology*, v. 159, no. 2, p. 159-174.
- Dunlap, W. J., Teyssier, C., McDougall, I., and Baldwin, S., 1991, Ages of deformation from K/Ar and $^{40}\text{Ar}/^{39}\text{Ar}$ dating of white micas: *Geology*, v. 19, no. 12, p. 1213-1216.
- Duvall, A. R., Clark, M. K., van der Pluijm, B. A., and Li, C., 2011, Direct dating of Eocene reverse faulting in northeastern Tibet using Ar-dating of fault clays and low-temperature thermochronometry: *Earth and Planetary Science Letters*, v. 304, no. 3-4, p. 520-526.
- Engi, M., Lanari, P., and Kohn, M. J., 2017, Significant ages—An introduction to petrochronology: *Reviews in Mineralogy Geochemistry*, v. 83, no. 1, p. 1-12.
- Feng, S. y., Zhang, P. z., Liu, B. j., Wang, M., Zhu, S. b., Ran, Y. k., Wang, W. t., Zhang, Z. q., Zheng, W. j., Zheng, D. w., Zhang, H. p., and Tian, X. f., 2016, Deep crustal deformation of the Longmen Shan, eastern margin of the Tibetan Plateau, from seismic reflection and Finite Element modeling: *Journal of Geophysical Research: Solid Earth*, v. 121, no. 2, p. 767-787.
- Fitz-Díaz, E., Camprubí, A., Cienfuegos-Alvarado, E., Morales-Puente, P., Schleicher, A. M., and van der Pluijm, B., 2014, Newly-formed illite preserves fluid sources during folding of shale and limestone rocks; an example from the Mexican Fold-Thrust Belt: *Earth and Planetary Science Letters*, v. 391, p. 263-273.
- Fu, B., Shi, P., Guo, H., Okuyama, S., Ninomiya, Y., and Wright, S., 2011, Surface deformation related to the 2008 Wenchuan earthquake, and mountain building of the Longmen Shan, eastern Tibetan Plateau: *Journal of Asian Earth Sciences*, v. 40, no. 4, p. 805-824.
- Furlong, K. P., Kirby, E., Creason, C. G., Kamp, P. J. J., Xu, G., Danišík, M., Shi, X., and Hodges, K. V., 2021, Exploiting Thermochronology to Quantify Exhumation Histories and Patterns of Uplift Along the Margins of Tibet: *Frontiers in Earth Science*, v. 9.
- Gao, M., Zeilinger, G., Xu, X., Tan, X., Wang, Q., and Hao, M., 2016, Active tectonics evaluation from geomorphic indices for the central and the southern Longmenshan range on the Eastern Tibetan Plateau, China: *Tectonics*, v. 35, no. 8, p. 1812-1826.
- Gaudemer, Y., Tapponnier, P., and Turcotte, D., 1989, River offsets across active strike-slip faults: *Ann. tecton.*, v. 3, no. 2, p. 55-76.
- Gibbons, W., Doig, R., Gordon, T., Murphy, B., Reynolds, P., and White, J. C., 1996, Mylonite to megabreccia: tracking fault events within a transcurrent terrane boundary in Nova Scotia, Canada: *Geology*, v. 24, no. 5, p. 411-414.
- Godard, V., Lavé, J., Carcaillet, J., Cattin, R., Bourlès, D., and Zhu, J., 2010, Spatial distribution of denudation in Eastern Tibet and regressive erosion of plateau margins: *Tectonophysics*, v. 491, no. 1-4, p. 253-274.

- Godard, V., Pik, R., Lavé, J., Cattin, R., Tibari, B., de Sigoyer, J., Pubellier, M., and Zhu, J., 2009, Late Cenozoic evolution of the central Longmen Shan, eastern Tibet: Insight from (U-Th)/He thermochronometry: *Tectonics*, v. 28, no. TC5009.
- Grathoff, G. H., and Moore, D., 1996, Illite polytype quantification using WILDFIRE© calculated X-ray diffraction patterns: *clay Minerals*, v. 44, p. 835-842.
- Grathoff, G. H., Moore, D. M., Hay, R. L., and Wemmer, K., 2001, Origin of illite in the lower Paleozoic of the Illinois basin: evidence for brine migrations: *Geological Society of America Bulletin*, v. 113, no. 8, p. 1092-1104.
- Grujic, D., Casey, M., Davidson, C., Hollister, L. S., Kündig, R., Pavlis, T., and Schmid, S., 1996, Ductile extrusion of the Higher Himalayan Crystalline in Bhutan: evidence from quartz microfabrics: *Tectonophysics*, v. 260, no. 1-3, p. 21-43.
- Guillot, S., Garzanti, E., Baratoux, D., Marquer, D., Mahéo, G., and de Sigoyer, J., 2003, Reconstructing the total shortening history of the NW Himalaya: *Geochemistry, Geophysics, Geosystems*, v. 4, no. 7.
- Guo, X., Gao, R., Keller, G. R., Xu, X., Wang, H., and Li, W., 2013a, Imaging the crustal structure beneath the eastern Tibetan Plateau and implications for the uplift of the Longmen Shan range: *Earth Planetary Science Letters*, v. 379, p. 72-80.
- Guo, X., Gao, R., Randy Keller, G., Xu, X., Wang, H., and Li, W., 2013b, Imaging the crustal structure beneath the eastern Tibetan Plateau and implications for the uplift of the Longmen Shan range: *Earth and Planetary Science Letters*, v. 379, p. 72-80.
- Guo, X., Gao, R., Wang, H., Li, W., Keller, G., Xu, X., Li, H., and Encarnacion, J., 2015, Crustal architecture beneath the Tibet-Ordos transition zone, NE Tibet, and the implications for plateau expansion: *Geophysical Research Letters*, v. 42, no. 24, p. 10,631-610,639.
- Guo, X., Keller, G. R., Gao, R., Xu, X., Wang, H., and Li, W., 2014, Irregular western margin of the Yangtze block as a cause of variation in tectonic activity along the Longmen Shan fault zone, eastern Tibet: *International Geology Review*, v. 56, no. 4, p. 473-480.
- Haines, S. H., and van der Pluijm, B., 2010, Dating the detachment fault system of the Ruby Mountains, Nevada: Significance for the kinematics of low-angle normal faults: *Tectonics*, v. 29, no. 4.
- Haines, S. H., and van der Pluijm, B. A., 2008, Clay quantification and Ar–Ar dating of synthetic and natural gouge: Application to the Miocene Sierra Mazatán detachment fault, Sonora, Mexico: *Journal of Structural Geology*, v. 30, no. 4, p. 525-538.
- Hames, W. E., and Cheney, J., 1997, On the loss of 40Ar^* from muscovite during polymetamorphism: *Geochimica et Cosmochimica Acta*, v. 61, no. 18, p. 3863-3872.
- Harrowfield, M. J., and Wilson, C. J., 2005, Indosinian deformation of the Songpan Garze fold belt, northeast Tibetan Plateau: *Journal of Structural Geology*, v. 27, no. 1, p. 101-117.
- He, X. L., Li, H. B., Wang, H., Zhang, L., Xu, Z. Q., and Si, J. L., 2018, Creeping Along the Guanxian-Anxian Fault of the 2008 Mw 7.9 Wenchuan Earthquake in the Longmen Shan, China: *Tectonics*, v. 37, no. 7, p. 2124-2141.

- Heidelbach, F., Kunze, K., and Wenk, H.-R., 2000, Texture analysis of a recrystallized quartzite using electron diffraction in the scanning electron microscope: *Journal of Structural Geology*, v. 22, no. 1, p. 91-104.
- Hetényi, G., Cattin, R., Vergne, J., and Nábělek, J. L., 2006, The effective elastic thickness of the India Plate from receiver function imaging, gravity anomalies and thermomechanical modelling: *Geophysical Journal International*, v. 167, no. 3, p. 1106-1118.
- Hetényi, G., Vergne, J., Bollinger, L., and Cattin, R., 2011, Discontinuous low-velocity zones in southern Tibet question the viability of the channel flow model: *Geological Society, London, Special Publications*, v. 353, no. 1, p. 99-108.
- Huang B S, Chen J H, Liu Q Y, et al., 2012, Estimation of rupture processes of the 2008 Wenchuan Earthquake from joint analyses of two regional seismic arrays[J]. *Tectonophysics*, 578: 87-97.
- Huang, Y., Wu, J., Zhang, T., and Zhang, D. 2008. Relocation of the M 8.0 Wenchuan earthquake and its aftershock sequence. *Science in China Series D: Earth Sciences*, 51, 1703-1711.
- Hubbard, J., and Shaw, J. H., 2009, Uplift of the Longmen Shan and Tibetan plateau, and the 2008 Wenchuan (M = 7.9) earthquake: *Nature*, v. 458, no. 7235, p. 194-197.
- Hubbard, J., Shaw, J. H., and Klinger, Y., 2010, Structural Setting of the 2008 Mw 7.9 Wenchuan, China, Earthquake: *Bulletin of the Seismological Society of America*, v. 100, no. 5B, p. 2713-2735.
- Hunziker, J., Frey, M., Clauer, N., Dallmeyer, R., Friedrichsen, H., Flehmig, W., Hochstrasser, K., Roggwiler, P. t., and Schwander, H., 1986, The evolution of illite to muscovite: mineralogical and isotopic data from the Glarus Alps, Switzerland: *Contributions to Mineralogy Petrology*, v. 92, no. 2, p. 157-180.
- Isik, V., Tekeli, O., and Seyitoglu, G., 2004, The $^{40}\text{Ar}/^{39}\text{Ar}$ age of extensional ductile deformation and granitoid intrusion in the northern Menderes core complex: implications for the initiation of extensional tectonics in western Turkey: *Journal of Asian Earth Sciences*, v. 23, no. 4, p. 555-566.
- Jamieson, R. A., and Beaumont, C., 2013, On the origin of orogens: *Bulletin*, v. 125, no. 11-12, p. 1671-1702.
- Jamieson, R. A., Beaumont, C., Medvedev, S., and Nguyen, M. H., 2004, Crustal channel flows: 2. Numerical models with implications for metamorphism in the Himalayan-Tibetan orogen: *Journal of Geophysical Research: Solid Earth*, v. 109, no. B6.
- Jamtveit, B., 2010, Metamorphism: from patterns to processes: *Elements*, v. 6, no. 3, p. 149-152.
- Jia, D., Li, Y., Lin, A., Wang, M., Chen, W., Wu, X., and Luo, L. 2010. Structural model of 2008 Mw 7.9 Wenchuan earthquake in the rejuvenated Longmen Shan thrust belt, China. *Tectonophysics*, 491(1-4), 174-184.
- Jia, D., Li, Y., Yan, B., Li, Z., Wang, M., Chen, Z., and Zhang, Y., 2020, The Cenozoic thrusting sequence of the Longmen Shan fold-and-thrust belt, Eastern margin of the Tibetan plateau: Insights from low-temperature thermochronology: *Journal of Asian Earth Sciences*.

- Jiang, M., Peng, M., Qiao, X., Yang, J., Tan, H., Qian, R., and Xu, L. 2017. Rediscussion on the geodynamics of the 2008 Wenchuan earthquake: New seismic reflection evidence for crustal structure of the Longmenshan. *Journal of Geodynamics*, 108, 1-12.
- Jiao, L., Tapponnier, P., Donzé, F. V., Scholtès, L., Gaudemer, Y., and Xu, X., 2023, Discrete Element Modelling of Southeast Asia's 3D Lithospheric Deformation during the Indian Collision: *Journal of Geophysical Research: Solid Earth*, p. e2022JB025578.
- Jolivet, M., Brunel, M., Seward, D., Xu, Z., Yang, J., Malavieille, J., Roger, F., Leyreloup, A., Arnaud, N., and Wu, C., 2003, Neogene extension and volcanism in the Kunlun Fault Zone, northern Tibet: New constraints on the age of the Kunlun Fault: *Tectonics*, v. 22, no. 5, p. n/a-n/a.
- Kellett, D. A., Warren, C., Larson, K. P., Zwingmann, H., van Staal, C. R., and Rogers, N., 2016, Influence of deformation and fluids on Ar retention in white mica: Dating the Dover Fault, Newfoundland Appalachians: *Lithos*, v. 254, p. 1-17.
- Kim, Y.-S., Peacock, D. C., and Sanderson, D., 2004, Fault damage zones: *Journal of structural geology*, v. 26, no. 3, p. 503-517.
- Kirby, E., Reiners, P. W., Krol, M. A., Whipple, K. X., Hodges, K. V., Farley, K. A., Tang, W., and Chen, Z., 2002, Late Cenozoic evolution of the eastern margin of the Tibetan Plateau: Inferences from $^{40}\text{Ar}/^{39}\text{Ar}$ and (U-Th)/He thermochronology: *Tectonics*, v. 21, no. 1, p. 1-20.
- Klemperer, S. L., 2006, Crustal flow in Tibet: geophysical evidence for the physical state of Tibetan lithosphere, and inferred patterns of active flow: *Geological Society, London, Special Publications*, v. 268, no. 1, p. 39-70.
- Kligfield, R., Hunziker, J., Dallmeyer, R., and Schamel, S., 1986, Dating of deformation phases using K-Ar and $^{40}\text{Ar}/^{39}\text{Ar}$ techniques: results from the Northern Apennines: *Journal of Structural Geology*, v. 8, no. 7, p. 781-798.
- Kohn, M. J., 2008, PTt data from central Nepal support critical taper and repudiate large-scale channel flow of the Greater Himalayan Sequence: *Geological Society of America Bulletin*, v. 120, no. 3-4, p. 259-273.
- Kono, M., 1974, Gravity anomalies in east Nepal and their implications to the crustal structure of the Himalayas: *Geophysical Journal International*, v. 39, no. 2, p. 283-299.
- Kralik, M., Klima, K., and Riedmüller, G., 1987, Dating fault gouges: *Nature*, v. 327, no. 6120, p. 315-317.
- Kuo, L.-W., Di Felice, F., Spagnuolo, E., Di Toro, G., Song, S.-R., Aretusini, S., Li, H., Suppe, J., Si, J., and Wen, C.-Y., 2017, Fault gouge graphitization as evidence of past seismic slip: *Geology*, v. 45, no. 11, p. 979-982.
- Lanari, P., Rolland, Y., Schwartz, S., Vidal, O., Guillot, S., Tricart, P., and Dumont, T., 2014a, P-T-t estimation of deformation in low-grade quartz-feldspar-bearing rocks using thermodynamic modelling and $^{40}\text{Ar}/^{39}\text{Ar}$ dating techniques: example of the Plan-de-Phasy shear zone unit (Briançonnais Zone, Western Alps): *Terra Nova*, v. 26, no. 2, p. 130-138.

- Lanari, P., Vidal, O., De Andrade, V., Dubacq, B., Lewin, E., Grosch, E. G., and Schwartz, S., 2014b, XMapTools: A MATLAB©-based program for electron microprobe X-ray image processing and geothermobarometry: *Computers & Geosciences*, v. 62, p. 227-240.
- Lanari, P., Wagner, T., and Vidal, O., 2014c, A thermodynamic model for di-trioctahedral chlorite from experimental and natural data in the system MgO–FeO–Al₂O₃–SiO₂–H₂O: applications to P–T sections and geothermometry: *Contributions to Mineralogy and Petrology*, v. 167, no. 2.
- Laurent, V., Scaillet, S., Jolivet, L., Augier, R., and Roche, V., 2021, 40Ar behaviour and exhumation dynamics in a subduction channel from multi-scale 40Ar/39Ar systematics in phengite: *Geochimica et Cosmochimica Acta*, v. 311, p. 141-173.
- LAW, R. D., SCHMID, S. M., and WHEELER, J., 1990, Simple shear deformation and quartz crystallographic fabrics: a possible natural example from the Torridon area of NW Scotland: *Journal of Structural Geology*, v. 12, p. 29-45.
- Leloup, P., Mahéo, G., Arnaud, N., Kali, E., Boutonnet, E., Liu, D., Xiaohan, L., and Haibing, L., 2010, The South Tibet detachment shear zone in the Dingtgye area: Time constraints on extrusion models of the Himalayas: *Earth and Planetary Science Letters*, v. 292, no. 1-2, p. 1-16.
- Leloup, P. H., Liu, X., Mahéo, G., Paquette, J.-L., Arnaud, N., Aubray, A., and Liu, X., 2015, New constraints on the timing of partial melting and deformation along the Nyalam section (central Himalaya): implications for extrusion models: *Geological Society, London, Special Publications*, v. 412, no. 1, p. 131-175.
- Lei, J., and Zhao, D. 2009. Structural heterogeneity of the Longmenshan fault zone and the mechanism of the 2008 Wenchuan earthquake (Ms 8.0). *Geochemistry, Geophysics, Geosystems*, 10(10).
- Li, Y., Jia, D., Shaw, J. H., Hubbard, J., Lin, A., Wang, M., and Wu, L. 2010. Structural interpretation of the coseismic faults of the Wenchuan earthquake: Three-dimensional modeling of the Longmen Shan fold-and-thrust belt. *Journal of Geophysical Research: Solid Earth*, 115(B4).
- Li, C.-Y., Wei, Z.-Y., Ye, J.-Q., Han, Y.-B., and Zheng, W.-J., 2010a, Amounts and styles of coseismic deformation along the northern segment of surface rupture, of the 2008 Wenchuan Mw 7.9 earthquake, China: *Tectonophysics*, v. 491, no. 1-4, p. 35-58.
- Li, H., Su, W., Wang, C.-Y., and Huang, Z., 2009, Ambient noise Rayleigh wave tomography in western Sichuan and eastern Tibet: *Earth and Planetary Science Letters*, v. 282, no. 1-4, p. 201-211.
- Li, H., Wang, H., Xu, Z., Si, J., Pei, J., Li, T., Huang, Y., Song, S.-R., Kuo, L.-W., Sun, Z., Chevalier, M.-L., and Liu, D., 2013a, Characteristics of the fault-related rocks, fault zones and the principal slip zone in the Wenchuan Earthquake Fault Scientific Drilling Project Hole-1 (WFSD-1): *Tectonophysics*, v. 584, p. 23-42.
- Li, H., Wang, H., Yang, G., Xu, Z., Li, T., Si, J., Sun, Z., Huang, Y., Chevalier, M.-L., Zhang, W., and Zhang, J., 2016, Lithological and structural characterization of the Longmen Shan

- fault belt from the 3rd hole of the Wenchuan Earthquake Fault Scientific Drilling project (WFSD-3): *International Journal of Earth Sciences*, v. 105, no. 8, p. 2253-2272.
- Li, H., Xu, Z., Niu, Y., Kong, G., Huang, Y., Wang, H., Si, J., Sun, Z., Pei, J., Gong, Z., Chevalier, M.-L., and Liu, D., 2014a, Structural and physical property characterization in the Wenchuan earthquake Fault Scientific Drilling project — hole 1 (WFSD-1): *Tectonophysics*, v. 619-620, p. 86-100.
- Li, Y., Allen, P. A., Densmore, A. L., and Qiang, X., 2003, Evolution of the Longmen Shan foreland basin (western Sichuan, China) during the Late Triassic Indosinian orogeny: *basin Research*, v. 15, no. 1, p. 117-138.
- Li, Y., Jia, D., Shaw, J. H., Hubbard, J., Lin, A., Wang, M., Luo, L., Li, H., and Wu, L., 2010b, Structural interpretation of the coseismic faults of the Wenchuan earthquake: Three-dimensional modeling of the Longmen Shan fold-and-thrust belt: *Journal of Geophysical Research*, v. 115, no. B4.
- Li, Y., Li, H., Zhou, R., Su, D., Yan, L., and Yan, Z., 2014b, Crustal thickening or isostatic rebound of orogenic wedge deduced from tectonostratigraphic units in Indosinian foreland basin, Longmen Shan, China: *Tectonophysics*, v. 619-620, p. 1-12.
- Li, Y., Su, D.-c., Zhou, R.-j., Li, H.-b., Densmore, A. L., Yan, L., and Yan, Z.-k., 2013b, Episodic orogeny deduced from coeval sedimentary sequences in the foreland basin and its implication for uplift process of Longmen Mountain, China: *Journal of Mountain Science*, v. 10, no. 1, p. 29-42.
- Li, Z.-W., Liu, S., Chen, H., Deng, B., Hou, M., Wu, W., and Cao, J., 2012, Spatial variation in Meso-Cenozoic exhumation history of the Longmen Shan thrust belt (eastern Tibetan Plateau) and the adjacent western Sichuan basin: Constraints from fission track thermochronology: *Journal of Asian Earth Sciences*, v. 47, p. 185-203.
- Li, Z.-X., Li, X., Kinny, P., and Wang, J., 1999, The breakup of Rodinia: did it start with a mantle plume beneath South China?: *Earth and Planetary Science Letters*, v. 173, no. 3, p. 171-181.
- Li, Z., Kamp, P. J., Liu, S., Xu, G., Tong, K., Danišik, M., Wang, Z., Li, J., Deng, B., and Ran, B., 2023, Late Cretaceous–Cenozoic thermal structure and exhumation of the Eastern Tibetan Plateau margin and its orogenic wedge: *Earth-Science Reviews*, p. 104319.
- Lin, A., Ren, Z., and Kumahara, Y., 2010, Structural analysis of the coseismic shear zone of the 2008 Mw 7.9 Wenchuan earthquake, China: *Journal of Structural Geology*, v. 32, no. 6, p. 781-791.
- Liu, Q. Y., van der Hilst, R. D., Li, Y., Yao, H. J., Chen, J. H., Guo, B., Qi, S. H., Wang, J., Huang, H., and Li, S. C., 2014, Eastward expansion of the Tibetan Plateau by crustal flow and strain partitioning across faults: *Nature Geoscience*, v. 7, no. 5, p. 361-365.
- Lloyd, G., 2000, Grain boundary contact effects during faulting of quartzite: an SEM/EBSD analysis: *Journal of Structural Geology*, v. 22, no. 11-12, p. 1675-1693.
- Lloyd, G., Law, R., Mainprice, D., and Wheeler, J., 1992, Microstructural and crystal fabric evolution during shear zone formation: *Journal of Structural Geology*, v. 14, no. 8-9, p. 1079-1100.

- Lloyd, G. E., and Freeman, B., 1994, Dynamic recrystallization of quartz under greenschist conditions: *Journal of Structural Geology*, v. 16, no. 6, p. 867-881.
- Lu, R., He, D., Xu, X., and Liu, B. J. J. o. A. E. S., 2016, Crustal-scale tectonic wedging in the central Longmen Shan: Constraints on the uplift mechanism in the southeastern margin of the Tibetan Plateau, v. 117, p. 73-81.
- Luo, L., Qi, J.-F., Zhang, M.-Z., Wang, K., and Han, Y.-Z., 2014, Detrital zircon U–Pb ages of Late Triassic–Late Jurassic deposits in the western and northern Sichuan Basin margin: constraints on the foreland basin provenance and tectonic implications: *International Journal of Earth Sciences*, v. 103, p. 1553-1568.
- Lyons, J. B., and Snellenburg, J., 1971, Dating faults: *Geological Society of America Bulletin*, v. 82, no. 6, p. 1749-1752.
- Mainprice, D., Bouchez, J.-L., Blumenfeld, P., and Tubià, J. M., 1986, Dominant c slip in naturally deformed quartz: Implications for dramatic plastic softening at high temperature: *Geology*, v. 14, no. 10, p. 819-822.
- Mattauer, M., 1992, The Songpan Garze Triassic belt of west Sichuan and eastern Tibet: a decollement fold belt on a passive margin: *Tectonics*, v. 3, no. 14, p. 619-626.
- Meng, Q.-R., Wang, E., and Hu, J.-M., 2005, Mesozoic sedimentary evolution of the northwest Sichuan basin: Implication for continued clockwise rotation of the South China block: *Geological Society of America Bulletin*, v. 117, no. 3.
- Meng, Q., Hu, J., Wang, E., and Qu, H., 2006, Late Cenozoic denudation by large-magnitude landslides in the eastern edge of Tibetan Plateau: *Earth and Planetary Science Letters*, v. 243, no. 1-2, p. 252-267.
- Molnar, P., and England, P., 1990, Late Cenozoic uplift of mountain ranges and global climate change: chicken or egg?: *Nature*, v. 346, no. 6279, p. 29-34.
- Molnar, P., and Tapponnier, P., 1975, Cenozoic Tectonics of Asia: Effects of a Continental Collision: Features of recent continental tectonics in Asia can be interpreted as results of the India-Eurasia collision: *science*, v. 189, no. 4201, p. 419-426.
- Moore, D. M., and Reynolds Jr, R. C., 1989, *X-ray Diffraction and the Identification and Analysis of Clay Minerals*, Oxford University Press (OUP).
- Morgan, S. S., and Law, R. D., 2004, Unusual transition in quartzite dislocation creep regimes and crystal slip systems in the aureole of the Eureka Valley–Joshua Flat–Beer Creek pluton, California: a case for anhydrous conditions created by decarbonation reactions: *Tectonophysics*, v. 384, no. 1-4, p. 209-231.
- Mottram, C. M., Kellett, D. A., Barresi, T., Zwingmann, H., Friend, M., Todd, A., and Percival, J. B., 2020, Syncing fault rock clocks: Direct comparison of U-Pb carbonate and K-Ar illite fault dating methods: *Geology*, v. 48, no. 12, p. 1179-1183.
- Murphy, P. J., Briedis, J., and Peck, J. H., 1979, Dating techniques in fault investigations: *Geological Society of America, Reviews in Engineering Geology*, v. 4, p. 153-168.
- Nakamura, T., Tsuboi, S., Kaneda, Y., and Yamanaka, Y. 2010. Rupture process of the 2008 Wenchuan, China earthquake inferred from teleseismic waveform inversion and forward modeling of broadband seismic waves. *Tectonophysics*, 491(1-4), 72-84.

- Nelson, K. D., Zhao, W., Brown, L., Kuo, J., Che, J., Liu, X., Klemperer, S., Makovsky, Y., Meissner, R., and Mechie, J., 1996, Partially molten middle crust beneath southern Tibet: Synthesis of project INDEPTH results: *Science*, v. 274, no. 5293, p. 1684-1688.
- Neumann, B., 2000, Texture development of recrystallised quartz polycrystals unravelled by orientation and misorientation characteristics: *Journal of Structural Geology*, v. 22, no. 11-12, p. 1695-1711.
- Passchier, C. W., and Trouw, R. A., 2005, *Microtectonics*, Springer Science & Business Media.
- Pei, S., Su, J., Zhang, H., Sun, Y., Toksöz, M. N., Wang, Z., and He, J. 2010. Three-dimensional seismic velocity structure across the 2008 Wenchuan Ms 8.0 earthquake, Sichuan, China. *Tectonophysics*, 491(1-4), 211-217.
- Pei, X., Li, Z., Ding, S., Li, R., Feng, J., Sun, Y., Zhang, Y., and Liu, Z., 2009, Neoproterozoic Jiaoziding peraluminous granite in the northwestern margin of Yangtze Block: Zircon SHRIMP U-Pb age and geochemistry and their tectonic significance: *Earth Science Frontiers*, v. 16, no. 3, p. 231-249.
- Paternell, M., Hasalová, P., Wilson, C. J. L., Piazzolo, S., and Schulmann, K., 2010, Evaluating quartz crystallographic preferred orientations and the role of deformation partitioning using EBSD and fabric analyser techniques: *Journal of Structural Geology*, v. 32, no. 6, p. 803-817.
- Paternell, M., Russell-Head, D. S., and Wilson, C. J., 2011, A technique for recording polycrystalline structure and orientation during in situ deformation cycles of rock analogues using an automated fabric analyser: *J Microsc*, v. 242, no. 2, p. 181-188.
- Pevear, D. R., 1999, Illite and hydrocarbon exploration: *Proceedings of the National Academy of Sciences*, v. 96, no. 7, p. 3440-3446.
- Pitard, P., Replumaz, A., Chevalier, M. L., Leloup, P. H., Bai, M., Doin, M. P., Thieulot, C., Ou, X., Balvay, M., and Li, H., 2021, Exhumation history along the Muli thrust—Implication for crustal thickening mechanism in eastern Tibet: *Geophysical Research Letters*, v. 48, no. 14, p. e2021GL093677.
- Polissar, P. J., Freeman, K. H., Rowley, D. B., McInerney, F. A., and Currie, B. S., 2009, Paleoaltimetry of the Tibetan Plateau from D/H ratios of lipid biomarkers: *Earth and Planetary Science Letters*, v. 287, no. 1-2, p. 64-76.
- Popov, D. V., Spikings, R. A., Scaillet, S., O'Sullivan, G., Chew, D., Badenszki, E., Daly, J. S., Razakamanana, T., and Davies, J. H. F. L., 2020, Diffusion and fluid interaction in Itrongay pegmatite (Madagascar): Evidence from in situ $^{40}\text{Ar}/^{39}\text{Ar}$ dating of gem-quality alkali feldspar and U Pb dating of protogenetic apatite inclusions: *Chemical Geology*, v. 556.
- Qi, W., Xuejun, Q., Qigui, L., Freymueller, J., Shaomin, Y., Caijun, X., and Gang, C. 2011. Rupture of deep faults in the 2008 Wenchuan earthquake and uplift of the Longmen Shan. *Nature Geoscience*, 4(9), 634-640.
- Ran, Y.-K., Chen, W.-S., Xu, X.-W., Chen, L.-C., Wang, H., Yang, C.-C., and Dong, S.-P., 2013, Paleoseismic events and recurrence interval along the Beichuan–Yingxiu fault of Longmenshan fault zone, Yingxiu, Sichuan, China: *Tectonophysics*, v. 584, p. 81-90.

- Ran, Y., Chen, L., Chen, J., Wang, H., Chen, G., Yin, J., Shi, X., Li, C., and Xu, X., 2010, Paleoseismic evidence and repeat time of large earthquakes at three sites along the Longmenshan fault zone: *Tectonophysics*, v. 491, no. 1-4, p. 141-153.
- Ran, Y., Xu, X., Wang, H., Chen, W., Chen, L., Liang, M., Yang, H., Li, Y., and Liu, H., 2019, Evidence of Characteristic Earthquakes on Thrust Faults From Paleo-Rupture Behavior Along the Longmenshan Fault System: *Tectonics*, v. 38, no. 7, p. 2401-2410.
- Replumaz, A., Capitanio, F. A., Guillot, S., Negredo, A. M., and Villaseñor, A., 2014, The coupling of Indian subduction and Asian continental tectonics: *Gondwana Research*, v. 26, no. 2, p. 608-626.
- Replumaz, A., Negredo, A. M., Guillot, S., der Beek, P. v., and Villaseñor, A., 2010, Crustal mass budget and recycling during the India/Asia collision: *Tectonophysics*, v. 492, no. 1-4, p. 99-107.
- Robert, A., Zhu, J., Vergne, J., Cattin, R., Chan, L. S., Wittlinger, G., Herquel, G., de Sigoyer, J., Pubellier, M., and Zhu, L. D., 2010, Crustal structures in the area of the 2008 Sichuan earthquake from seismologic and gravimetric data: *Tectonophysics*, v. 491, no. 1-4, p. 205-210.
- Roger, F., Malavieille, J., Leloup, P. H., Calassou, S., and Xu, Z., 2004, Timing of granite emplacement and cooling in the Songpan–Garzê Fold Belt (eastern Tibetan Plateau) with tectonic implications: *Journal of Asian Earth Sciences*, v. 22, no. 5, p. 465-481.
- Rolland, Y., Alexeiev, D. V., Kröner, A., Corsini, M., Loury, C., and Monié, P., 2013, Late Palaeozoic to Mesozoic kinematic history of the Talas–Ferghana strike-slip fault (Kyrgyz West Tianshan) as revealed by $^{40}\text{Ar}/^{39}\text{Ar}$ dating of syn-kinematic white mica: *Journal of Asian Earth Sciences*, v. 67, p. 76-92.
- Rolland, Y., Cox, S. F., and Corsini, M., 2009, Constraining deformation stages in brittle–ductile shear zones from combined field mapping and $^{40}\text{Ar}/^{39}\text{Ar}$ dating: the structural evolution of the Grimsel Pass area (Aar Massif, Swiss Alps): *Journal of Structural Geology*, v. 31, no. 11, p. 1377-1394.
- Royden, L. H., Burchfiel, B. C., King, R. W., Wang, E., Chen, Z., Shen, F., and Liu, Y., 1997, Surface deformation and lower crustal flow in eastern Tibet: *Science*, v. 276, no. 5313, p. 788-790.
- Royden, L. H., Burchfiel, B. C., and van der Hilst, R. D., 2008, The geological evolution of the Tibetan Plateau: *Science*, v. 321, no. 5892, p. 1054-1058.
- Russell-Head, D., and Wilson, C., Automated fabric analyser system for quartz and ice, *in* Proceedings Geological Society of Australia Abstracts 2001, Volume 64, Geological Society of Australia; 1999, p. 159-159.
- Sanchez, G., Rolland, Y., Schneider, J., Corsini, M., Oliot, E., Goncalves, P., Verati, C., Lardeaux, J.-M., and Marquer, D., 2011, Dating low-temperature deformation by $^{40}\text{Ar}/^{39}\text{Ar}$ on white mica, insights from the Argentera-Mercantour Massif (SW Alps): *Lithos*, v. 125, no. 1-2, p. 521-536.
- SBGMR, 1991, Sichuan Bureau of Geology and Mineral Resources, Regional Geology of Sichuan Province, Beijing: Geology House, 728 p.:

- Scaillet, S., Feraud, G., Balleuvre, M., and Amouric, M., 1992, MgFe and [(Mg, Fe) Si-Al₂] compositional control on argon behaviour in high-pressure white micas: A ⁴⁰Ar/³⁹Ar continuous laser-probe study from the Dora-Maira nappe of the internal western Alps, Italy: *Geochimica et Cosmochimica Acta*, v. 56, no. 7, p. 2851-2872.
- Scharf, A., Handy, M. R., Schmid, S. M., Favaro, S., Sudo, M., Schuster, R., and Hammerschmidt, K. J. T., 2016, Grain-size effects on the closure temperature of white mica in a crustal-scale extensional shear zone—Implications of in-situ ⁴⁰Ar/³⁹Ar laser-ablation of white mica for dating shearing and cooling (Tauern Window, Eastern Alps): *tectonophysics*, v. 674, p. 210-226.
- Schneider, S., Hammerschmidt, K., and Rosenberg, C. L., 2013, Dating the longevity of ductile shear zones: Insight from ⁴⁰Ar/³⁹Ar in situ analyses: *Earth and Planetary Science Letters*, v. 369, p. 43-58.
- Searle, M. P., and Szulc, A. G., 2005, Channel flow and ductile extrusion of the high Himalayan slab—the Kangchenjunga–Darjeeling profile, Sikkim Himalaya☆: *Journal of Asian Earth Sciences*, v. 25, no. 1, p. 173-185.
- Shen, X., Tian, Y., Zhang, G., Zhang, S., Carter, A., Kohn, B., Vermeesch, P., Liu, R., and Li, W., 2019, Late Miocene Hinterland Crustal Shortening in the Longmen Shan Thrust Belt, the Eastern Margin of the Tibetan Plateau: *Journal of Geophysical Research: Solid Earth*, v. 124, no. 11, p. 11972-11991.
- Shen, Z.-K., Sun, J., Zhang, P., Wan, Y., Wang, M., Bürgmann, R., Zeng, Y., Gan, W., Liao, H., and Wang, Q., 2009, Slip maxima at fault junctions and rupturing of barriers during the 2008 Wenchuan earthquake: *Nature geoscience*, v. 2, no. 10, p. 718-724.
- Sibson, R. H., 1977, Fault rocks and fault mechanisms: *Journal of the Geological Society*, v. 133, no. 3, p. 191-213.
- Solum, J. G., van der Pluijm, B. A., and Peacor, D. R., 2005, Neocrystallization, fabrics and age of clay minerals from an exposure of the Moab Fault, Utah: *Journal of Structural Geology*, v. 27, no. 9, p. 1563-1576.
- Stipp, M., Stübenitz, H., Heilbronner, R., and Schmid, S. M., 2002, The eastern Tonale fault zone: a ‘natural laboratory’ for crystal plastic deformation of quartz over a temperature range from 250 to 700 C: *Journal of structural geology*, v. 24, no. 12, p. 1861-1884.
- Stöckhert, B., Brix, M. R., Kleinschrodt, R., Hurford, A. J., and Wirth, R., 1999, Thermochronometry and microstructures of quartz—a comparison with experimental flow laws and predictions on the temperature of the brittle–plastic transition: *Journal of Structural Geology*, v. 21, no. 3, p. 351-369.
- Tan, X., Liu, Y., Lee, Y.-H., Lu, R., Xu, X., Suppe, J., Shi, F., and Xu, C., 2019, Parallelism between the maximum exhumation belt and the Moho ramp along the eastern Tibetan Plateau margin: Coincidence or consequence?: *Earth and Planetary Science Letters*, v. 507, p. 73-84.
- Tan, X., Xu, X.-W., Lee, Y.-H., Lu, R.-Q., Liu, Y., Xu, C., Li, K., Yu, G.-H., and Kang, W.-J., 2017, Late Cenozoic thrusting of major faults along the central segment of Longmen Shan,

- eastern Tibet: Evidence from low-temperature thermochronology: *Tectonophysics*, v. 712-713, p. 145-155.
- Tan, X., Yue, H., Liu, Y., Xu, X., Shi, F., Xu, C., Ren, Z., Shyu, J. B. H., Lu, R., and Hao, H., 2018, Topographic Loads Modified by Fluvial Incision Impact Fault Activity in the Longmenshan Thrust Belt, Eastern Margin of the Tibetan Plateau: *Tectonics*, v. 37, no. 9, p. 3001-3017.
- Tapponnier, P., Peltzer, G., and Armijo, R., 1986, On the mechanics of the collision between India and Asia: Geological Society, London, Special Publications, v. 19, no. 1, p. 113-157.
- Tapponnier, P., Zhiqin, X., Roger, F. o., Meyer, B., and Arnaud, N., 2001, Oblique Stepwise Rise and Growth of the Tibet Plateau: *Science*, v. 294, no. 5547, p. 1671-1677.
- Tian, Y., Kohn, B. P., Gleadow, A. J. W., and Hu, S., 2013, Constructing the Longmen Shan eastern Tibetan Plateau margin: Insights from low-temperature thermochronology: *Tectonics*, v. 32, no. 3, p. 576-592.
- Tian, Y., Kohn, B. P., Phillips, D., Hu, S., Gleadow, A. J. W., and Carter, A., 2016, Late Cretaceous-earliest Paleogene deformation in the Longmen Shan fold-and-thrust belt, eastern Tibetan Plateau margin: Pre-Cenozoic thickened crust?: *Tectonics*, v. 35, no. 10, p. 2293-2312.
- Tian, Y., Li, R., Tang, Y., Xu, X., Wang, Y., and Zhang, P., 2018, Thermochronological Constraints on the Late Cenozoic Morphotectonic Evolution of the Min Shan, the Eastern Margin of the Tibetan Plateau: *Tectonics*, v. 37, no. 6, p. 1733-1749.
- Torgersen, E., Viola, G., Zwingmann, H., and Harris, C., 2015, Structural and temporal evolution of a reactivated brittle–ductile fault – Part II: Timing of fault initiation and reactivation by K–Ar dating of synkinematic illite/muscovite: *Earth and Planetary Science Letters*, v. 410.
- Tu, X., Dai, F., and Pan, Y., 2012, Dating of faults and estimation of surface uplift and erosion rates in the northern margin of Dabie Mountains, China: *Journal of Asian Earth Sciences*, v. 56, p. 72-76.
- van der Beek, P., Van Melle, J., Guillot, S., Pêcher, A., Reiners, P. W., Nicolescu, S., and Latif, M., 2009, Eocene Tibetan plateau remnants preserved in the northwest Himalaya: *Nature Geoscience*, v. 2, no. 5, p. 364-368.
- Velde, B., 1965, Phengite micas; synthesis, stability, and natural occurrence: *American Journal of Science*, v. 263, no. 10, p. 886-913.
- Villa, 1998, Isotopic closure: *terra Nova*, v. 10, no. 1, p. 42-47.
- Villa, I. M., 2022, Dating deformation: the role of atomic-scale processes: *Journal of the Geological Society*.
- Viola, G., Zwingmann, H., Mattila, J., and Käpyaho, A., 2013, K-Ar illite age constraints on the Proterozoic formation and reactivation history of a brittle fault in Fennoscandia: *Terra Nova*, v. 25, no. 3, p. 236-244.
- Vrolijk, P., Pevear, D., Covey, M., and LaRiviere, A., 2018, Fault gouge dating: history and evolution: *Clay Minerals*, v. 53, no. 3, p. 305-324.

- Wang, C., Wu, J., Lou, H., Zhou, M., and Bai, Z. 2003. P-wave crustal velocity structure in western Sichuan and eastern Tibetan region. *Science in China Series D: Earth Sciences*, 46, 254-265.
- Wang, E., Kirby, E., Furlong, K. P., van Soest, M., Xu, G., Shi, X., Kamp, P. J. J., and Hodges, K. V., 2012, Two-phase growth of high topography in eastern Tibet during the Cenozoic: *Nature Geoscience*, v. 5, no. 9, p. 640-645.
- Wang, E., Meng, K., Su, Z., Meng, Q., Chu, J. J., Chen, Z., Wang, G., Shi, X., and Liang, X., 2014a, Block rotation: Tectonic response of the Sichuan basin to the southeastward growth of the Tibetan Plateau along the Xianshuihe-Xiaojiang fault: *Tectonics*, v. 33, no. 5, p. 686-718.
- Wang, H., Li, H., Si, J., Sun, Z., and Huang, Y., 2014b, Internal structure of the Wenchuan earthquake fault zone, revealed by surface outcrop and WFSD-1 drilling core investigation: *Tectonophysics*, v. 619-620, p. 101-114.
- Wang, H., Li, H. B., Zhang, L., Zheng, Y., Si, J. L., and Sun, Z. M., 2019, Paleoseismic Slip Records and Uplift of the Longmen Shan, Eastern Tibetan Plateau: *Tectonics*, v. 38, no. 1, p. 354-373.
- Wang, M., and Shen, Z. K., 2020, Present-Day Crustal Deformation of Continental China Derived From GPS and Its Tectonic Implications: *Journal of Geophysical Research: Solid Earth*, v. 125, no. 2.
- Wang, Z., Wang, J., Chen, Z., Liu, Y., Huang, R., Pei, S., and Tang, W. 2011. Seismic imaging, crustal stress and GPS data analyses: Implications for the generation of the 2008 Wenchuan Earthquake (M7. 9), China. *Gondwana Research*, 19(1), 202-212.
- Weislogel, A., Graham, S., Chang, E., Wooden, J., and Gehrels, G., 2010, Detrital zircon provenance from three turbidite depocenters of the Middle–Upper Triassic Songpan-Ganzi complex, central China: Record of collisional tectonics, erosional exhumation, and sediment production: *Geological Society of America Bulletin*, v. 122, no. 11-12, p. 2041-2062.
- Weislogel, A. L., Graham, S. A., Chang, E. Z., Wooden, J. L., Gehrels, G. E., and Yang, H., 2006, Detrital zircon provenance of the Late Triassic Songpan-Ganzi complex: Sedimentary record of collision of the North and South China blocks: *Geology*, v. 34, no. 2, p. 97-100.
- West Jr, D. P., and Hubbard, M. S., 1997, Progressive localization of deformation during exhumation of a major strike-slip shear zone: Norumbega fault zone, south-central Maine, USA: *Tectonophysics*, v. 273, no. 3-4, p. 185-201.
- Worley, B. A., and Wilson, C. J., 1996, Deformation partitioning and foliation reactivation during transpressional orogenesis, an example from the Central Longmen Shan, China: *Journal of Structural Geology*, v. 18, no. 4, p. 395-411.
- Wu, C., Li, H., Leloup, P. H., Yu, C., Si, J., Liu, D., Pan, J., Chevalier, M.-L., and Gong, Z., 2014, High-angle fault responsible for the surface ruptures along the northern segment of the Wenchuan Earthquake Fault Zone: Evidence from the latest seismic reflection profiles: *Tectonophysics*, v. 619, p. 159-170.

- Xiao, L., Zhang, H.-F., Ni, P.-Z., Xiang, H., and Liu, X.-M., 2007a, LA-ICP-MS U–Pb zircon geochronology of early Neoproterozoic mafic-intermediate intrusions from NW margin of the Yangtze Block, South China: Implication for tectonic evolution: *Precambrian Research*, v. 154, no. 3-4, p. 221-235.
- Xiao, L., Zhang, H., Clemens, J., Wang, Q., Kan, Z., Wang, K., Ni, P., and Liu, X., 2007b, Late Triassic granitoids of the eastern margin of the Tibetan Plateau: Geochronology, petrogenesis and implications for tectonic evolution: *Lithos*, v. 96, no. 3-4, p. 436-452.
- Xu, Z., Liwei, H., Zongxiu, W., Xiaofang, F., and Minghua, H. 1992. The Evolution of Songpan-Ganzi Orogenic Belt in China.
- Xu, Z., Ji, S., Li, H., Hou, L., Fu, X., and Cai, Z., 2008, Uplift of the Longmen Shan range and the Wenchuan earthquake: *Episodes*, v. 31.
- Xue, Z., Lin, W., Chu, Y., Faure, M., Chen, Y., Ji, W., and Qiu, H., 2021, An intracontinental orogen exhumed by basement-slice imbrication in the Longmenshan Thrust Belt of the Eastern Tibetan Plateau: *GSA Bulletin*.
- Xue, Z., Martelet, G., Lin, W., Faure, M., Chen, Y., Wei, W., Li, S., and Wang, Q., 2017, Mesozoic Crustal Thickening of the Longmenshan Belt (NE Tibet, China) by Imbrication of Basement Slices: Insights From Structural Analysis, Petrofabric and Magnetic Fabric Studies, and Gravity Modeling: *Tectonics*, v. 36, no. 12, p. 3110-3134.
- Xypolias, P., 2010, Vorticity analysis in shear zones: A review of methods and applications: *Journal of Structural Geology*, v. 32, no. 12, p. 2072-2092.
- Yan, D.-P., Qiu, L., Wells, M. L., Zhou, M.-F., Meng, X., Lu, S., Zhang, S., Wang, Y., and Li, S.-B., 2018, Structural and Geochronological Constraints on the Early Mesozoic North Longmen Shan Thrust Belt: Foreland Fold-Thrust Propagation of the SW Qinling Orogenic Belt, Northeastern Tibetan Plateau: *Tectonics*, v. 37, no. 12, p. 4595-4624.
- Yan, D.-P., Zhou, M.-F., Li, S.-B., and Wei, G.-Q., 2011, Structural and geochronological constraints on the Mesozoic-Cenozoic tectonic evolution of the Longmen Shan thrust belt, eastern Tibetan Plateau: *Tectonics*, v. 30, no. 6, p. n/a-n/a.
- Yan, D.-P., Zhou, M.-F., Song, H.-L., Wang, X.-W., and Malpas, J., 2003a, Origin and tectonic significance of a Mesozoic multi-layer over-thrust system within the Yangtze Block (South China): *Tectonophysics*, v. 361, no. 3-4, p. 239-254.
- Yan, D.-P., Zhou, M.-F., Song, H., and Fu, Z., 2003b, Structural style and tectonic significance of the Jianglang dome in the eastern margin of the Tibetan Plateau, China: *Journal of Structural Geology*, v. 25, no. 5, p. 765-779.
- Yan, D., Zhou, M., Wei, G., Gao, J., Liu, S., Xu, P., and Shi, X., 2008a, The Pengguan tectonic dome of Longmen Mountains, Sichuan Province: Mesozoic denudation of a Neoproterozoic magmatic arc-basin system: *Science in China Series D: Earth Sciences*, v. 51, no. 11, p. 1545-1559.
- Yan, D., Zhou, M., Wei, G., Liu, H., Dong, T., Zhang, W., and Jin, Z., 2008b, Collapse of Songpan-Garzê Orogenic Belt Resulted from Mesozoic Middle-crustal Ductile Channel Flow: Evidences from Deformation and Metamorphism Within Sinian-Paleozoic Strata in

- Hinterland of Longmenshan Foreland Thrust Belt: *Earth Science Frontiers*, v. 15, no. 3, p. 186-198.
- Yan, J., Zhang, T., Liu, J., Chen, X., Chen, W., and Dao, H. N., 2021, Lateral subhorizontal middle to lower crustal flow in response to continental collision: Evidence from the Diancang Shan complex along the Ailao Shan-Red River belt, Southeastern Tibetan Plateau: *Journal of Structural Geology*, v. 143.
- Yao, H., van der Hilst, R. D., and de Hoop, M. V., 2006, Surface-wave array tomography in SE Tibet from ambient seismic noise and two-station analysis - I. Phase velocity maps: *Geophysical Journal International*, v. 166, no. 2, p. 732-744.
- Yin, A., and Nie, S., 1993, An indentation model for the North and South China collision and the development of the Tan-Lu and Honam fault systems, eastern Asia: *Tectonics*, v. 12, no. 4, p. 801-813.
- Yoder, H. S., and Eugster, H., 1955, Synthetic and natural muscovites: *Geochimica et Cosmochimica Acta*, v. 8, no. 5-6, p. 225-280.
- Yu, G., Xu, X., Klinger, Y., Diao, G., Chen, G., Feng, X., and An, Y. 2010. Fault-scarp features and cascading-rupture model for the M w 7.9 Wenchuan earthquake, eastern Tibetan plateau, China. *Bulletin of the seismological Society of America*, 100(5B), 2590-2614.
- Yuan, C., Zhou, M.-F., Sun, M., Zhao, Y., Wilde, S., Long, X., and Yan, D., 2010, Triassic granitoids in the eastern Songpan Ganzi Fold Belt, SW China: Magmatic response to geodynamics of the deep lithosphere: *Earth Planetary Science Letters*, v. 290, no. 3-4, p. 481-492.
- Zhang, H.-F., Parrish, R., Zhang, L., Xu, W.-C., Yuan, H.-L., Gao, S., and Crowley, Q. G., 2007, A-type granite and adakitic magmatism association in Songpan–Garze fold belt, eastern Tibetan Plateau: implication for lithospheric delamination: *Lithos*, v. 97, no. 3-4, p. 323-335.
- Zhang, H.-F., Zhang, L., Harris, N., Jin, L.-L., and Yuan, H., 2006, U–Pb zircon ages, geochemical and isotopic compositions of granitoids in Songpan-Garze fold belt, eastern Tibetan Plateau: constraints on petrogenesis and tectonic evolution of the basement: *Contributions to Mineralogy and Petrology*, v. 152, p. 75-88.
- Zhang, K.-J., Li, B., Wei, Q.-G., Cai, J.-X., and Zhang, Y.-X., 2008, Proximal provenance of the western Songpan–Ganzi turbidite complex (Late Triassic, eastern Tibetan plateau): Implications for the tectonic amalgamation of China: *Sedimentary Geology*, v. 208, no. 1-2, p. 36-44.
- Zhang, P.-Z., 2013, A review on active tectonics and deep crustal processes of the Western Sichuan region, eastern margin of the Tibetan Plateau: *Tectonophysics*, v. 584, p. 7-22.
- Zhang, P.-Z., Shen, Z., Wang, M., Gan, W., Bürgmann, R., Molnar, P., Wang, Q., Niu, Z., Sun, J., Wu, J., Hanrong, S., and Xinzhao, Y., 2004, Continuous deformation of the Tibetan Plateau from global positioning system data: *Geology*, v. 32, no. 9.
- Zhang, Y., Jia, D., Shen, L., Yin, H., Chen, Z., Li, H., Li, Z., and Sun, C., 2015, Provenance of detrital zircons in the Late Triassic Sichuan foreland basin: constraints on the evolution of

the Qinling Orogen and Longmen Shan thrust-fold belt in central China: *International Geology Review*, v. 57, no. 14, p. 1806-1824.

- Zhao, G., Unsworth, M. J., Zhan, Y., Wang, L., Chen, X., Jones, A. G., Tang, J., Xiao, Q., Wang, J., Cai, J., Li, T., Wang, Y., and Zhang, J., 2012, Crustal structure and rheology of the Longmenshan and Wenchuan Mw 7.9 earthquake epicentral area from magnetotelluric data: *Geology*, v. 40, no. 12, p. 1139-1142.
- Zhao, J.-H., and Zhou, M.-F., 2007, Neoproterozoic adakitic plutons and arc magmatism along the western margin of the Yangtze Block, South China: *The Journal of Geology*, v. 115, no. 6, p. 675-689.
- Zheng, Y., Kong, P., and Fu, B., 2014, Time constraints on the emplacement of klippen in the Longmen Shan thrust belt and tectonic implications: *Tectonophysics*, v. 634, p. 44-54.
- Zheng, Y., Li, H., Sun, Z., Wang, H., Zhang, J., Li, C., and Cao, Y., 2016, New geochronology constraints on timing and depth of the ancient earthquakes along the Longmen Shan fault belt, eastern Tibet: *Tectonics*, v. 35, no. 12, p. 2781-2806.
- Zhou, M.-F., Kennedy, A. K., Sun, M., Malpas, J., and Leshner, C. M., 2002, Neoproterozoic arc-related mafic intrusions along the northern margin of South China: implications for the accretion of Rodinia: *The Journal of geology*, v. 110, no. 5, p. 611-618.
- Zhou, M.-F., Yan, D.-P., Wang, C.-L., Qi, L., and Kennedy, A., 2006, Subduction-related origin of the 750 Ma Xuelongbao adakitic complex (Sichuan Province, China): Implications for the tectonic setting of the giant Neoproterozoic magmatic event in South China: *Earth and Planetary Science Letters*, v. 248, no. 1-2, p. 286-300.

Appendix

S1 River network evolution around the Wenchuan-Maoxian (WM) fault

Here, we discuss the possibility that the ~25 km offset reconstruction along the Wenchuan-Maoxian fault, in addition to the clear Zagunao-Minjiang (#7-7'' in Fig. 1a) and Caoba-Yuzixi (#6-6'), also realigns other, less prominent rivers.

Smaller rivers across the southeast part of the WM fault zone are also realigned with a 25 km right-lateral offset (#1-1'', #2-2'', #3-3'' in Fig. 1c and #4-4'', #5-5'' in Fig. S1-1a).

However, the 25 km offset brings the present-day upper reach of the major Minjiang flowing to southwest (#10 in Fig. S1-1a, b and S1-2) in front of a river flowing northwest (#10' in Fig. S1-1c and S1-2) is puzzling. This may be explained considering that the Pengguan was exhumed by ~8 km since ~30 Ma (Furlong et al., 2021), and that most rivers, unlike the Minjiang, may have been dammed by the fast-rising Pengguan range. In that case rivers flowing southwest may have reversed their flow to northwest on the ~9 km wide NW flank of the Pengguan, while they would have kept southeast flow on the SE flank. Indeed, northwest-flowing rivers on the NW flank of the Pengguan systematically have southeast flowing counterparts right across the crest (#8' and 8'', #9' and 9'', #10' and 10'', #11' and 11'', #12' and 12'', #13' and 13'' in Fig. S1-1b and S1-2). Further, the now northwest flowing rivers have systematically an upstream counterpart with the 25 km offset (#8' and 8, #9' and 9, #10' and 10 in Fig. S1b and S2; and #11' and 11, #12' and 12, #13' and 13 in Fig. S1d and S2). The upper Minjiang river (#10) is significantly larger than the other ones, and its counterpart, the Qianjiang river (#10'') is also significantly larger than the surrounding rivers (Fig. 3a, S1-1a).

Assuming that a fast uplift of the Pengguan have dammed one large and 5 minor rivers allows a ~25 km right-lateral offset to yield a consistent river network all along the WM fault, bringing 13 rivers in front of their counterparts.

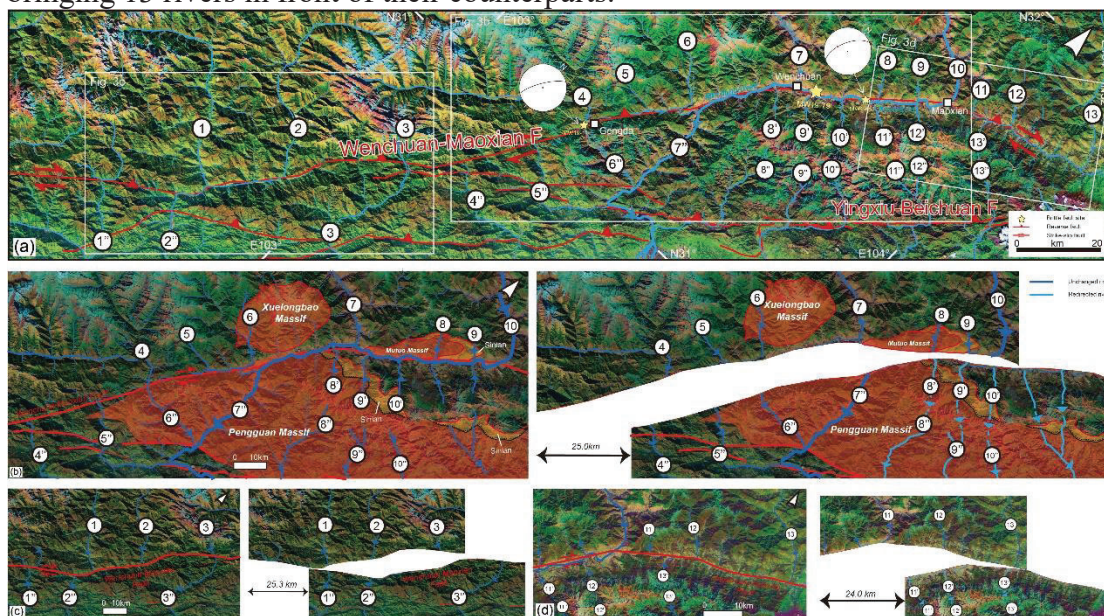


Fig. S1-1 River network evolution around the WM fault. (a) Landsat 8 image with major river channels and brittle faults. River data are referenced and modified from GloRic dataset and Sichuan water system map (SPWRD 2017; Dallaire et al. 2019). Faults from Li et al., 2011 and personal mapping. Stars indicate brittle fault sites – see text for details. Main rivers channels are numbered sequentially from SW to NE. b), c) and d) zooms on parts of the fault

zone (left) with corresponding reconstitution prior to right-lateral faulting (right) assuming 25 km of right lateral offset in the N50° direction along the WM fault. On b) granitic basement is shown in red and overlying Sinian unit in orange. Note that black arrows and dash lines on the reconstructions indicate river flow inversion and lost connections since uplift of the Pengguan range. See text for details.

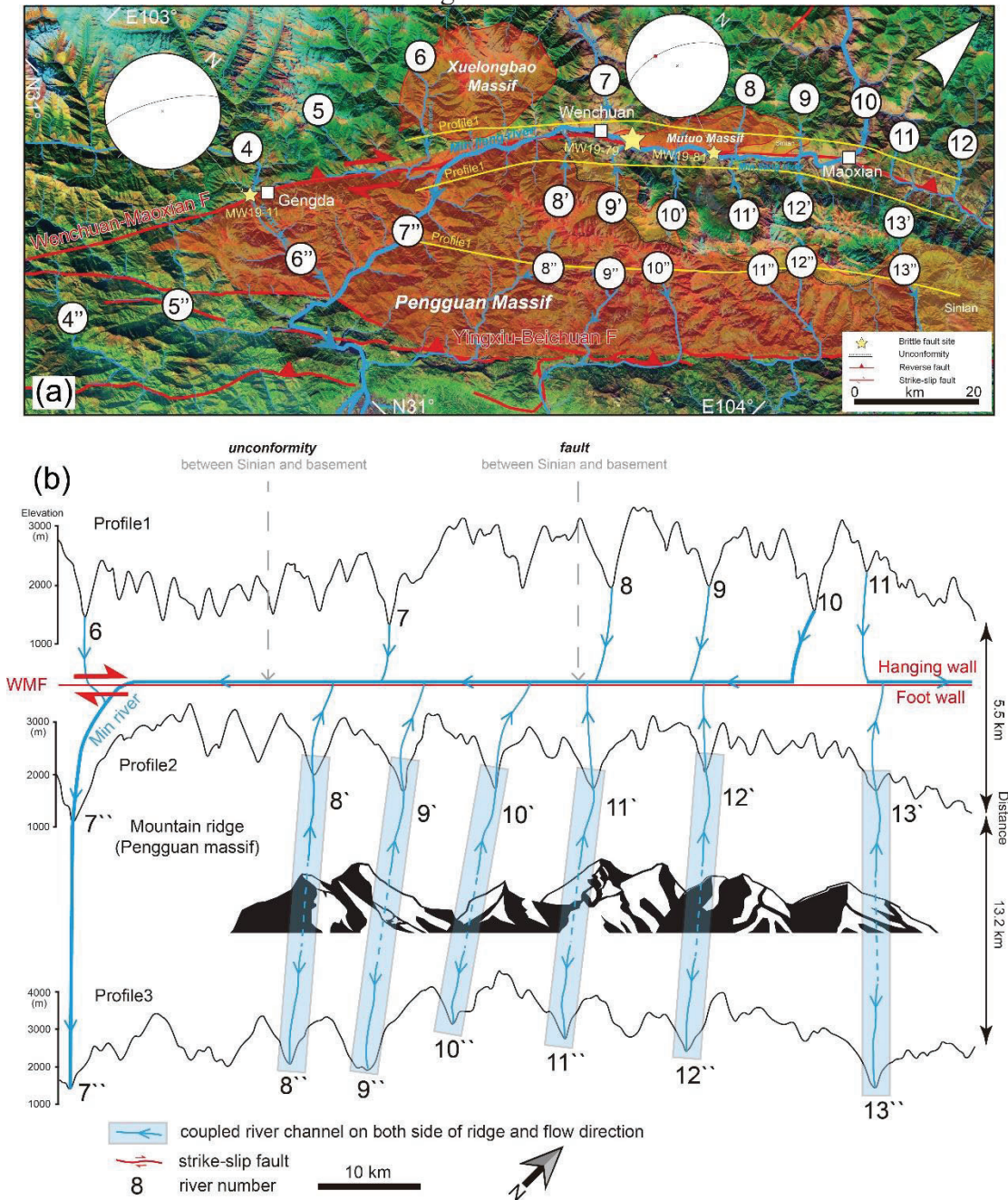


Fig.

S1-2 River network and river channel profiles around the WM fault. a) Map view of central part of WM fault with river network. b) three topography profiles along the WM fault showing the small river valleys on the SE Flank of the Pengguan (8''-13'') that are in front the valleys across the Pengguan ridge (8' - 13'), themselves offset by 25 km from rivers across the WM fault (8-13).

S2 Results Illite dating MW19-79A and MW19-79E

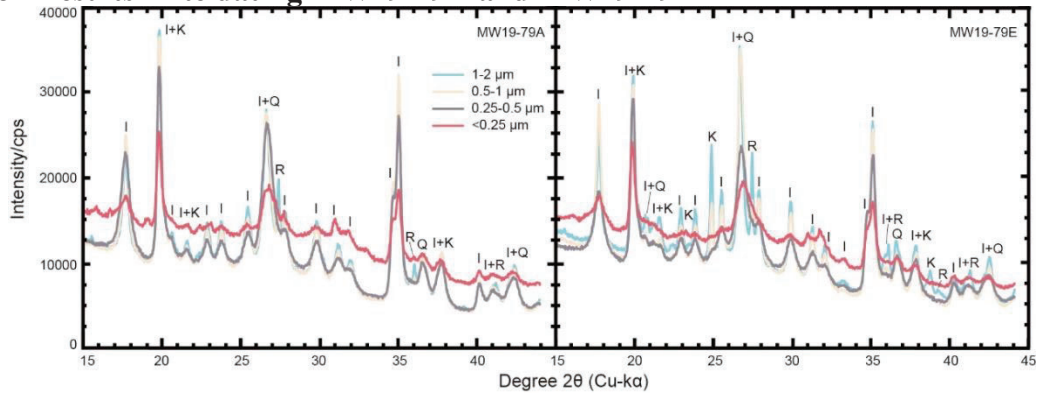


Fig. S2-1 X-ray diffractograms of random-mounted illite fractions of various sizes. Abbreviation: I: illite 2M1; K: kaolinite; Q: quartz; R: rutile

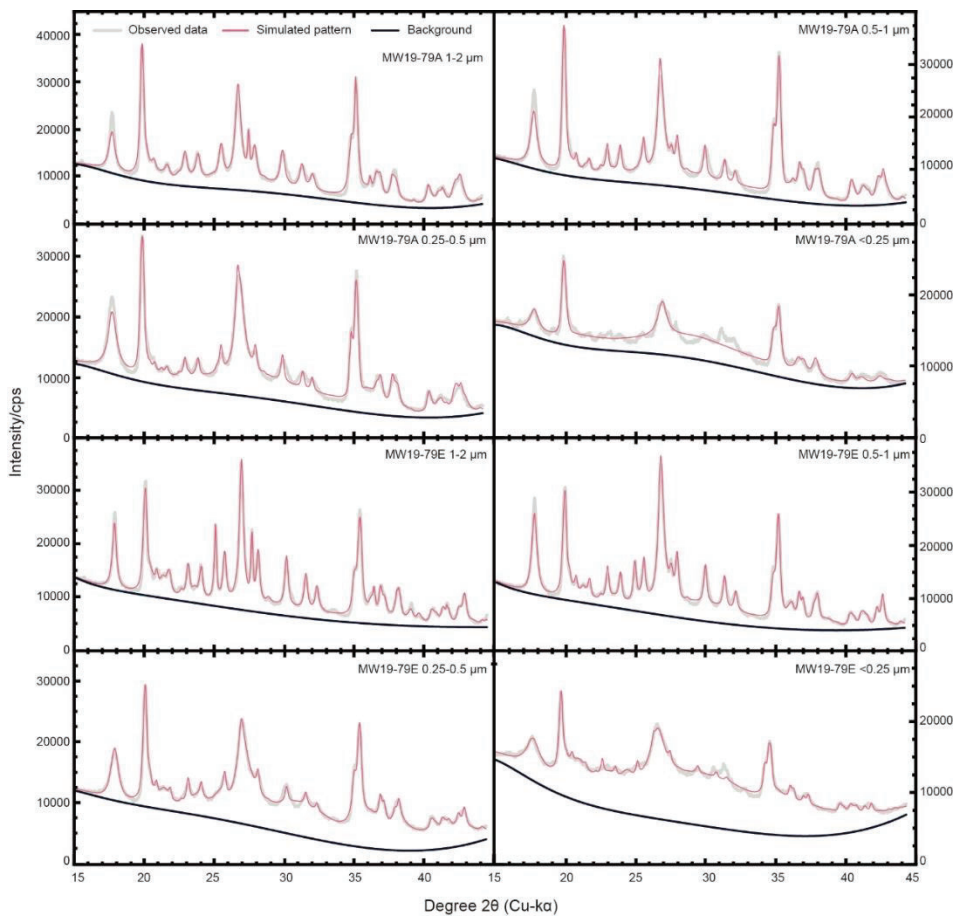


Fig. S2-2 Comparison of integrating curves of best-fitting mineral compositions obtained with the Profex software with the experimental X-ray diffractograms of random-mounted illite fractions of various sizes

Table S2-1 Best-fitting mineral compositions for the unoriented slides using PROFEX software

Sample	Clay size(um)	2M ₁ illite (%)	1M _d illite (%)	Anatase (%)	Kaolinite (%)	Rutile (%)	2M ₁ illite Percent (%)
MW19-79A	2-1	50.4±1.7	42.8±1.5		4.84±0.76	2±0.11	54.08±3.84
	1-0.5	29.65±0.77	67.38±0.79		1.44±0.28	1.53±0.2	30.56±3.02
	0.5-0.25	16.24±0.46	80.03±0.84		1.32±0.33	2.42±0.61	16.87±2.92
	<0.25		81.597		18.403		0±2.73
MW19-79E	2-1	44.5±1.3	41.9±1.6	2.08±0.08	8.57±0.49	2.92±0.12	51.5±3.7
	1-0.5	32.1±9.2	59±12	1.38±0.39	5.2±1.4	2.17±0.66	35.24±8.73
	0.5-0.25	6.95±0.8	88.5±1.3		1.88±0.22	2.64±0.29	7.28±3.32
	<0.25	5.28±0.68	88.4±1.5		6.3±0.89		5.64±3.4

Table S2-2 K–Ar ages of the four size fractions of illite isolated from the fault gouge samples MW19-79A and MW19-79E

Sample	Clay size (um)	K cont. (%)	(⁴⁰ Ar/ ³⁸ Ar) m	(³⁸ Ar/ ³⁶ Ar) m	Radiogenic ⁴⁰ Ar (mol/g)	⁴⁰ K (mol/g)	Age (Ma, 1σ)
MW19-79A	2-1	7.89	1.03	1051.71	2.35E-10	1.89E-07	21.2±0.2
	1-0.5	8.57	1.02	896.32	1.94E-10	2.05E-07	16.2±0.1
	0.5-0.25	8.31	1.05	745.62	1.19E-10	1.99E-07	10.3±0.2
	<0.25	3.92	0.82	496.04	3.81E-11	9.39E-08	6.9±0.1
MW19-79E	2-1	6.84	2.02	1053.16	5.83E-10	1.64E-07	60.2±0.5
	1-0.5	7.33	2.04	909.27	4.16E-10	1.76E-07	40.3±0.5
	0.5-0.25	6.79	1.66	560.64	1.91E-10	1.63E-07	20.1±0.2
	<0.25	4.07	1.15	363.45	5.48E-11	9.76E-08	9.6±0.1

Table S2-3 percentage of inherited (2M1) illite and corresponding K-Ar ages in Myr for the four different grain sizes of two fault gouge samples MW19-79A and MW19-79E

Sample	Clay size(um)	Inherited illite (%)	K-Ar Age (Ma)
MW19-79A	2-1	54.08±3.84	21.2±0.2
	1-0.5	30.56±3.02	16.2±0.1
	0.5-0.25	16.87±2.92	10.3±0.2
	<0.25	0±2.73	6.9±0.1
MW19-79E	2-1	51.5±3.7	60.2±0.5
	1-0.5	35.24±8.73	40.3±0.5
	0.5-0.25	7.28±3.32	20.1±0.2
	<0.25	5.64±3.4	9.6±0.1

S3 Analytical procedure for Ar-Ar dating

The detailed procedure of in-situ and step-heating $^{40}\text{Ar}/^{39}\text{Ar}$ dating can be seen in Beaudoin et al. (2020). The main experimental procedures and apparatus settings are the same, some minor modifications are as follows:

1, For step-heating $^{40}\text{Ar}/^{39}\text{Ar}$ dating, hand samples were crushed and sieved for fragments below 100 μm , then magnetically and gravimetrically sorted to obtain a purer white mica aggregate. After very careful inspection under a binocular microscope to remove any adhering phase/contaminant, these were cleaned through three successive ultrasonic baths (acetone, ethanol, and pure water), each one followed by drying in a 50 °C stove, before final optical inspection and weighing.

2, For the in-situ analyses, according to the size of the white mica belt, two spot sizes of 50 μm and 100 μm were applied to ensure a sufficient signal strength.

S4 Sample MW19-38A in situ dating

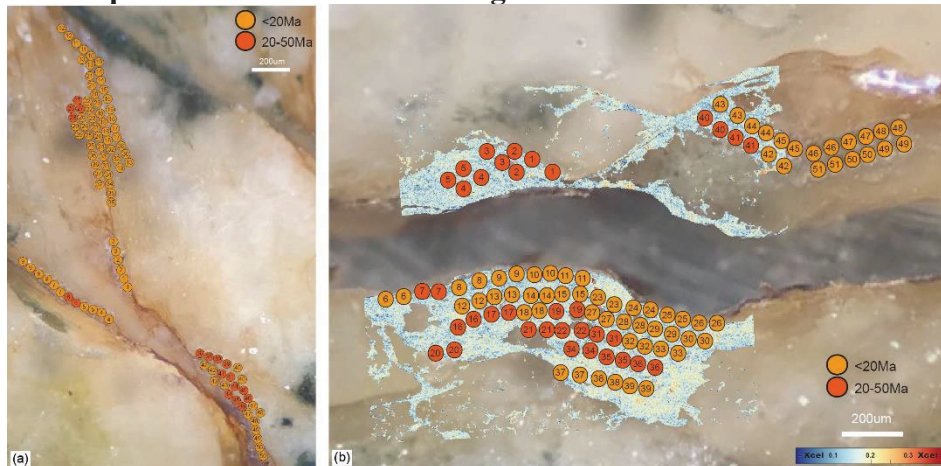


Fig. S4-1 In-situ laser points location map. a) zone N393 with circled numbers corresponding to spot numbers and circle colors to age range. b): zone N390 with colors corresponding to Xcel composition where available, circled numbers correspond to spot numbers and circle colors to age range.

Table S4-1 excel file for in-situ $^{40}\text{Ar}/^{39}\text{Ar}$ isotopic data

S5 Sample MW19-38A step heating dating

Include two runs: N407 (run1) and N399 (run2), see Table S5-1 excel file for $^{40}\text{Ar}/^{39}\text{Ar}$ isotopic data

S6 Sample MW19-10B in situ dating

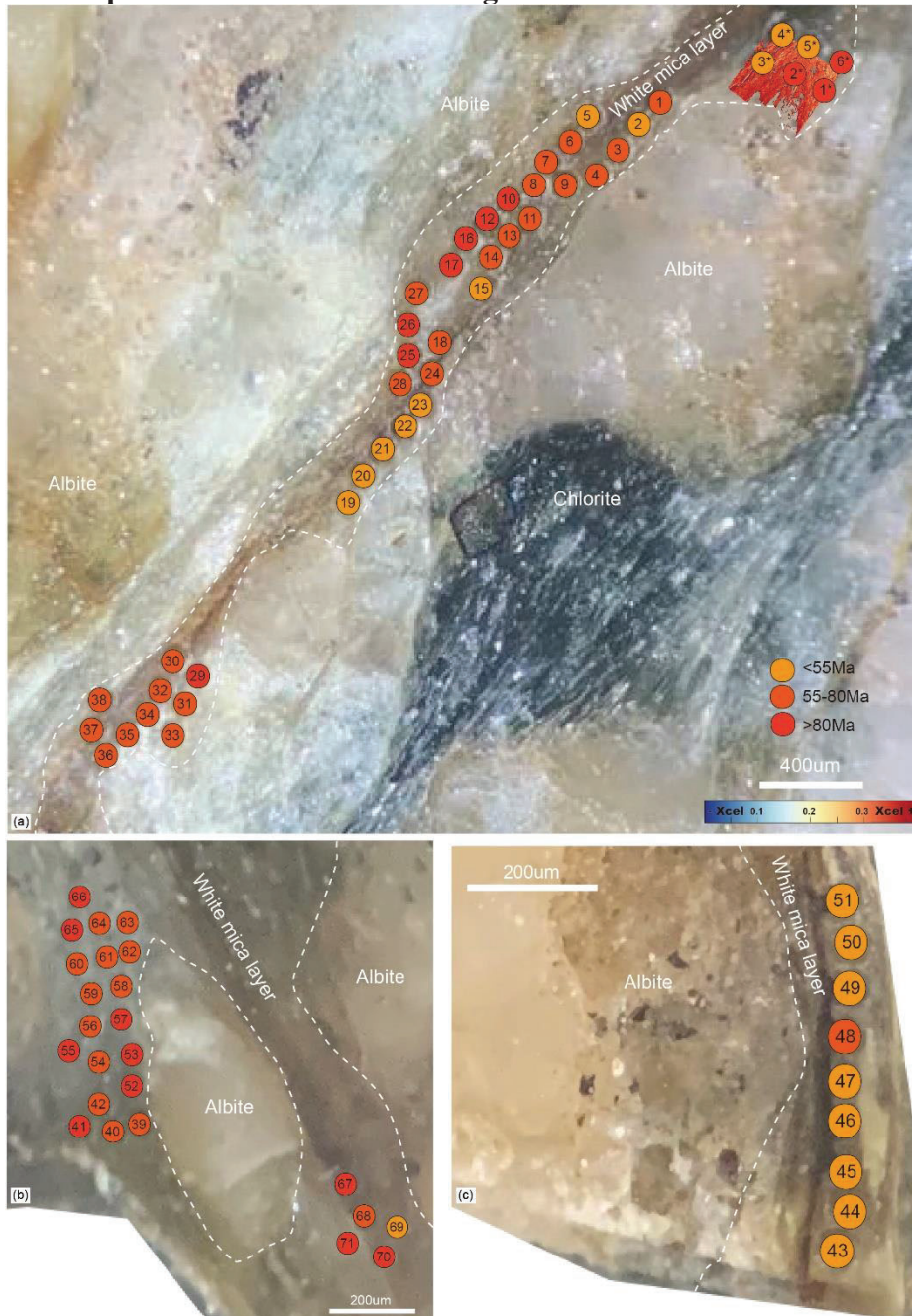


Fig.S6-1 a): In-situ laser points location map of N390 and N392 with colors corresponding to Xcel composition where available, circled numbers to spot numbers and circle colors to age range. b) and c): In-situ laser points location map.

Table S6-1 excel file for in-situ $^{40}\text{Ar}/^{39}\text{Ar}$ isotopic data

S7 Sample MW19-10B step heating dating

Include one run: N396, see Table S7-1 excel file for $^{40}\text{Ar}/^{39}\text{Ar}$ isotopic data

S8 Microprobe analytical procedure and X map tool

Sample petrographical observations were carried out in ISTO, University of Orléans, by using a Merlin Compact ZEISS scanning electron microscope (SEM) with an X-ray energy dispersive system (EDS) on a polished rock section, precise chemical composition data were acquired by electron microprobe analyses (EMPA). To convert the raw chemical composition datum obtained through EMPA or EDS into a visual compositional map require the use of XMapTools software, the detail of procedure can be found in Lanari et al. (2014).

S9 Microprobe results of MW19-38A and EMPA location

EMPA was carried out on area1 and area2, see Table S9-1 excel file for data

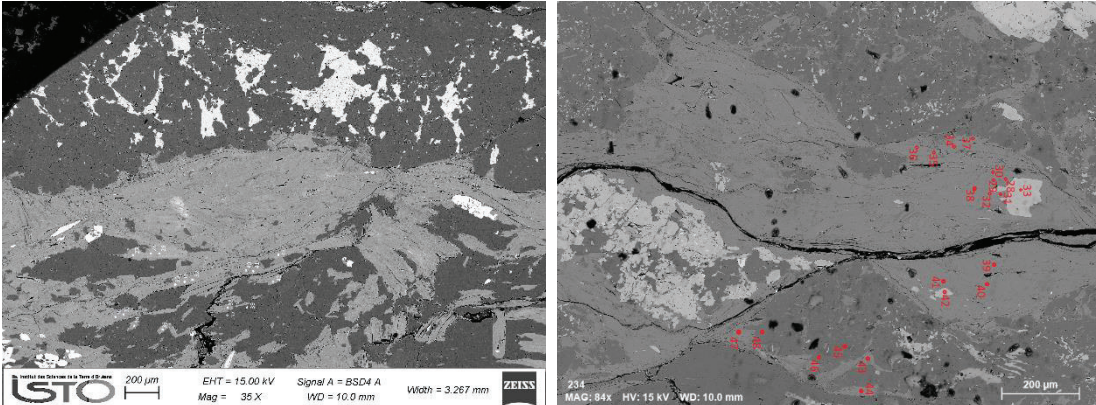


Fig.S9-1 EMPA location for MW19-38A, left: area1, right: area2

S10 Microprobe results of MW19-10B and EMPA location

EMPA was carried out on one area, see Table S10-1 excel file for data

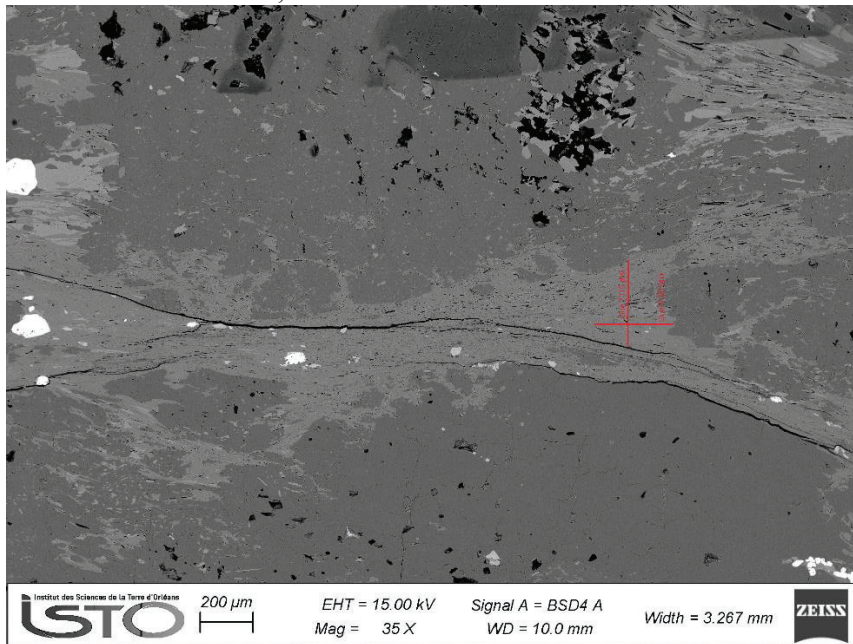


Fig. S10-1 EMPA location for MW19-10B

S11 Temperature estimate MW19-38A and MW19-10B

The detail of procedure can be found in Bourdelle et al. (2015).

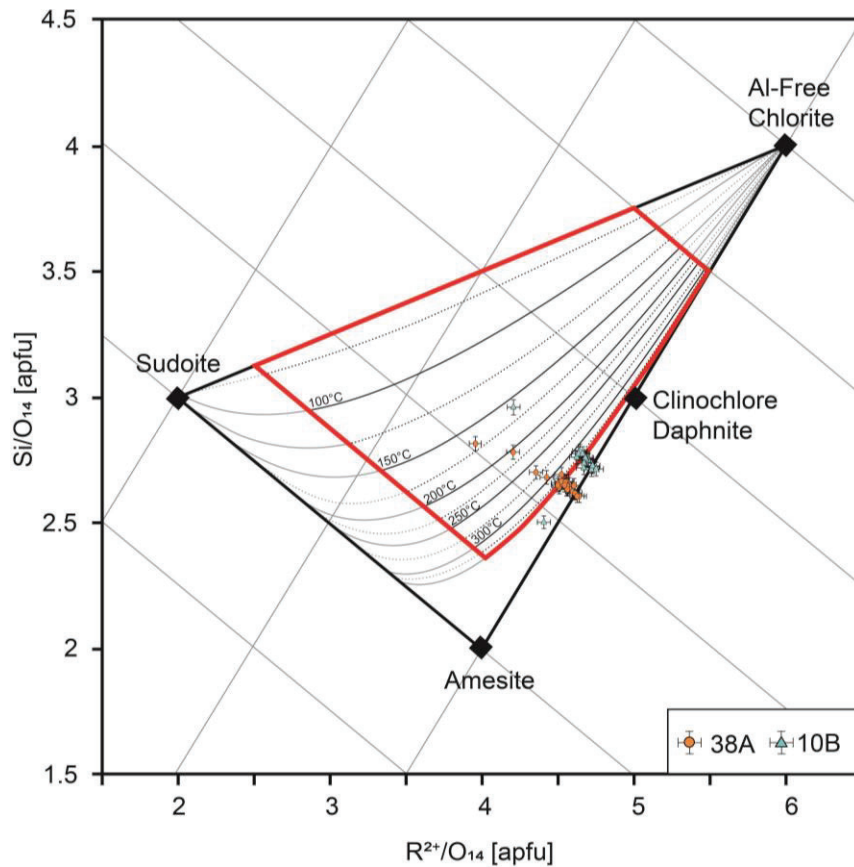


Fig. S11-1 T estimate MW19-38A and MW19-10B

Table S11-1 T estimate data of MW19-38A and MW19-10B

MW19-38A	Fe+Mg	±	Si	±	T	+	-
24 / 1 .	4.554	0.046	2.664	0.027	350°		
24 / 2 .	4.201	0.042	2.780	0.028	210°	10°	5°
24 / 3 .	4.592	0.046	2.627	0.026	350°		
24 / 4 .	4.505	0.045	2.641	0.026	350°		25°
24 / 5 .	4.593	0.046	2.622	0.026	>350°		
24 / 6 .	4.555	0.046	2.633	0.026	350°		
24 / 7 .	4.423	0.044	2.680	0.027	290°	25°	15°
24 / 8 .	4.603	0.046	2.648	0.026	>350°		
24 / 9 .	4.521	0.045	2.691	0.027	315°	35°	15°
24 / 10 .	4.570	0.046	2.652	0.027	350°		
24 / 11 .	4.608	0.046	2.616	0.026	>350°		
24 / 12 .	4.562	0.046	2.648	0.026	350°		
24 / 13 .	4.609	0.046	2.617	0.026	>350°		
24 / 14 .	4.560	0.046	2.646	0.026	350°		
24 / 15 .	4.522	0.045	2.657	0.027	350°		25°
24 / 16 .	4.499	0.045	2.657	0.027	330°	20°	10°
24 / 17 .	4.496	0.045	2.649	0.026	330°	20°	10°

24 / 18 .	4.520	0.045	2.665	0.027	340°	10°	20°
24 / 19 .	3.953	0.040	2.814	0.028	170°	5°	5°
24 / 20 .	4.352	0.044	2.700	0.027	265°	10°	5°
24 / 21 .	4.546	0.045	2.661	0.027	350°	25°	0°
24 / 22 .	4.541	0.045	2.649	0.026	350°	25°	0°
24 / 23 .	4.560	0.046	2.632	0.026	350°		
24 / 24 .	4.637	0.046	2.605	0.026	>350°		
24 / 25 .	4.622	0.046	2.605	0.026	>350°		
MW19-10B	Fe+Mg	±	Si	±	T	+	-
51 / 1 .	4.640695	0.046	2.784	0.028	315°	35°	15°
52 / 1 .	4.204965	0.042	2.958	0.030	160°	10°	10°
52 / 2 .	4.724074	0.047	2.722	0.027	>350°		
52 / 3 .	4.620044	0.046	2.760	0.028	320°	20°	30°
52 / 4 .	4.718588	0.047	2.710	0.027	>350°		
52 / 5 .	4.699048	0.047	2.748	0.027	350°		
52 / 6 .	4.685469	0.047	2.757	0.028	350°		25°
52 / 7 .	4.685008	0.047	2.753	0.028	350°		25°
52 / 8 .	4.67732	0.047	2.758	0.028	350°		25°
52 / 9 .	4.632987	0.046	2.774	0.028	320°	20°	30°
52 / 10 .	4.658478	0.047	2.773	0.028	325°	25°	25°
52 / 11 .	4.724984	0.047	2.725	0.027	>350°		
52 / 12 .	4.6659	0.047	2.718	0.027	350°		
52 / 13 .	4.747877	0.047	2.712	0.027	>350°		
52 / 14 .	4.667696	0.047	2.735	0.027	350°		
45 / 7 .	4.404405	0.044	2.502	0.025	>350°		